Università degli Studi di Palermo

AREA RICERCA E TRASFERIMENTO TECNOLOGICO

SETTORE DOTTORATI E CONTRATTI PER LA RICERCA

U. O. DOTTORATI DI RICERCA

Dottorato in Scienze Molecolari e Biomolecolari

Dipartimento di Scienze e Tecnologie Biologiche Chimiche e Farmaceutiche (STEBICEF)

Settore Scientifico Disciplinare CHEM-08/A

Advanced nanomedicines based on carbon nanodots for targeted theranostic approaches in breast cancer

LA DOTTORESSA

Roberta Cillari

IL COORDINATORE

Prof.ssa Giovanna Pitarresi

IL TUTOR

Prof.ssa Gennara Cavallaro

IL CO TUTOR

Prof. Nicolò Mauro

CICLO XXXVII

ANNO CONSEGUIMENTO TITOLO 2024

Table of contents

1 - Introduction

1.1. Breast cancer overview and management

Breast cancer (BC) is the most frequent malignancy and the second leading cause of death in women, counting about 2.3 million diagnoses and 670,000 deaths in 2022 (Bray Bsc et al., 2024). The high number of diagnoses is an impressive but somewhat encouraging finding, as the significant effort of screening and prevention campaigns has recently increased attention to BC, enabling many women to receive an early diagnosis which is critical for improving survival chances (Paci et al., 2014). Indeed, cancer contained in the breast or spreading only to the closest lymph nodes is considered curable by combining complete or breast-conservative surgical restriction with systemic adjuvant or neoadjuvant therapy. In contrast, the high mortality rate recorded for metastatic or advanced forms of BC is of concern, as well as the 5-year survival rate of metastatic BC, which stands at 29 % regardless of the tumor subtype and decreases to 12 % for metastatic triple-negative breast cancer (Burguin et al., 2021). In the case of advanced and non-operable tumors, the treatment protocol consists of systemic therapy, selected according to the specific molecular breast cancer subset of the patient.

The generic term breast cancer, actually, encompasses several tumor forms that can be gathered into five main subgroups based on their histological and molecular characteristics (Joshi & Press, 2018):

- luminal A-like, presenting a strong expression of hormone receptors (oestrogen receptor – ER and progesterone receptor – PR), but not expressing the human

epidermal growth factor receptor 2 (HER2); this breast cancer subtype presents a low histological grade of aggressiveness and is usually associated with good prognosis;

- luminal B-like HER2-, characterized by a lower expression of hormone receptors and higher aggressiveness compared to the luminal A-like subtype;
- luminal B-like HER2+, that encompasses luminal B-like tumors also presenting HER2 receptors expression;
- non-luminal HER2 enriched, which does not express hormone receptors while expressing high levels of HER2**;**
- basal-like triple-negative (TNBC), is the most aggressive form of breast cancer and the most difficult to treat as it does not express either hormone receptors or HER2, thus it is often associated with poor prognosis.

The better prognosis associated with hormone receptor-positive (HR+) and HER2+ subtypes of BC is not only due to the lower aggressiveness of these tumoral subsets, but also to the different treatment options available before recurring to intensive chemotherapy. The expression of hormone receptors (HR) provides specific therapeutic targets to address, making endocrine therapy the mainstay treatment, combined with chemotherapy only in case of therapeutic inefficacy and rapid progression (Lopez-Tarruella et al., 2022). Moreover, the implementation of CDK4/6 inhibitors in combination with endocrine therapy has been demonstrated to increase the progression-free survival of HER2- breast cancer, leading to the FDA approval of three CDK4/6i, palbociclib, abemaciclib, and ribociclib for this application (X. Wang et al., 2024). In HER2+ breast cancer the therapeutic strategy envisages the blockage

of the HER2 pathway using monoclonal antibodies, such as trastuzumab and pertuzumab, or chemotherapy, also in combination (Figueroa-Magalhães et al., 2014).

Instead, chemotherapy remains the main therapeutic option for treating TNBC, using anthracycline and taxanes as first-line options, followed by capecitabine and vinorelbine (Claessens et al., 2020). However, these chemotherapeutics are mostly hydrophobic small molecules with a poor pharmacokinetic profile that may result in short circulation time and reduced concentration at the site of action below therapeutic levels (Moorthi et al., 2011). On the other hand, high-dose treatment regimens are discouraged by the restricted therapeutic index and lack of selectivity of these cytotoxic drugs, which cause dose-limiting adverse effects that impair patients' prognosis and life quality (Corrie, 2011). To improve the efficacy and tolerability of chemotherapy treatments, combined or sequential administration of multiple therapeutic agents is recommended, although the occurrence of drug resistance phenomena represents a major limitation of this approach (Gote et al., 2021).

Multi-drug resistance (MDR) is a major cause of chemotherapy failure and it has been associated with over 90 % of cancer mortality (Bukowski et al., 2020). Cancer refractory to treatments may depend on the characteristics of the cancer subtype (intrinsic resistance) or being acquired during the treatment, increasing the chances of recurrence and metastasis (Luque-Bolivar et al., 2020). Several biological mechanisms concur in establishing MDR, including expression of membrane transporters causing increased drug efflux, facilitated drug metabolism, occurrence of genetic alterations that block apoptotic signaling, mutations of drug targets or activation of feedback

signaling responses, and reduced drug penetration and uptake in the tumor microenvironment (TME) (Yu et al., 2023).

Cancer cells are surrounded by a complex network of stromal cells and extracellular matrix (ECM) that dynamically interact, creating a unique TME that plays a cardinal role in cancer progression and drug resistance (Najafi et al., 2019). TME stroma embraces a heterogenous population of cancer-associated cells, including cancer-associated fibroblasts (CAFs), mesenchymal stem cells (MSCs), and innate and adaptative immune cells, which support tumor progression, promoting neo-angiogenesis, proliferative signaling, and immune escape (Hanahan & Coussens, 2012). Cancer-associated cellular stroma is embedded within a proteic matrix constituted of collagens, fibronectin, laminins, glycosaminoglycans, and proteoglycans, which provides structural sustainment while favoring biochemical signaling between cancer and stromal cells (Insua-Rodríguez & Oskarsson, 2016). The ECM architecture is responsible for the stiffness and elevated interstitial fluid pressure (IFP) of TME, forming a physical barrier that opposes drug permeation and correct vascularization, favoring the instauration of hypoxic and acidic conditions (Huang et al., 2021).

In the last decade, a better understanding of advanced breast cancer molecular characteristics and a deeper understanding of cancer TME led to the identification of new therapeutic targets and the development of emerging targeted therapy (J. Li et al., 2023), such, for example, poly(ADP-ribose) polymerase (PARP) inhibitors for patients with breast cancer (BRCA) genes mutations (Cortesi et al., 2021).

Evidence of the prognostic role of immune infiltration in HER2+ and TNBC has stimulated a growing interest in immunotherapy of BC, leading to the development of innovative therapeutic strategies to restore the host immune response against tumor cells (Pusztai et al., 2016). During its progression, BC escapes the physiological mechanisms of immune surveillance by promoting the expression of immunosuppressive mediators, including IL-10 and TGF-β, and expressing immune checkpoint regulators, such as cytotoxic T lymphocyte-associated protein 4 (CTLA-4), programmed cell death 1 ligand (PD-L1), indoleamine-2,3-dioxygenase (IDO), or lymphocyte activation gene LAG-3, which compromise tumor recognition and elimination by the immune system (W. Zou, 2005). The established immunosuppression in the TME is further aggravated by the polarization of tumor-associated macrophages (TAMs) to the M2 anti-inflammatory subtype and by the recruitment of T regulatory (Treg) cells and myeloid-derived stromal cells (MDSCs), which contribute to amplify the immunosuppressive signaling in the tumor microenvironment (TME), provoking the inhibition of $CD4^+$ T helper and $CD8^+$ cytotoxic T lymphocytes infiltration and activation against cancer cells (Dieci et al., 2021). The release of immunosuppressive mediators also affects innate immunity by altering the functions of natural killer (NK) cells and inhibiting antigen presentation mechanisms that should stimulate the action of the adaptive components of the immune system (Portale & Di Mitri, 2023). Several strategies have been proposed to intervene in BC immune evasion, leading to the over 400 clinical trials currently ongoing evaluating cancer vaccines and immune checkpoint inhibitors (Brown & Vomhof-DeKrey, 2024; Debien et al., 2023). However, the development of robust immunotherapies faces the complexity of immune suppression mechanisms in the

TME and the heterogeneity of BC, leading to high variability in patients' responses. Better clinical outcomes have been obtained by combining immunotherapy with conventional treatments, including chemotherapy and radiation therapy (Chun et al., 2019; Yap et al., 2021). Indeed, cytotoxic treatments may induce immunogenic cell death (ICD) by causing the release of damage-associated molecular patterns (DAMPs) at the tumor site, which promote a local inflammatory state that stimulates both innate and adaptative immune responses against cancer cells, thereby synergizing with immunotherapy (Krysko et al., 2012; Zang et al., 2022). The efforts in BC combination immunotherapy led to the approval of the PD-L1 inhibitor atezolizumab in association with nab-paclitaxel as a first-line option in the management of TNBC presenting a significative (> 1%) expression of PD-L1 (Mavratzas et al., 2020).

Hyperthermic treatment represents another promising approach for the clinical management of treatment-resistant BC. Unlike thermal ablation, which causes indiscriminate destruction of tissues by exposure to temperatures above 50 °C, hyperthermia involves a less drastic local temperature rise, reaching 42 °C (Mellal et al., 2017). Within this temperature range, significant alterations of cellular homeostasis occur, including protein denaturation and aggregation, inhibition of DNA repair mechanisms, modification of cellular membrane permeability, and alternation of cellular metabolism (Roti, 2008). However, the sensitivity to hyperthermia varies among different cell types, with cancer cells being more susceptible to cellular damage induced by local temperature increases than healthy cells, due to the limited heat dissipation and insufficient heat-shock response occurring in tumor tissues (Bettaieb et al., 2013). Besides inducing apoptosis by direct cytotoxic effect, hyperthermic treatments also sensitize cancer cells to chemotherapy and radiation therapy by

increasing blood perfusion and enhancing vascular permeability in the TME, thus reducing interstitial fluid pressure and re-establishing physiological pH and oxygen conditions (Dunne et al., 2020). Despite the promise of antitumoral hyperthermia, the clinical implementation of this therapeutic strategy is hampered by the limits of the heat-delivery methods, which usually encompass the generation of local, regional, or whole-body hyperthermia delivered by using an external source, such as microwaves, radiofrequency, ultrasound, and laser irradiation, applied superficially at patients' skin or using interstitial, intraluminal, or intracavital applicators and heat liquid perfusion (Chicheł et al., 2007). The main drawbacks of thermal treatment administration through the skin are due to the diffusion of the heat generated by the external source in the tissues, which leads to reduced and inhomogeneous heating at the cancer site, reaching insufficient therapeutic effect (Beik et al., 2016). On the other hand, the insertion or implantation of applicator devices allows heat to be generated near the tumor mass achieving local hyperthermia, but this method is highly invasive, may require anesthesia, and might cause pain and physical tissue damage at the application site, so it experiences low patient compliance (Jha et al., 2016). Moreover, in the metastatic setting, only the application of whole-body hyperthermia may offer some advantages in terms of chemotherapy sensitization, while potentially providing hemodynamic and cardiac complications (Lassche et al., 2019).

1.2. Nanomedicine in cancer treatment

The implementation of nanotechnology in biomedicine has revolutionized cancer therapy, offering new opportunities to overcome the limitations of conventional treatments. Nowadays, nanoparticles have been extensively employed as drug delivery

systems (DDS) to optimize the efficacy of classical chemotherapeutics and to reduce their severe off-target toxicity, thus minimizing the severe dose-limiting side effects of chemotherapy and improving patients' prognosis. To date, 15 cancer nanomedicines have been approved and are available on the market, of which at least 5 are indicated for breast cancer treatment (Table 1), and over 80 new nanomedicines are currently being evaluated in more than 200 clinical trials (He et al., 2019).

Product	Nanosystem	Indication
Doxil/Caelyx	PEGylated liposomal doxorubicin	Breast and ovarian cancer, myeloma
DaunoXome	Liposomal doxorubicin	Kaposi's sarcoma
Myocet	Liposomal doxorubicin	Breast cancer
Lipusu	Liposomal paclitaxel	Breast and non-small-cell lung cancer
Abraxane	Albumin-bound paclitaxel	Breast cancer, pancreatic adenocarcinoma, non-small-cell lung cancer
Oncaspar	L-asparaginase conjugate	Leukemia
DepoCyt	Liposomal cytarabine	Solid tumors or leukemia
Genexol-PM	Micellar paclitaxel	Breast cancers
Mepact	Liposomal mifamurtide	Osteogenic sarcoma
Marqibo	Liposomal vincristine sulfate	Leukemia
PICN	Nanosuspension of paclitaxel	Breast cancer
ONIVYDE	Liposomal irinotecan	Pancreatic adenocarcinoma
DHP107	Paclitaxel-loaded lipid nanoparticles	Gastric cancer
Vyxeos	Liposomal daunorubicin and cytarabine	Leukemia
Apealea	Micellar paclitaxel	Ovarian, peritoneal, and fallopian tube cancer

Table 1. Clinical-approved cancer nanomedicines.

1.2.1. Nanomedicine design and drug incorporation

Many of the nanostructures approved and under evaluation are liposomes , polymeric micelles, solid lipid nanoparticles, drug-polymer conjugates, and polymer nanoparticles, although the plethora of nanomaterials for clinical applications is much broader, encompassing polymer-, lipid-, inorganic- and carbon-based nanosystems with different design and characteristics (Mitchell et al., 2020) (Figure 1). Though highly diverse, these structures share common properties, such as high water solubility and nanometer size, which result in DDS with ideal pharmacokinetics improving the therapeutic outcome of chemotherapy (Aghebati-Maleki et al., 2020).

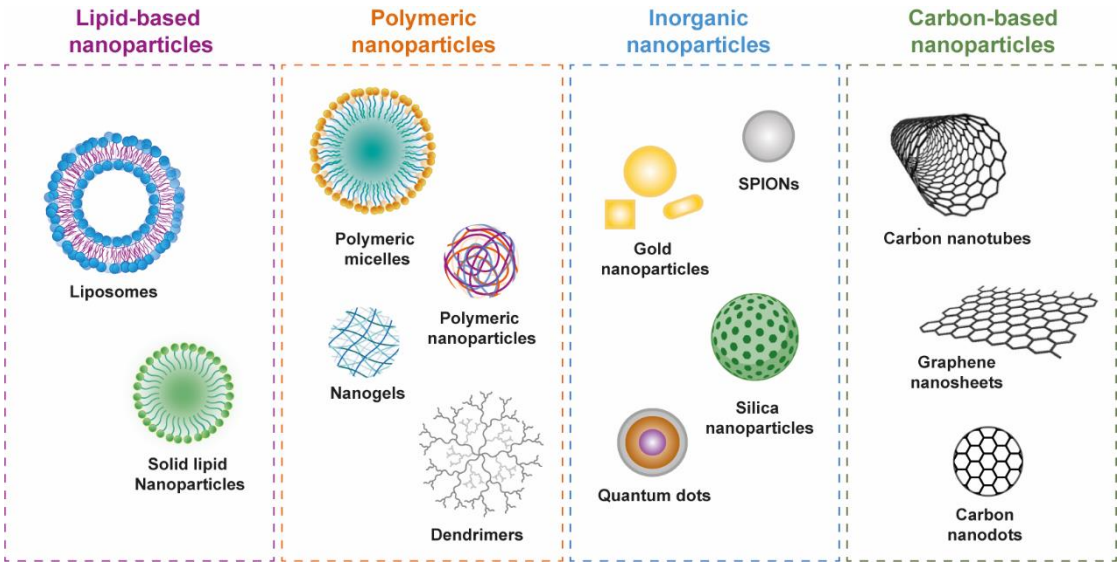

Figure 1. Architectures for nanomedicine applications. Examples of nanoparticles including lipid-based (liposomes and solid lipid nanoparticles), polymeric-based (polymeric micelles, polymeric nanoparticles, nanogels, and dendrimers), inorganic (super paramagnetic iron oxide nanoparticles – SPIONs, gold nanoparticles, silica nanoparticles, and quantum dots), and carbon- based nanoparticles (carbon nanotubes, graphene nanosheets, and carbon nanodots).

Depending on the nanocarrier structure, drugs are incorporated through physical interactions or chemical conjugation. Physical incorporation is achieved by surface absorption or encapsulation occurring during the nanosystem assembly. Structures like nanocapsules, polymeric micelles, and porous nanoparticles present hydrophobic compartments that can host lipophilic drugs, such as most chemotherapeutics (Hussein & Youssry, 2018; Mauro, Utzeri, Cillari, et al., 2022). An interesting approach to obtain nanoparticles forming inclusion complexes with drugs involves incorporating cyclodextrins (Cdx) in the nanostructure architecture (Dos et al., 2019). Cdx are cyclic oligosaccharides that spontaneously arrange in a tridimensional truncated cone shape, presenting a central hydrophobic cavity while maintaining a hydrophilic outer surface. This peculiar structure represents an ideal site for the molecular complexation of hydrophobic drugs, enhancing the drug loading of nanoparticles and favoring stable interaction with chemotherapeutics (Cutrone et al., 2017). The major challenge of physical encapsulation is the low drug-loading content, which commonly sets at 2 – 5% (Lu et al., 2016).

Alternatively, drug loading may be attached to the nanostructure through chemical bonds, which cleavage after administration induces the release of free drug enabling its interaction with the molecular target. However, the rapid dissociation of the drug payload, indicated as the “burst effect”, is often undesirable, leading to early elimination and inadequate dosage at the site of action (Bhattacharjee, 2021). Therefore the conjugation chemistry should be rationally designed to control drug release.

1.2.2. Benefits of administering chemotherapeutics as nanoformulations

The hydrophobicity and meager stability of chemotherapeutics represent a core challenge in their pharmaceutical formulation (Mattheolabakis et al., 2012). To enable the parenteral administration of several hydrophobic drugs, solvents and surfactants are usually required to favor their solubility, despite this approach may result in increased toxicity (Ten Tije et al., 2012). Incorporating chemotherapeutics into nanostructures with a biocompatible and hydrophilic surface is an effective strategy to increase their water solubility and improve their transport in the bloodstream.

Within the nanocarrier, drugs are also protected from degradation processes, that might alter their chemical structure thus compromising their pharmacological activity, and from early liver metabolism which might cause premature excretion. In addition, DDS can be designed to provide a slow and controlled release of the drug payload, keeping the drug concentration within a therapeutic window for a prolonged time and, thereby, allowing for reducing dosage and frequency of administration (Lee & Yeo, 2015). Overall, the increased stability of chemotherapeutics in nanoformulations has the potential to extend drug half-life and therefore improve their bioavailability (Banerjee & Sengupta, 2011; Kadam et al., 2012; Wicki et al., 2015).

However, to prolong the persistence of the DDS in the bloodstream, it is necessary to prevent their recognition and clearance by the reticuloendothelial system (RES), which occurs following the adherence of serum proteins (*i.e.* opsonins) on the nanoparticles' surface (Kaminskas & Boyd, 2011). This process depends on the nanostructure characteristics, with hydrophobic and charged particles easily undergoing opsonization (Fam et al., 2020). Therefore, a common strategy to avoid the absorption

of opsonins relies on hindering the electrostatic and hydrophobic interactions with serum proteins by grafting hydrophilic polymer chains at the surface of the nanostructure (Owens & Peppas, 2006). For this purpose, poly(ethylene glycol) (PEG) is the most effective and commonly used polymer due to its biocompatibility and hydrophilic nature. PEG coating on nanoparticles generates a hydration shell that sterically and thermodynamically hinders protein absorption (Suk et al., 2016). This strategy for escaping RES recognition is widely validated in the literature; in fact, several studies have demonstrated that nanoparticles coated with PEG having a molecular weight of 2kDa or higher showed increased circulation time *in vivo* (Miteva et al., 2015).

Particles' size also influences sequestration by the RES, which is physiologically predisposed to recognize structures having comparable diameters with pathogens such as viruses (~25 – 120 nm) and bacteria (200 – 250 nm) (Kaminskas & Boyd, 2011). Ultrasmall nanoparticles (< 8 nm) tend to escape absorption by RES, but their stay in the bloodstream is nevertheless limited because, due to their diameter below the glomerular filtration threshold (~ 5.5 nm), they are rapidly eliminated by renal filtration (Du et al., 2017). Besides, nanostructures rationally designed to have a hydrodynamic diameter of 10 – 15 nm have better chances of resisting rapid renal clearance, lingering in the bloodstream to be distributed to the target tissues (Goel et al., 2019).

1.2.3. Biodistribution of nanocarriers and passive accumulation in cancer

Chemotherapeutics can loosely diffuse through continuous vascular endothelium and cell membranes, resulting in indiscriminate distribution throughout the body and,

consequently, restricted therapeutic index due to severe side effects of cytotoxic drugs in healthy tissues (Patel & Patel, 2019). The incorporation of drugs within nanocarriers deeply changes their pharmacokinetics, as the biodistribution profile of DDSs is strongly influenced by their nanoscale dimensions. Differently from small molecules, nanosystems are retained in the vascular space and only permeate through fenestrations of discontinuous endothelium. Besides in liver and spleen, which present more permeable vasculature also in physiological conditions, this type of vascular architecture has been observed in inflamed tissues and in proximity to tumor formation s (Glassman & Muzykantov, 2019, Torchilin, 2011). The rapid growth of vessels during the process of tumor neoangiogenesis, in fact, results in the formation of a leaky and irregular vascular network, through which nanoparticles can easily extravasate. The higher permeability of cancer tissues is not compensated by increased lymphatic drainage, therefore nanoparticles are not efficiently removed from tumoral interstitial space, tending to accumulate (J. H. Park et al., 2008). This phenomenon, called the enhanced permeability and retention (EPR) effect, has been a milestone in antitumoral drug delivery, laying the groundwork for the development of cancer nanomedicine.

Although all currently approved and commercially available cancer nanomedicines rely on passive targeting of drugs based on the EPR effect (Fraguas-Sánchez et al., 2019), the real clinical relevance of this phenomenon is debated. Accumulating evidence, in fact, indicates that the EPR effect is strongly affected by heterogeneity among patients, cancer types, and tumor characteristics (Prabhakar et al., 2013; R. Sun et al., 2022). In particular, the complex composition and diversity of the TME strongly contribute to the variability of the EPR effect. The diffusion of nanoparticles from the perivascular region to cancer cells is impaired by the density of the ECM and the

elevated IFP encountered in the TME, which may differ substantially among different tumors causing drug resistance (R. Sun et al., 2022). IFP is also responsible for the accelerated removal of nanotherapeutics from the cancer site, as the high hydrostatic pressure of interstitial fluids of tumors may provoke an outward transport of therapeutic agents, further reducing the effect of nanomedicines (Ernsting et al., 2013; J. Guo et al., 2020). Nanosystems with ultrasmall size distribution (6-10 nm) are preferable to reach tumor parenchyma after extravasation owing to their higher diffusion throughout the stiff TME and in metastatic niches, compared to bigger nanoparticles (Mishra et al., 2018).

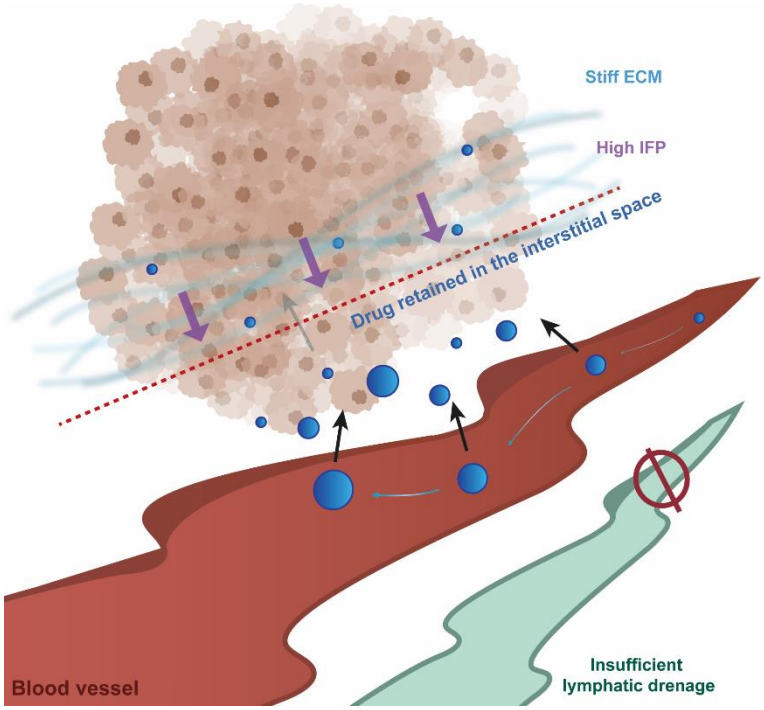

Figura 2. Passive targeting and limits of the EPR effect.

The peculiar and variable features of TME affecting the efficacy of the EPR effect are hard to recapitulate in pre-clinical tumor models, especially using animal models that drastically differ from human cancers in terms of growing rate, tumor-to-body weight

ratio, and metabolism. For instance, murine tumors grow sensibly faster than human cancers, developing a much more aberrant vasculature with loose pericyte coverage, and a less dense ECM, leading to overrated encouraging results of nanoparticles' efficacy (Danhier, 2016). The considerable limits of preclinical models on evaluating nanomedicine diffusion explain the different outcomes observed by promising EPR-based DDS when translating to clinics (Prabhakar et al., 2013).

1.2.4. Engineering the surface of DDS with targeting agents for active delivery

In addition to exploiting the physicochemical properties of DDSs to achieve their preferential targeting to the tumor site, active targeting of nanosystems can be achieved by introducing directional elements on their surface that can specifically bind receptors overexpressed by tumor cells. After extravasation, the specific binding with tumors should favor nanosystems' retention in the TME and improve selective uptake by cancer cells (Attia et al., 2019).

Besides hormones and HER-2 receptors, which are overexpressed in specific subsets of breast cancer, tumor cells present an aberrant expression of several receptors for growth factors and metabolites that are involved in cancer progression and are needed to sustain the high proliferation rate of cancer cells (Yoo et al., 2019). Among these, folate receptor (FR), epidermal growth factor receptor (EGFR), transferrin receptor (TfR), biotin receptor, and hyaluronic acid receptor (CD44) have been proposed as possible targets for nanomedicine delivery to breast cancer cells (Mauro, Scialabba, et al., 2020; Nandi et al., 2021; Rizwanullah et al., 2021; Roncato et al., 2018; Scialabba et al., 2019).

The metabolic reprogramming observed in tumor cells offers appealing opportunities for active delivery, capitalizing on the massive demand and uptake of nutrients needed to meet the energy requirements of rapidly growing tumors (Navarro et al., 2022). For instance, energy production in cancer cells prevalently relies on glycolysis and lactic acid production, rather than on oxidative phosphorylation, regardless of the oxygen concentration (Liberti & Locasale, 2016). This evidence, indicated as aerobic glycolysis or "Warburg effect", implies a greater glucose demand by cancer cells, resulting in higher glucose transporters expression and enhanced glucose uptake (Adekola et al., 2012). Therefore, the conjugation of nanoparticles with glucose derivatives has been proposed as a promising active targeting strategy to promote the selective uptake of nanomedicines by several cancers, leveraging the Warburg effect as a distinguishing property of tumor cells (X. Jiang et al., 2014; Morais et al., 2022).

Alternative drug delivery strategies target tumor stroma rather than cancer cells, including tumor vasculature and cancer-associated fibroblasts (J. Guo et al., 2020; X. Li et al., 2015). Moreover, the peculiar characteristics of TME can be exploited to achieve the targeted release of the drug payload after the preferential accumulation of the DDS in the tumoral tissue (Y. Jiang et al., 2022).

1.2.5. Stimuli-responsive nanocarriers for controlled drug release

To obtain extremely selective drug release at the tumor site, nanostructures can be rationally designed to undergo morphological or structural alterations as a response to the peculiar conditions of TME, resulting in the massive release of the antitumoral chemotherapeutic agent delivered only at the site of action (Mura et al., 2013). Distinguishing characteristics of tumor tissues that can be exploited as endogenous

stimuli to trigger release include acidic pH, high concentration of reducing species (GSH), hypoxia, and overexpression of specific enzymes (M. Liu et al., 2017). Although these are common features of cancer, the inter- and intra-tumoral variability of TME conditions pose a challenge to precise control of drug release thereby impairing clinical translation (Decuzzi & Cook, 2021).

Precise control of drug release is also obtained utilizing nanocarriers projected to be responsive to an external stimulus, such as electrical or magnetic field application, ultrasound treatment, local heat, and laser irradiation. Not depending on TME parameters, remotely activable DDS are less affected by cancer inhomogeneity providing less variable release compared to nanocarriers responsive to internal stimuli. Moreover, the possibility of directly directing the source of the exogenous stimulus to the target tissue guarantees the selective release of the drug payload where desired, providing high spatiotemporal control (Abouelmagd et al., 2014).

1.3. Beyond drug delivery: theranostic nanomaterials

The role of nanomedicine in cancer treatment is not limited to drug delivery applications: several nanomaterials have proven inherent and remotely triggered therapeutic properties, suitable to perform innovative anticancer treatments while avoiding the potential toxicity of chemotherapy or radiation therapy (Jia et al., 2020).

Interacting with biological environments, several nanomaterials may induce local generation of reactive oxygen species (ROS). Despite physiological ROS concentrations contribute to cell proliferation and differentiation, high levels of ROS disrupt the functional cellular redox balance, causing the activation of oxidative stress

pathways. Although undesirable in healthy tissues, oxidative stress selectively induced in cancer cells can be harnessed to induce ROS-mediated cytotoxicity, obtaining direct cellular damage that may lead to the activation of apoptosis and autophagy cell death mechanisms (L. Li et al., 2015; T. Zhang et al., 2020).

Nanomaterials capable of converting the applied electromagnetic radiation to heat have been intensively studied as potential therapeutic agents to perform selective photothermal treatments (PTT), overcoming the drawbacks of conventional hyperthermia. Photothermal agents, indeed, enable targeted and minimally invasive hyperthermic treatments that rely on the on-demand controlled activation of the nanosystem, by irradiation with an external light source. Focusing the irradiation on the cancer tissue, where the nanoheater is accumulated by passive or active targeting, provides a localized temperature increase at the tumor site, preserving healthy tissues from possible heat damage. For the photoactivation of the nanosystem, near-infrared (NIR) irradiation is recommended due to its superior penetration depth through organic tissues compared to ultraviolet (UV) and visible electromagnetic radiations, favoring PPT of cancer in deep sites (Lv et al., 2021).

Nanomaterials with promising antitumoral potential can be further engineered to present contrast properties valuable for bioimaging and biosensing, obtaining advanced nanostructures endowed with both diagnostic and therapeutic properties. Such multifunctional nanoparticles, usually indicated as *theranostics*, have aroused increasing interest in nanomedicine because of their incredible potential for extremely targeted anti-cancer treatments (Kelkar & Reineke, 2011). Early approaches to theranostics simply involved the use of nanocarriers such as liposomes, micelles, and

polymer nanoparticles for co-delivery of an anticancer chemotherapeutic drug and a contrast agent for magnetic resonance imaging (MRI), positron emission tomography (PET), or computed tomography (CT) (E. K. Lim et al., 2015). This strategy has been nowadays outdated by the development of nanomaterials with inherent contrast properties, which do not require conjugation with other probes or dye loading to be detectable by common diagnostic techniques (Key & Leary, 2014; W. Li & Chen, 2015; Xie et al., 2010).

Noble metal nanoparticles have been extensively studied as potential PTT agents because of their strong absorbance in the NIR region and suitable photothermal conversion ability. Gold nanoparticles (AuNPs), and in particular gold nanorods, display fascinating tailorable optical properties, adjustable by varying their size and shape, that can be optimized to obtain remarkable NIR absorption. Based on their conformation, AuNPs show localized *surface plasmonic resonance* that results in enhanced absorption of the exciting light, which energy is subsequently dissipated as heat production and, also, re-emitted as electromagnetic radiation. The re-emitted light confers intrinsic photoluminescence to the nanomaterial, which is suitable for tracking the nanosystem by fluorescence imaging (FLI). Besides, AuNPs have also been proposed as contrast agents for X-ray-mediated computed tomography (CT) and photoacoustic imaging, demonstrating high versatility for bioimaging applications. Despite the excellent performance of AuNPs as PTT agents and bioimaging probes, critical concerns about their long-term cytotoxic effects arose impacting their clinical translatability. These nanoparticles, in fact, are not biodegradable and tend to accumulate in high-perfused organs, such as liver, intestine, kidney, and spleen, provoking long term toxicity due to oxidative damage (Sani et al., 2021).

Super-paramagnetic iron oxide nanoparticles (SPIONS) are also interesting nanostructures for bioimaging purposes due to their paramagnetic properties which alter the longitudinal (T_1) and transverse (T_2) relaxation rates of fluids in the surrounding volume. This feature confers magnetic contrast to these nanoparticles, which is suitable for magnetic resonance imaging (MRI) applications (Shabestari Khiabani et al., 2017). MRI is a powerful non-invasive technique useful to image and monitor the progression of cancer, providing deep penetration imaging with high soft-tissue contrast. The potential of SPIONs in MRI led to their approval as possible substitutes for gadolinium(III)-based contrast agents, which, however, are still the clinical standard due to their superior performance, despite the high toxicity risk associated with Gd^{+3} ions (Caspani et al., 2020; Pasquini et al., 2018). Besides their imaging potential, SPIONs are also capable of transforming electromagnetic energy into heat, which is suitable for performing magnetic-hyperthermic treatments (L. Wu et al., 2016).

The bioimaging contrast of nanoparticles used as PTT agents can be exploited to guide the therapeutic intervention, performing the remote activation of the nanosystem when its maximum accumulation at the site of action is observed. Imaging-guided photothermal therapy (IG-PTT) provides further improved spatiotemporal control of the hyperthermic treatment that results specifically targeted to the cancerous site. Furthermore, the visualization of nanoparticles in different tissues from the primary tumor by bioimaging opens to performing PTT directed to secondary tumoral formations or metastatic sites, thus providing innovative treatment possibilities for advanced disease (L. Zou et al., 2016).

Besides AuNPs and SPIONs, carbon-based materials have attracted increasing attention as theranostic nanomaterials, providing substantial advantages over noble metal-based nanoheaters, including low-cost, higher stability, and biodegradability. Among the several carbon allotropes proposed, including carbon nanotubes, graphene oxide, and fullerenes, carbon nanodots have recently emerged as promising nanomaterials for theranostic applications.

1.3.1. Carbon nanodots

Carbon nanodots (CDs) are versatile organic nanoparticles, usually smaller than 10 nm, typically composed of carbon, oxygen, nitrogen, and hydrogen (Mauro et al., 2021). The carbonaceous core of CDs may present an amorphous or crystalline structure, which can be organized in crystallin layers assuming graphitic-like features.

Since their fortuitous discovery in the early 2000s (Funkhouser, 2002), they have attracted increasing interest due to their fascinating optical properties associated with advantageous physical and chemical features. Despite their simple chemical composition, CDs present multicolor fluorescence emission, characterized by high sensitivity to the environment and tunable by modulating the excitation wavelength (Goryacheva et al., 2017; Sciortino, Cannizzo, et al., 2018), as well as a strong photo-thermal conversion ability (Balou et al., 2022; Mauro, Utzeri, Sciortino, et al., 2022). These main hallmarks are accompanied by many additional benefits, such as high surface-volume ratio, high water solubility, and high biocompatibility (Scialabba et al., 2019). The unique combination of properties provided by CDs can be exploited, for example, in electronic device manufacturing, photocatalysis, and optical sensing, as well as for several medical purposes including the production of fluorescent

biomaterials for application in additive manufacturing and regenerative medicine, bioimaging, biosensing, photothermal therapy, and drug delivery (Feng et al., 2020; Hola et al., 2014; Kaurav et al., 2023; Mauro et al., 2024; Nazri et al., 2021).

CDs can be easily synthesized by the disruption of pre-formed carbon structures (top-down methods) or by carbonization of small organic molecules (bottom-up methods) (Figure 3). Bottom-up methods are advantageous over top-down approaches as the properties of the resulting CDs can be tailored by an appropriate selection of the reaction conditions and of the molecular precursors, which are usually obtained from low-cost organic materials or biomass, and can be thoroughly selected to confer peculiar characteristics to the final structure of CDs (Mauro, Utzeri, et al., 2020).

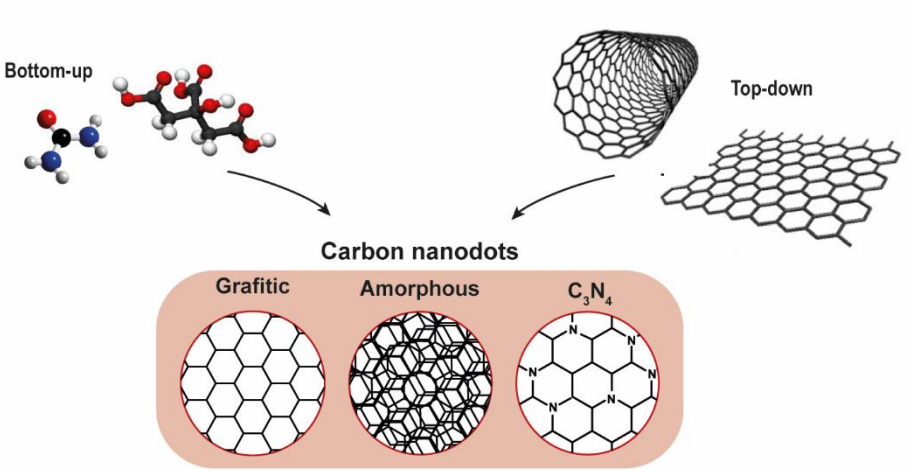

Figure 3. Synthesis and structure of CDs

For instance, the incorporation of heteroatoms, such as nitrogen and sulfur, within the core of CDs has been proven to enhance the photoluminescence of CDs and it is easily achieved by introducing N- and S- bearing small molecules among the molecular precursors (Y. Park et al., 2016). Synthesis performed in the presence of high nitrogen

concentrations leads to carbon nitride (C_3N_4) nanostructures, organized in either graphitic or crystalline cores (Messina et al., 2016; Sciortino, Mauro, et al., 2018). Within the core of CDs, heteroatoms alter local charge density and structural defects disposition, causing a profound change in the electronic states of CDs that are strongly correlated with the optical properties of these nanoparticles (Yan et al., 2019). Although the origin of CDs' fluorescence is still unclear, experimental observations highlighted that a bright photoluminescence is obtained by introducing irregularities, such as sp^3 carbons, hydroxyls, or carbonyl groups, in a π-conjugated electron system. This evidence suggests the dependency of CDs' fluorescence emission on the structure of the carbonaceous core, involving mechanisms of recombination of electron-hole pairs in π and π^* electronic levels of the sp^2 sites, and on its interaction with the surface electronic states, (Goryacheva et al., 2017). Surface electron states are also involved in the mechanism of CDs' fluorescence, as indicated by the strong dependence of this phenomenon on surface passivation and environmental conditions (Mao et al., 2010). In particular, the multicolor fluorescence of this nanomaterial is associated with the presence of surface electronic traps at different energies, which are stabilized through surface functionalization (Lecroy et al., 2017; S. Y. Lim et al., 2015). Commonly, the surface of CDs is functionalized with biocompatible polymers, such as poly(ethylene glycol) (PEG), obtaining a red-shift of the emission peak and an increase of the fluorescence intensity, evaluated in terms of quantum yield (Y. P. Sun et al., 2006). Besides its impact on optical properties, the conjugation with polymers is also functional to improve the pharmacokinetics of CDs. The ultrasmall size of CDs (< 5 nm) guarantees their bioelimination after administration, avoiding any accumulation and retention by the RES, but it may be responsible for early renal clearance.

Biopolymers conjugated at the surface of CDs determine an increase in the average hydrodynamic diameter above the renal cutoff, prolonging the circulation time of the nanosystem (Scialabba et al., 2019; Suk et al., 2015). The functionalization of CDs is easily achieved by bioconjugation, leveraging the surface chemistry of these nanoparticles. Indeed, CDs are usually rich in polar functional groups, such as carboxyls, amines, and hydroxyls, which confer to the nanostructure high dispersibility in different solvents and facile processability (W. Liu et al., 2016).

Due to their unique optical properties, CDs are valuable for FLI, showing superior performance compared to both fluorescent organic dyes and nanoparticles having similar emission properties, such as semiconductor quantum dots, in terms of chemical and photo-stability (Phan & Cho, 2022). In cancer diagnosis, CDs used to label tumor cells allow their detection by flow cytometry and their investigation at a molecular level by fluorescence microscopy. At the same time, their FLI potential confers to CDs self-tracking ability, useful for *in vitro* or *ex vivo evaluation* of their distribution and intracellular trafficking (R. S. Wu et al., 2022).

The sensitivity of CDs' optical properties to external conditions is valuable for sensing the surrounding environment, obtaining information on pH, ions concentration, and solvents. In cancer therapy, biosensing devices are useful to monitor changes in TME parameters in response to treatment. For instance, the pH of tumor tissues (6.4) is acid compared to the physiological value of blood circulation (7.4), and further decreases at intracellular levels in cancer (5.5). During tumor regression, a relief of acidic conditions in TME is observed as a consequence of restored oxygen levels and physiological metabolism in the healing tissue. Thereby, pH changes in the TME are

directly correlated to the treatments' efficacy (Espina-Casado et al., 2021; L. Wang & Li, 2011). Enabling real-time evaluation of therapeutic results, biosensing opens the way to sophisticated and personalized antitumoral approaches, tailorable on the basis of the individual response.

Besides their photoluminescence, CDs can re-emit part of the absorbed light through non-radiative processes, causing local heat production (Balou et al., 2022). Associating bioimaging properties with photothermal conversion ability, CDs are envisioned as suitable agents to perform NIR-triggered IG-PTT. The application of FLI for *in vivo* monitoring and therapeutic guidance is, however, challenging, due to the light absorption and scattering phenomena occurring in biological tissues that limit the penetration depth of light radiation and affect the spatial resolution of the output imaging signal (Rao et al., 2007). The reduced biological tissues interference with light in the red and NIR region opens a transparency window that can be exploited for FLI-guided PTT (Weissleder, 2001).

The therapeutic potential of CDs also extends to drug delivery applications. Due to their structure containing sp^2 and sp^3 hybridized carbons, CDs can load hydrophobic drugs via strong π–π interactions. Moreover, the high surface area to volume ratio ensures high drug-loading capacity to CDs, whereas their ultrasmall size enables drug delivery at intracellular levels (Bartkowski et al., 2024; Jung et al., 2016).

Showcasing bioimaging, biosensing, and therapeutic potential in a single ultrasmall nanoparticle, CDs represent a promising nanomaterial with outstanding potential for cancer theranostic applications (Figure 4).

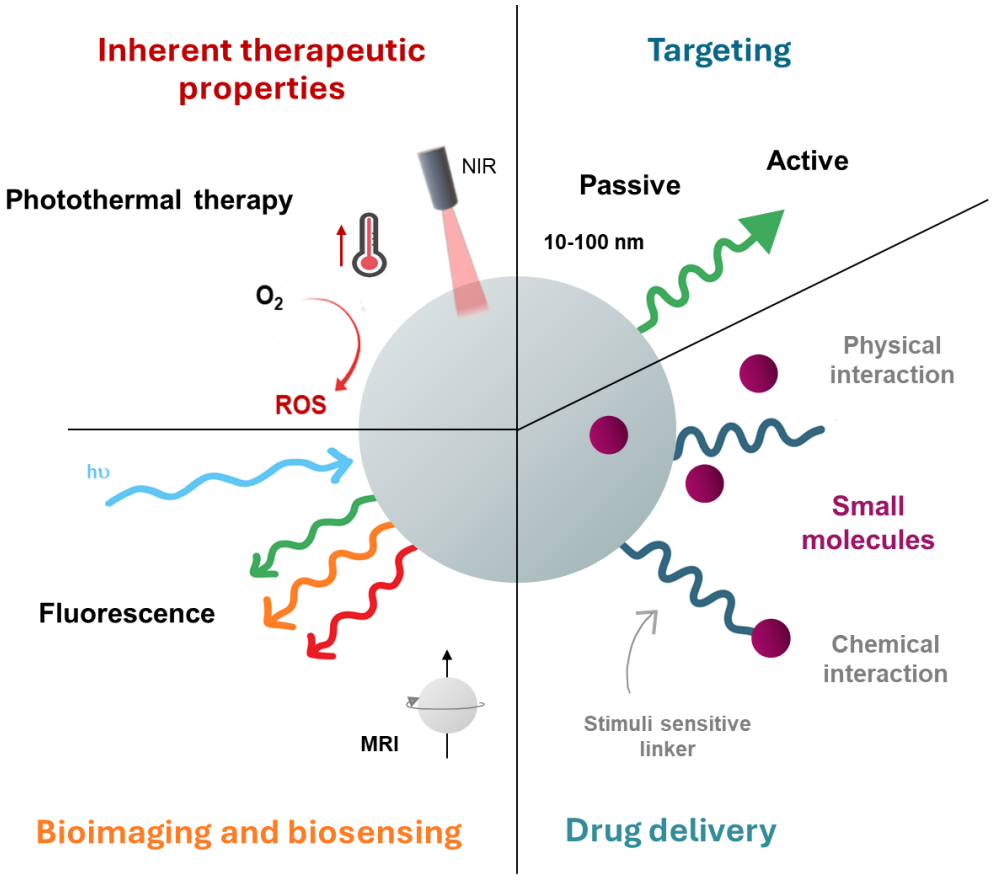

Figure 4. Properties of CDs and applications in cancer theranostics.

The rate-limiting drawback of CDs for their clinical translatability is the extremely low average reaction yield obtained for their synthesis. Attempts to increase the reaction yields above 10% resulted in broader size distributions and severe structural heterogeneity. Therefore, there is an urgent need for optimized synthetic protocols to prepare homogenous CDs with high reaction yields (H. Liu et al., 2024).

In 2022, our research group published an efficient protocol to obtain decagram-scale quantities of N,S-doped CDs with a narrow size distribution and interesting optical properties (Mauro, Utzeri, Sciortino, et al., 2022). In detail, CDs were synthesized by solvothermal decomposition of citric acid and urea in dimethylformamide (DMF), in

the presence of green indocyanine, used as a sulfur donor. The adopted synthetic route yielded CDs of about 5 nm with bright multicolor fluorescence following light absorption in the UV-visible range and remarkable photo-thermal efficiency in the NIR region, which has been exploited to induce hyperthermia causing cancer cell death *in vitro*. CDs also displayed oxidant activity, presumably due to S-doping, causing an increase in ROS levels in cancer cells, which has been further enhanced with local NIR irradiation. Overall, the inherent anticancer properties of the obtained CDs resulted in noteworthy selective susceptibility of cancerous and pre-cancerous cells to CDs treatment, which deservers further investigations.

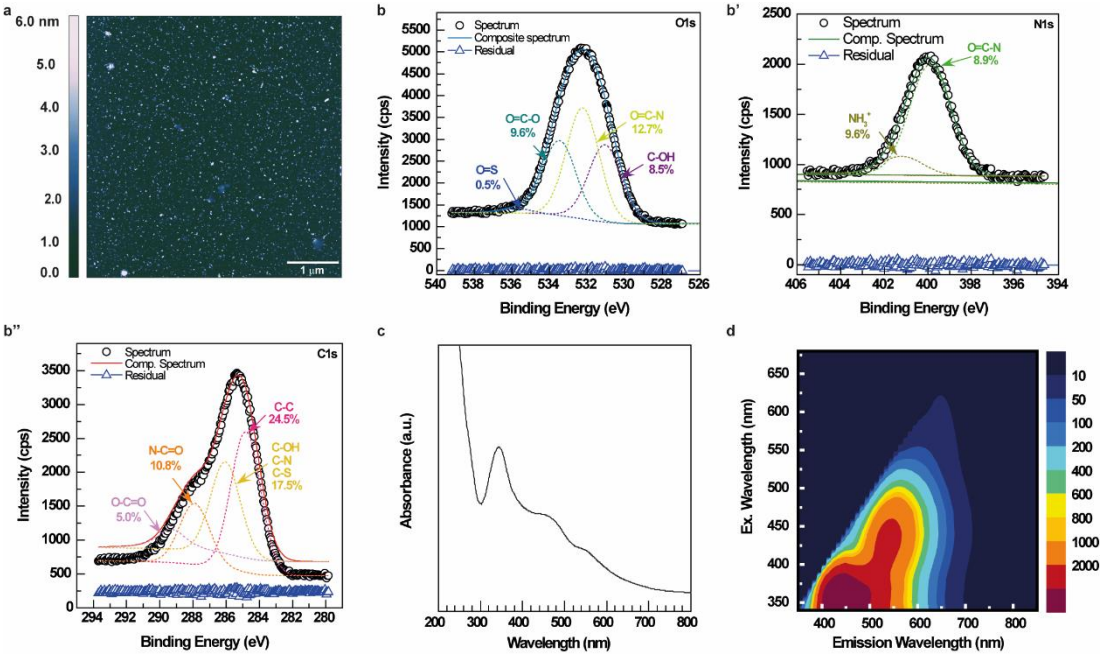

Figure 5. Panel resuming the properties of N,S-doped CDs, readapted from (Mauro, Utzeri, Sciortino, et al., 2022), including AFM micrograph (a), surface chemistry analyzed by XPS analysis (b-b''), UV-visible absorption spectrum (c), and 3D fluorescence emission (d).

2. Aim of the work

The poor prognosis and limited survival of patients with non-operable advanced or metastatic breast cancer are related to the unspecificity and dose-limiting toxicity of conventional treatments, which are often inefficient in addressing breast cancer heterogeneity and treatment resistance. Nanomedicine has emerged as a promising antitumoral approach to implement personalized, non-invasive, and efficient treatments, overcoming the drawbacks of conventional therapies. In particular, theranostic nanomaterials offer unique opportunities to implement extremely targeted anticancer treatments by integrating multiple therapeutic approaches with bioimaging and biosensing abilities.

The present thesis work is focused on the development of theranostic nanoplatforms with different designs, projected to explore several multimodal approaches in breast cancer diagnosis and treatment. The common thread of the envisioned theranostic nanosystems is the presence of carbon nanodots as the central element. CDs were selected to confer unique optical properties to the nanostructures, which can be tailored by accurately selecting molecular precursors and synthetic parameters, as well as rationally designing the post-synthetic surface passivation. The surface chemistry of these nanostructures favors their manipulation and processing, enabling easy functionalization through simple, cost-effective, and eco-friendly coupling reactions. The choice of CDs over other nanomaterials with similar optical properties lies in the tunability of their optical properties, together with their superior biocompatibility, which confers them unique versatility and safety for biomedical applications. Moreover, CDs demonstrated intrinsic anticancer properties causing selective breast

cancer damage, going beyond the paradigm of nanoparticles as drug delivery systems. In particular, CDs are useful as photothermal agents to perform NIR-triggered hyperthermic treatment and have been associated with local ROS generation, provoking oxidative stress damage to cancer cells.

To enhance the inherent therapeutic potential of CDs, the first part of the present work proposes two strategies to leverage the antitumoral effect of ROS signaling activation by combination therapy. The first explored approach involves the strategic use of CDs as delivery systems for drugs targeting ROS pathways, such as the PDE-5 inhibitor sildenafil (Rotella, 2002). The simultaneous stimulation of ROS production by sildenafil and CDs should amplify the oxidative stress-mediated cancer cytotoxicity, resulting in a tumor-specific synergistic effect. The loading of sildenafil on CDs has been favored by engineering the nanoparticles by conjugation with β-cyclodextrins, which form an inclusion complex with the drug, enhancing its solubility and improving its stability (Al Omari et al., 2006). Furthermore, the interaction of sildenafil with β-cyclodextrins should modulate the drug release kinetics, favoring the payload release at the site of action. The conjugation protocol was studied to obtain well-organized nanostructures in which the central carbon nanodots were decorated with several cyclodextrin moieties at the surface. The impact of CDs- β-cyclodextrins conjugates loaded with sildenafil on PDE-5 expressing cells, including ER^+ breast cancer cell line MCF-7, were evaluated *in vitro*, assessing cell viability, oxidative stress levels, and expression of genes involved in ROS homeostasis.

Cancer cell death induced by the local overproduction of ROS has been associated in the literature with enhanced antitumor immune response, suggesting a potential

synergy of oxidative stress mediators with cancer immunotherapy (S. Guo et al., 2021). On this basis, the combination of CDs-mediated anticancer activity with immune-stimulation was evaluated as a promising strategy to achieve a dual-mode breast cancer immunotherapy. To this aim, CDs were conjugated with indoximod, an immune adjuvant acting on the downstream pathway of indoleamine-2,3-dioxygenase (IDO), which plays an important role in TME immunosuppression (Brincks et al., 2020). Although indoximod used as monotherapy demonstrated only modest immunomodulatory efficacy, the noteworthy results obtained from indoximod together with chemotherapy and radiation therapy highlight its improved performance in combination treatment regimes, validating its potential synergic activity with CDs-mediated antitumoral effect (Jackson et al., 2013; Soliman et al., 2014, 2016). The anticancer properties of CDs-indoximod conjugates (CDs-IND) were evaluated both *in vitro* and *in vivo* breast cancer models, and an extensive characterization of TME was performed to establish the impact of CDs-IND treatment on TME immune profile.

The second part of this thesis work focused on developing multimodal imaging carbon-based nanostructures, designed to improve the potential *in vivo* performance of CDs for bioimaging and biosensing purposes. In particular, the strategies explored involve the incorporation of contrast agents within the carbonaceous core of CDs during their solvothermal synthesis, obtaining hybrid nanostructures endowed with bi-modal imaging properties. The obtained nanostructures should maintain the CDs' photoluminescence that allows FLI for *in vivo* and *ex vivo* evaluations with high sensitivity and spatiotemporal resolution, with additional benefits provided by the doping agent which should confer to the nanoplatform deep-tissue imaging with high contrast, for instance by CT or MRI.

The first attempt here reported in this sense concerns the incorporation of gold seeds within the structure of CDs, to obtain gold/carbon nanohybrids (AuCDs) endowed with CT/FLI bi-modal imaging, obtained by combining the optical properties of CDs with the X-ray attenuation properties of gold. The surface of AuCDs was functionalized with 2-deoxy-(D)-glucose, chosen as a targeting agent to specifically direct AuCDs towards cancer cells by exploiting the Warburg effect. Different biological models have been used to evaluate the bioimaging performance of AuCDs-Glu, as well as their efficacy of the selective targeting strategy to achieve preferential uptake by cancer cells, in order to assess the potential of AuCDs-Glu for theranostic applications.

In parallel, another promising hybrid nanostructure was developed by doping the core of CDs with gadolinium (III) ions, thus to obtain MRI/FLI bi-modal imaging theranostic nanotools. Indeed, gadolinium(III) organic complexes are the most widely used MRI contrast agents in clinics, despite the potential toxicity related to the release of free Gd^{+3} ions (Pasquini et al., 2018). The incorporation of Gd^{+3} should confer MRI contrast to the nanostructure while preventing the unspecific release of toxic ions, providing a huge advantage over commercially available gadolinium chelates and other nanoparticles complexing Gd^{+3} at the surface. Besides presenting paramagnetic properties, GdCDs should retain the optical properties of CDs enabling IG-PTT of breast cancer. Moreover, the effect of pH on the imaging properties of GdCDs was evaluated to assess the applicability of GdCDs in TME biosensing, resulting in multifunctional nanosystems with huge potential in precision cancer therapy and monitoring.

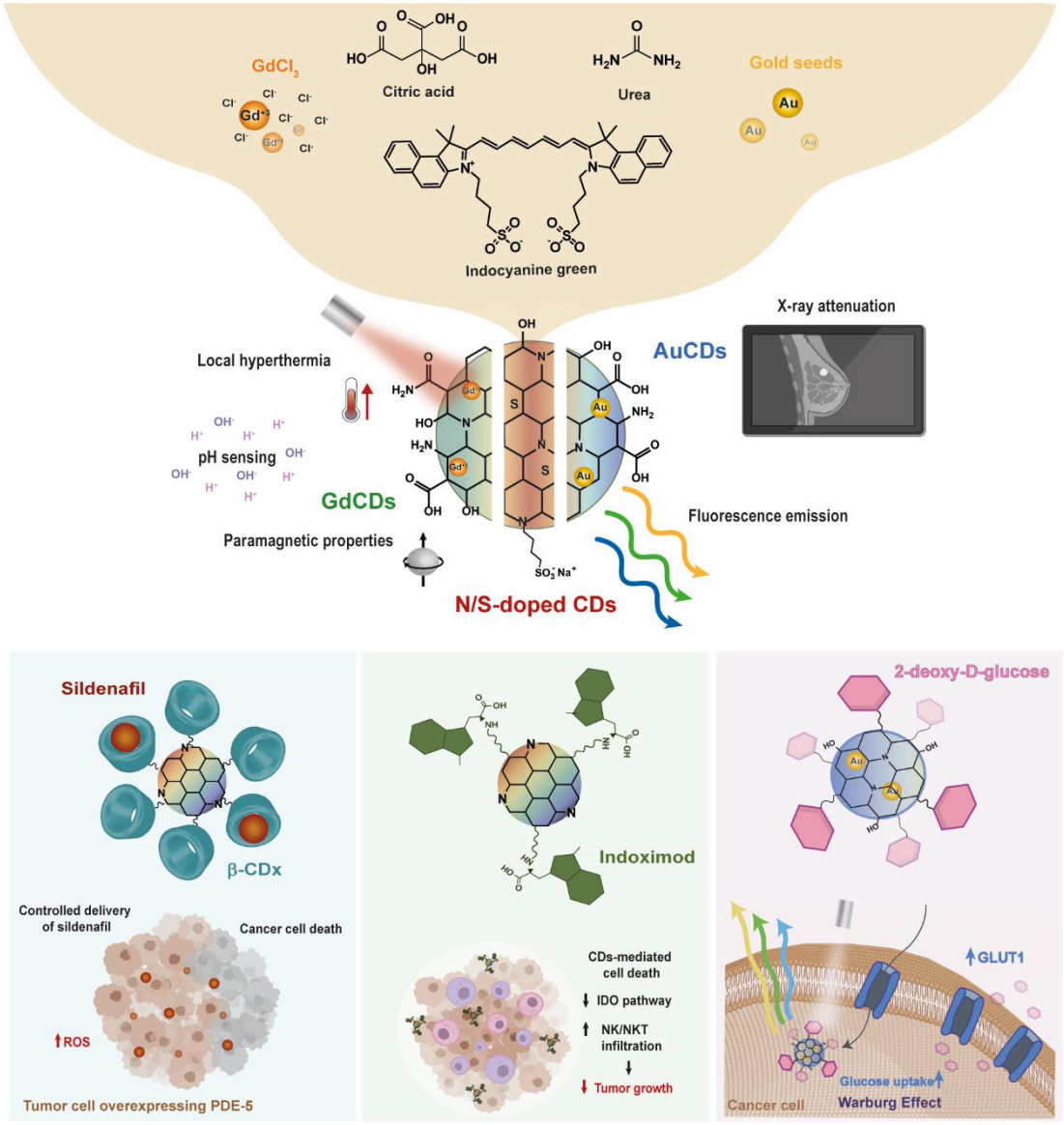

Figure 6. Graphical abstract of the proposed nanostructures and their potential application in breast cancer theranostics.

3 – Results and discussion

3.1. β-cyclodextrins conjugated carbon nanodots delivering sildenafil to perform targeted anticancer treatments based on ROS signaling activation

3.1.1. The conjugation of carbon nanodots with β-cyclodextrins leads to ultrasmall photoluminescent nanostructures

N/S co-doped carbon nanodots (CDs) (5.1 ± 0.3 nm), obtained as described by Mauro et al. (2022), were conjugated with β-cyclodextrins (β-Cdx) through a convergent synthesis protocol consisting of a preliminary functionalization of CDs and β-Cdx treated separately to form derivatives bearing alkyne- and azido- groups, respectively, which reacted in a subsequent step through a click chemistry reaction to form the final structure.

Firstly, a regioselective mono-functionalization of β-cyclodextrins was achieved by selectively activating the hydroxyl group in position 6 of one monomer by mono-tosilation, using *p*-toluenesulfonyl chloride in strongly basic conditions. This synthetic protocol, extensively reported in the literature, is usually followed by purification processes such as precipitation or crystallization in organic solvents, which lead to low yields of the pure product (Djedaini-Pilard et al., 1999; Kasal & Jindřich, 2021). Instead, we adopted an alternative purification technique, already reported by Tripodo et al. (2013) that exploits a cation exchange resin to cause a rapid reduction of the solution pH to acidic conditions, inducing a critical decrease of mono-tosylated-β-

cyclodextrins (Cdx-OTs) solubility and therefore provoking their selective precipitation, whereas unreacted β-Cdx and *p*-toluenesulfonic acid were maintained in solution and removed by washing with ultrapure water. Subsequently, the tosyl – leaving group easily underwent a nucleophilic substitution by azoture under mild and green conditions, giving mono-6-azido-6-deoxy-β-cyclodextrins (β-Cdx-N_3) with a 40 % yield (Figure 7).

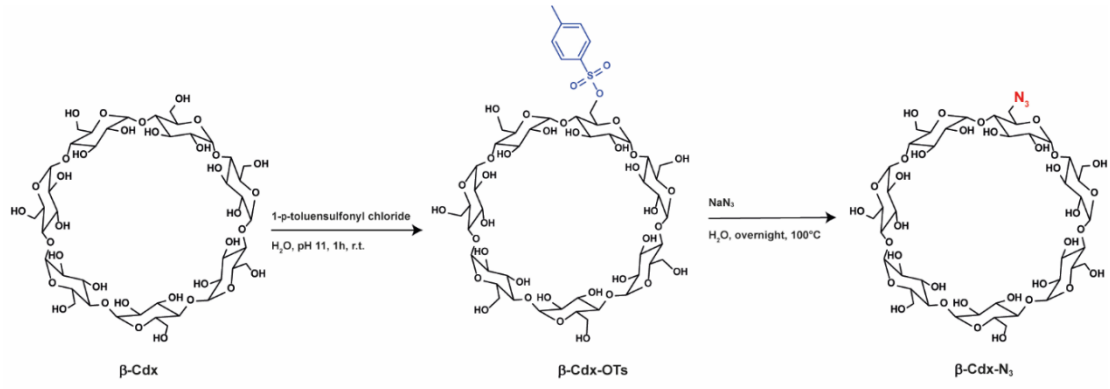

Figure 7. Synthetic pathway adopted for the monofunctionalization of β-Cdx. The mono-tosylation of β-Cdx in position 6, obtained by reaction with p-toluensulfonyl chloride in basic conditions, allowed introducing a good leaving group functional to achieve the regioselective substitution with azoture, obtaining mono-6-azido-6-deoxy-β-cyclodextrins (β-Cdx-N_3).

The ^{1}H-NMR spectrum of β-Cdx-OTs presented the characteristic aromatic peaks of the para-toluenesulfonyc group (7.74-7.72 ppm and 7.43-7.40 ppm) and a peak at 2.41ppm, attributable to the methyl group in position 9, confirming the occurred tosylation of β-Cdx. The shifting of the peaks referable to the protons in positions 5 and 6 from overlapping with water (~ 3.75 ppm) to 4.18 and 4.3 ppm respectively is coherent with the tosylation in position 6, due to the deshielding effect of the tosyl

group on adjacent protons. Furthermore, the ratio between the integrals of the peak related to the methyl group of the para-toluenesulfonyl moiety (2.41ppm) and the peak of the anomeric proton (4.8 ppm) results to be 1:7, indicating that only one monomer of the β-Cdx presents the tosyl pendant, corroborating the effective mono-functionalization (Figure 8a).

The typical groups of the tosyl- pendant described were absent in the spectrum of β-Cdx-N_3 proving that the group was successfully substituted. Moreover, by comparing the integrals of the anomeric peak (4.8 ppm) with that of the peak at 4.57 ppm, attributed to the hydroxyl group in position 6, it has been calculated that six of seven monomers present the -OH in position 6, whereas in one monomer the hydroxyl group in position 6 is effectively substituted (Figure 8b). Finally, the presence of the azido group in the structure was confirmed by the corresponding neat peak at 2100 cm^{-1} in the FT-IR spectrum of β-Cdx-N_3, which was absent in the spectrum of β-Cdx (Figure 9).

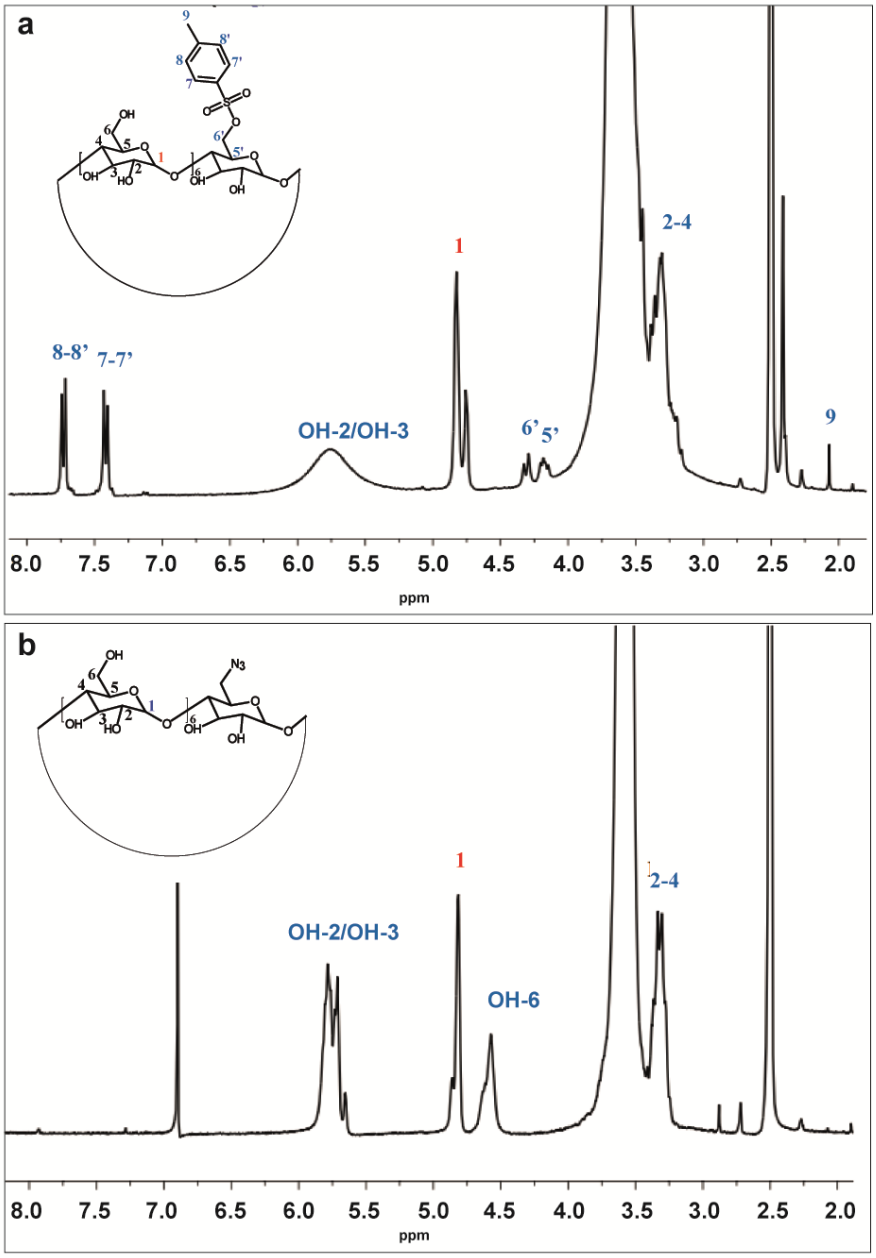

Figure 8. ^{1}H-NMR spectra of β-Cdx-OTs (a) and β-Cdx-N$_3$ (b). The substitution of the of tosyl leaving group with azoture was verified by comparing the ^{1}H-NMR spectra of β-Cdx-OTs and β-Cdx-N$_3$. The analysis was performed in DMSO-*d6* at 300.1 MHz.

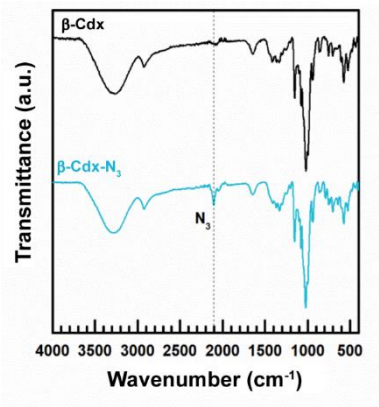

Figure 9. FT-IR spectra of β-Cdx (black) and β-Cdx-N3 (light blue). Samples were prepared as KBr pellets, and the analysis was performed in the 4000 – 400 cm^{-1} range. The dotted line highlights the appearance of the neat peak at 2100 cm^{-1}, attributable to the presence of the azido group, in the spectrum of β-Cdx-N_3.

In parallel, crystalline CDs presenting several carboxylic groups at the surface were coupled with a low molecular weight amino-PEG_4-alkyne by amide coupling, using EDC and NHS as activating agents. In the structure of the obtained CDs-PEG-CC, the PEG chain serves as a hydrophilic molecular spacer providing the alkyne terminal groups needed for the subsequent conjugation with β-Cdx-N_3 performed by 1,3 dipolar copper-catalyzed azido-alkyne Huisgen cycloaddition (Evans, 2007) (Figure 10).

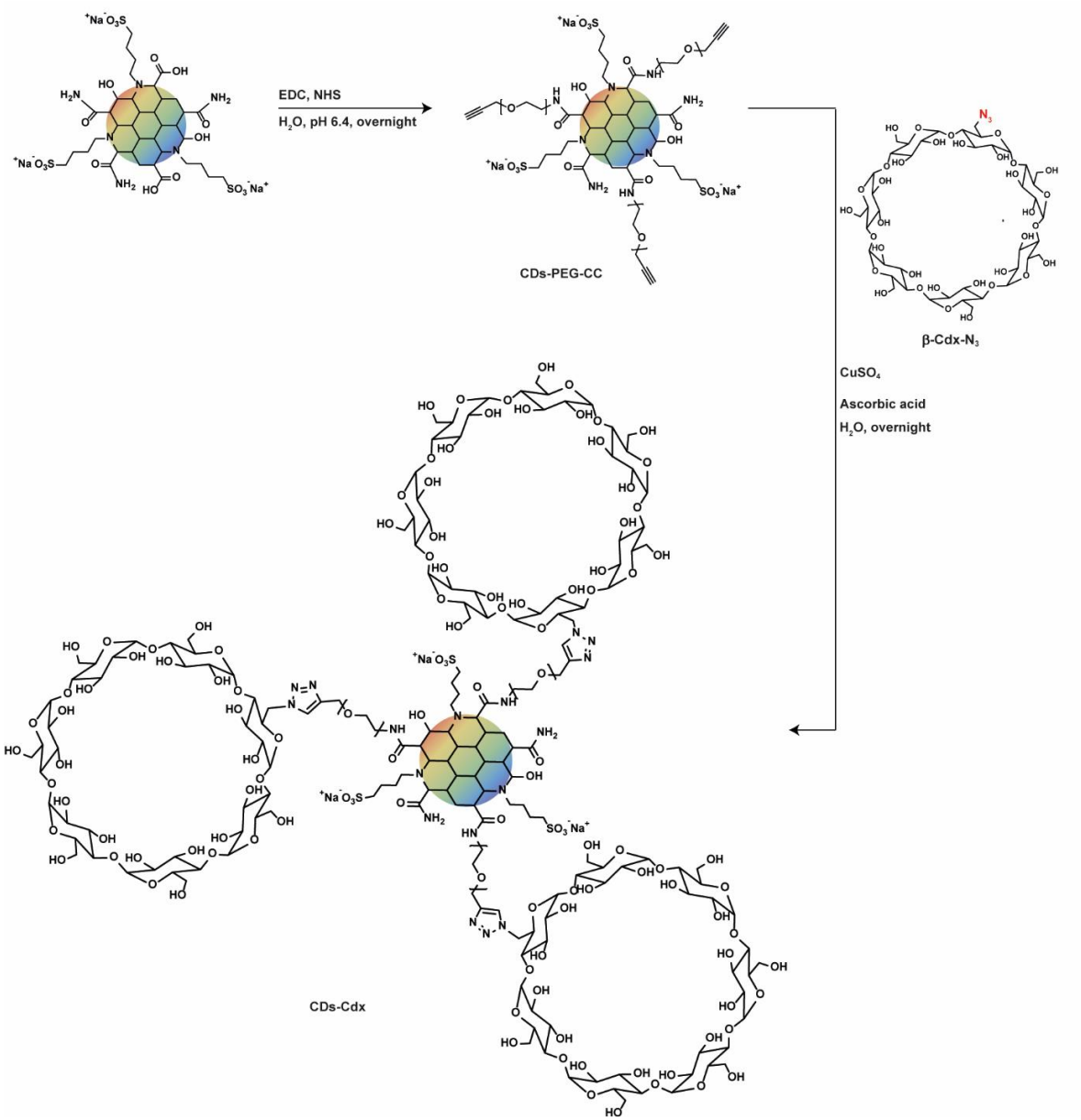

Figure 10. Scheme illustrating the synthesis of CDs-Cdx conjugates. CDs were firstly functionalized by amide coupling with amino-PEG_4-alkyne, then the alkyne terminal group of PEG chains was exploited to perform a 1,3 dipolar Cu (I) catalized Huisgen cycloaddition on the azido group of β-Cdx-N_3.

The FT-IR spectrum of CDs-PEG-CC presents the typical bands of PEG chains, related to the vibrations of C–H and C–O–C at 2950 cm^{-1} and 1100 cm^{-1}, respectively,

together with an increase in the ratio between the peaks of amide I band (1650 cm^{-1}) and the C=O stretching (1720 cm^{-1}), highlighting the formation of amidic bonds which is coherent with the PEGylation through amide coupling (Figure 11a). The characteristic peaks of the PEG spacer are also present in the FT-IR spectrum of the CDs-Cdx conjugate, which also shows the typical peaks of β-Cdx attributable to C-O-C stretching (1000 – 1300 cm^{-1}) and C-H stretching (2950 cm^{-1}). Besides, the distinctive peak of the azido group vibrations at 2100 cm^{-1}, which is evident in the spectrum of β-Cdx-N_3, is not shown in the spectrum of the conjugate, clearly demonstrating that the azido group has been involved in the linkage of PEGylated CDs with β-Cdx (Figure 11b).

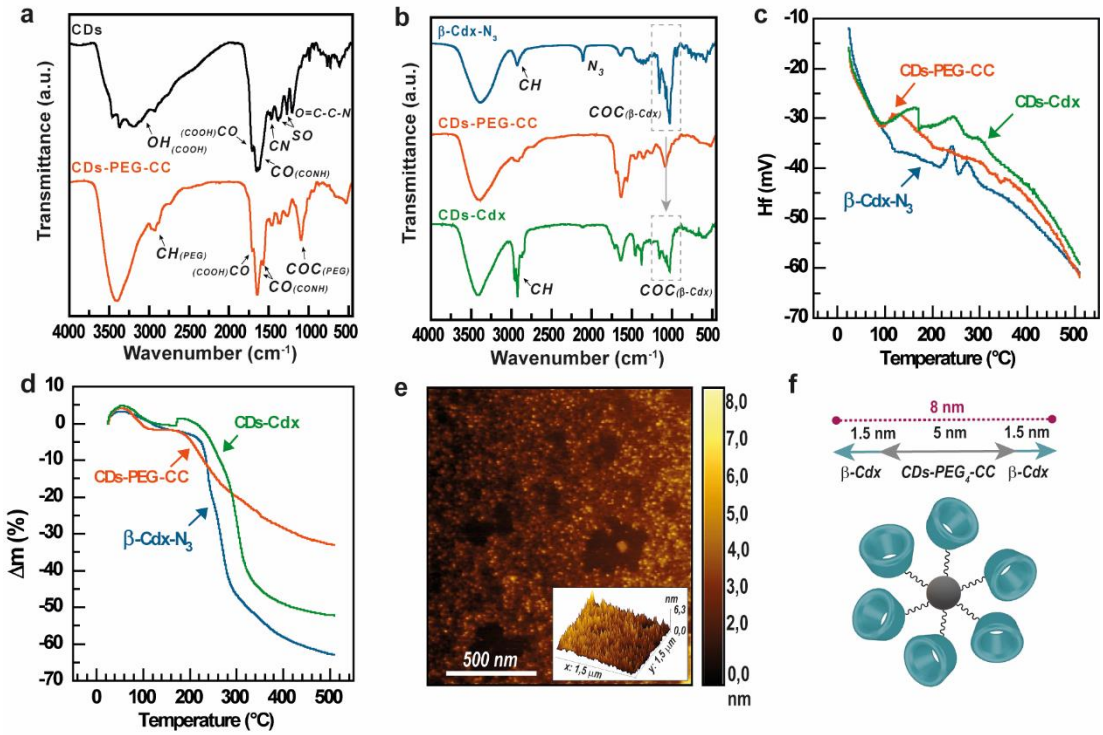

Figure 11. Physicochemical characterization of CDs-Cdx and their precursors. (a) FT-IR spectra of CDs (black) and CDs-PEG-CC (orange) and (b) FT-IR spectra of. Analyses were performed on KBr pellets of the samples and spectra were recorded in

the 4000 – 400 cm^{-1} range; (c) DSC analysis and (d) thermogravimetric analysis of CDs-Cdx (green), CDs-PEG-CC (orange) and β-Cdx-N_3 (blue), performed in the 30 – 500 °C range; (e) AFM micrograph of CDs-Cdx attained in non-contact mode (scalebar = 500 nm); (f) schematic illustration of the structure of CDs-Cdx and the corresponding average size, evaluated by analyzing the heights from the AFM data.

Further proofs of the feasibility of the synthetic pathway adopted were provided by differential scanning calorimetry (DSC) and thermogravimetric analysis (TGA) (Figure 11c-d). In particular, the thermograms of CDs-PEG-CC and β-Cdx-N_3 display characteristic exothermic transitions at 130 °C and 230-270 °C, respectively. The transition of CDs-PEG-CC corresponds to a negligible weight loss at the corresponding temperatures by TGA (< 2%), followed by a weight loss from 180°C to 550°C (-32%), whereas β-Cdx-N_3 displays a sudden weight loss in the 230-270 °C range, owing to decomposition phenomena. The conjugate CDs-Cdx undergoes very similar transitions, resulting in a complex thermogram in which, however, the exothermic peaks are slightly shifted to high temperatures (240 – 286 °C), indicating a higher thermal stability that is compatible with a covalent conjugation. To estimate the number of β-Cdx moieties linked at the surface of CDs, we compared the enthalpy values of the peaks at 240 and 286 °C with those of bare β-Cdx-N_3, calculating that β-Cdx represent roughly 35 % on weight basis of the conjugate, corresponding to seven β-Cdx per CDs.

The diameter and size distribution of CDs-Cdx were assessed by atomic force microscopy (AFM). AFM micrographs, reported in Figure 11e, show spherical objects of 8.1 ± 0.2 nm diameter with homogeneous distribution. Considering that the average

diameter of plain CDs was 5.1 ± 0.3 nm, there is a 3 nm increase in the average diameter of the nanoparticles after the conjugation, which perfectly corresponds with the presence of 400 Da PEG chains functionalized with β-Cdx (1.5 nm). Thus, the structure of CDs-Cdx can be described as a core-shell organized nanoparticle presenting CDs as central element passivated with PEG-β-Cdx chains, as illustrated in Figure 11f. The absence of aggregates suggests that the adopted synthetic protocol prevented the formation of dot-to-dot crosslinking phenomena, observed in the literature as a cause of heterogeneity in similar nanostructures. Indeed, because of the multifunctionalities of β-Cdx represented by their multiple hydroxyl groups, simpler conjugation protocols may lead to nanoparticles with broader size distribution (Espina-Casado et al., 2021; Yang et al., 2019). Therefore the importance of obtaining mono-functionalized β-Cdx-N_3 bearing only one azido group which can react only with one dot, avoiding undesired crosslinking. Instead, CDs having several alkynes functions at the surface can react with several β-Cdx, leading to the final nanostructure obtained.

The ultrasmall size of CDs-Cdx (<10 nm) is desirable for ensuring its rapid diffusion throughout the stiff TME and into the tumor parenchyma. On the other hand, the diameter higher than the renal cut-off (5 nm) prevents early elimination, conferring optimal properties for drug delivery purposes (Goel et al., 2019).

The conjugate CDs-Cdx is also endowed with interesting optical properties, including multicolor absorption and fluorescence emission. The absorption spectrum of CDs-Cdx extends all along the UV/Visible region up to 750 nm, with multiple main peaks at 345, 440, and 560 nm, corresponding to electronic transitions occurring at the surface of carbon dots already observed in the spectra of the precursors (CDs and CDs-

PEG-CC), and well-established in the literature (Scialabba et al., 2019; Sciortino, Mauro, et al., 2018) (Figure 12a). Thus, the passivation of CDs with PEG and β-Cdx did not impinge on the electronic states of CDs from which the unique optical properties of these nanoparticles arise. In particular, the surface conjugation with β-Cdx by 1-4 triazoles preserves the extended optical absorption towards the red/NIR region obtained by sulfur-doping, thus allowing NIR-triggered photothermal applications. CDs-Cdx also display a bright multicolor fluorescence, with main emission peaks at 450 and 530 nm, and a tail extending to the red region, which is suitable for bio-imaging applications (Weissleder, 2001)(Figure 12b-b')

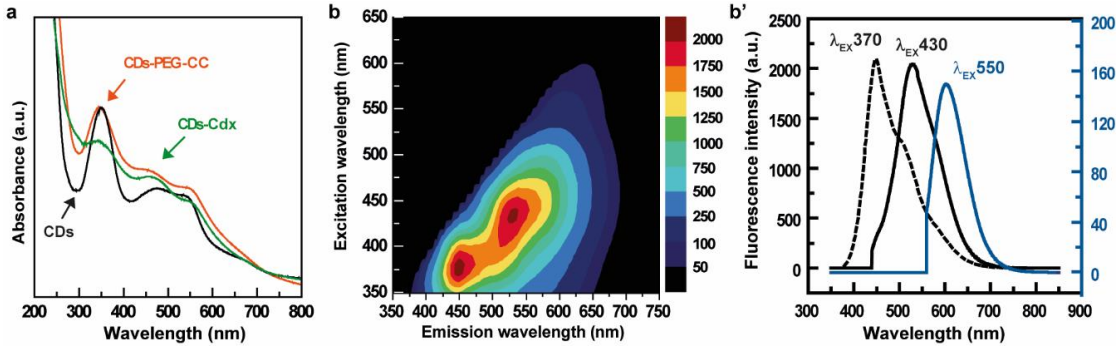

Figure 12. Optical properties of CDs-Cdx and their precursors. (a) UV-visible absorption spectra of aqueous solutions of CDs-Cdx (green), CDs-PEG-CC (orange) and CDs (black), recorded in the 800 – 200 nm range. (b) 3D emission spectrum of CDs-Cdx in the 350-750 nm range, obtained by exciting an aqueous solution of the sample in the 350 – 650 nm range. (b') Focus on the 2D emission spectra of CDs-Cdx attained by exciting the samples at 370, 430, and 550 nm.

3.1.2. The CDs-Cdx conjugates enable the controlled delivery of sildenafil

CDs-Cdx conjugates were employed for loading sildenafil citrate with the aim of promoting positive reinforcement of CDs-mediated ROS production damaging tumor cells and enhancing the passive accumulation of the nanosystem by EPR effect, favored by the drug effect on vasculature. The loading should be endorsed by the ability of β-Cdx to form inclusion complexes with drugs. We prepared CDs-Cdx loaded with sildenafil (CDs-Cdx@sildenafil) using the kneading method, using mechanical pounding to obtain a homogeneous dispersion of the nanosystem and the drug in a volatile solvent (ethanol/water) which evaporates during the procedure, forming a thin film. Then we resuspended the mixture in water and removed the drug excess by filtration and dialysis. The drug loading calculated, established by HPLC analysis, was 20.6 %.

In a medium mimicking physiological conditions, CDs-Cdx@sildenafil released the drug payload in a controlled fashion up to 48 h. Indeed, the drug release profile, reported in Figure 13, shows that after 10 h of incubation 55 % of Sildenafil was released from the nanosystem, then the curve reached a quasi-plateau resulting in a maximum release of 70 % after 48 h. This trend results more controlled over the simple diffusion of the drug, which reaches 87 % already within the first 10 h. Therefore, the long-lasting reversible interaction between sildenafil and CDs-Cdx provides a suitable release profile for ensuring the accumulation of the drug at the site of action. Since sildenafil/β-Cdx complexes present a quite low binding constant (150 M^{-1}), the sustained release obtained should be ascribed to the host's binding phenomena involving the CDs-Cdx nanostructure (Al Omari et al., 2006).

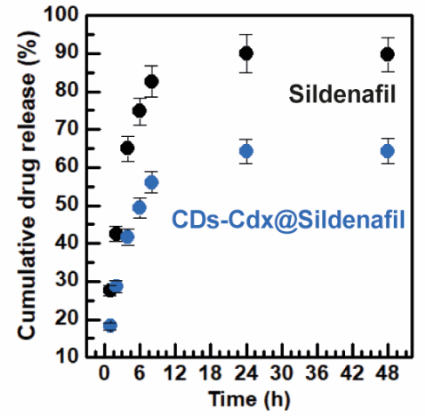

Figure 13. Drug release kinetics of sildenafil from CDs-Cdx@Sildenafil (blue) compared with the free diffusion of sildenafil (black). The study was performed by evaluating the diffusion of sildenafil from a dialysis tube (MWCO 1kDa) in a medium consisting of 1% Tween 80 PBS solution (pH 7.4). The concentration of sildenafil in the external medium was evaluated at scheduled times by HPLC analysis. Data are reported as mean ± SD (N = 3).

3.1.3. The intracellular distribution of CDs-Cdx implies distinct cytotoxic effects on different cell lines

Exploiting the self-tracking properties of CDs-Cdx we evaluated their cellular uptake by healthy (NHDF), pre-tumoral (16-HBE), and breast cancer (MCF-7) cells *in vitro*, after 24 h of incubation. CDs-Cdx efficiently entered all tested cell lines after 24h, although displaying different intracellular localization between cancerous and non-cancerous cells. Indeed, the brilliant fluorescence of the nanosystem enabled following the cellular internalization in the blue, green, and red channels with high spatial resolution, allowing to distinguish the preferential accumulation of CDs-Cdx in intracellular compartments (Figure 14). In particular, in breast cancer cells the nanosystem displays a prevalent accumulation within the nuclei, showing also spots

of brilliant blue fluorescence all around the cytosol which were slightly visible in the green and red channel, suggesting an interaction with cell vesicles that influences the fluorescence intensity at different wavelengths (Fig. 14 a-a^{V}). Instead, CDs-Cdx diffuse throughout the cytosol in NHDF and 16-HBE, with negligible fluorescence detectable in the nuclei (Fig. 14 b-b^{V}, c-c^{V}). The different localization among the tested cells implies that the sildenafil payload may be released in diverse districts causing the inhibition of PDE-5, thus providing different effects between cancerous and non-cancerous cells.

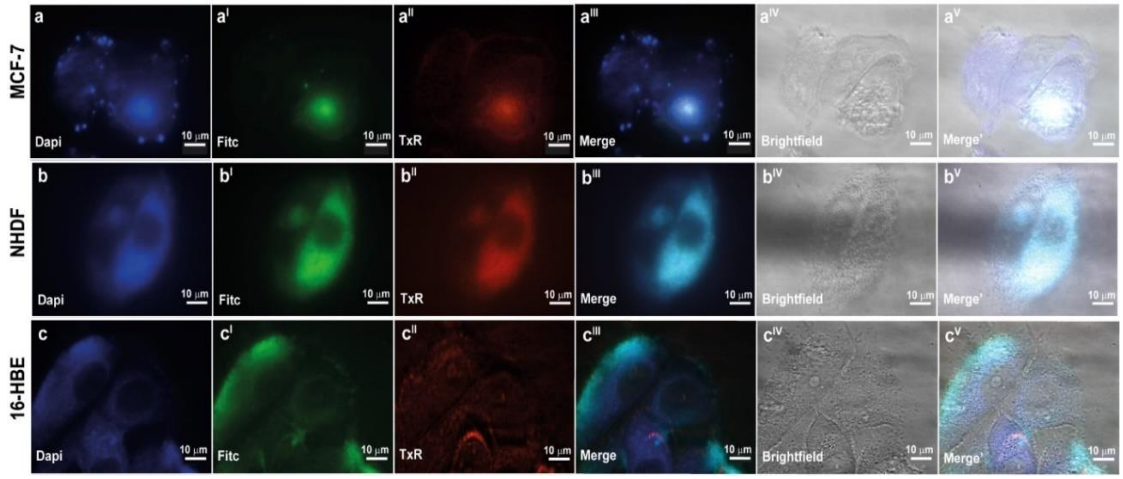

Figure 14. Cellular uptake CDs-Cdx on human breast cancer (MCF-7, a-a^{V}), human bronchial pre-cancerous (16-HBE, b-b^{V}), and human healthy dermal fibroblast (NHDF, c-c^{V}) evaluated by widefield fluorescence microscopy. Cells were incubated with CDs-Cdx in DMEM (0.15 mg mL^{-1}) for 24h at 37°C. The blue, green, and red fluorescence, appreciable in the Dapi (a,b,c), Fitc (a',b',c'), and TexasRed (TxR, a'',b'',c'') channels respectively, is only due to the multicolor self-photoluminescence of CDs-Cdx; (a''', b''', c''') Merge of the three fluorescence

channels, (a^{IV}, b^{IV}, c^{IV}) brightfield optical signals, and (a^{V}, b^{V}, c^{V}) merges of fluorescent channels with brightfield signals.

Before assessing the role of sildenafil-loaded nanoparticles in eliciting a selective antitumoral response by enhancing the ROS pathway, we evaluated the cytocompatibility of the plain vehicle. To this aim, NHDF, 16-HBE, and MCF-7 cells were incubated with increasing concentrations of CDs-Cdx (10 - 250 μg mL^{-1}) for 24h or 48h, then the cell viability was evaluated by MTS assay. Results, reported in Figure 15 a-a', clearly demonstrate that the nanosystem is plenty cytocompatible for NHDF cells, while a slight cytotoxic effect can be observed for 16-HBE and MCF-7 cells at the higher concentration, reaching 84 % and 74 % of cell viability respectively after 24 h, and 81 % and 67 % after 48 h. Therefore it emerges an inherent and selective anticancer effect of CDs-Cdx, attributable to selective ROS production in cancerous and pre-cancerous cell lines due to the interaction of sulfur-doped carbon nanodots with the electron transport chain in the mitochondrial membrane, which causes a massive production of ROS already reported in the literature (Mauro, Utzeri, Sciortino, et al., 2022).

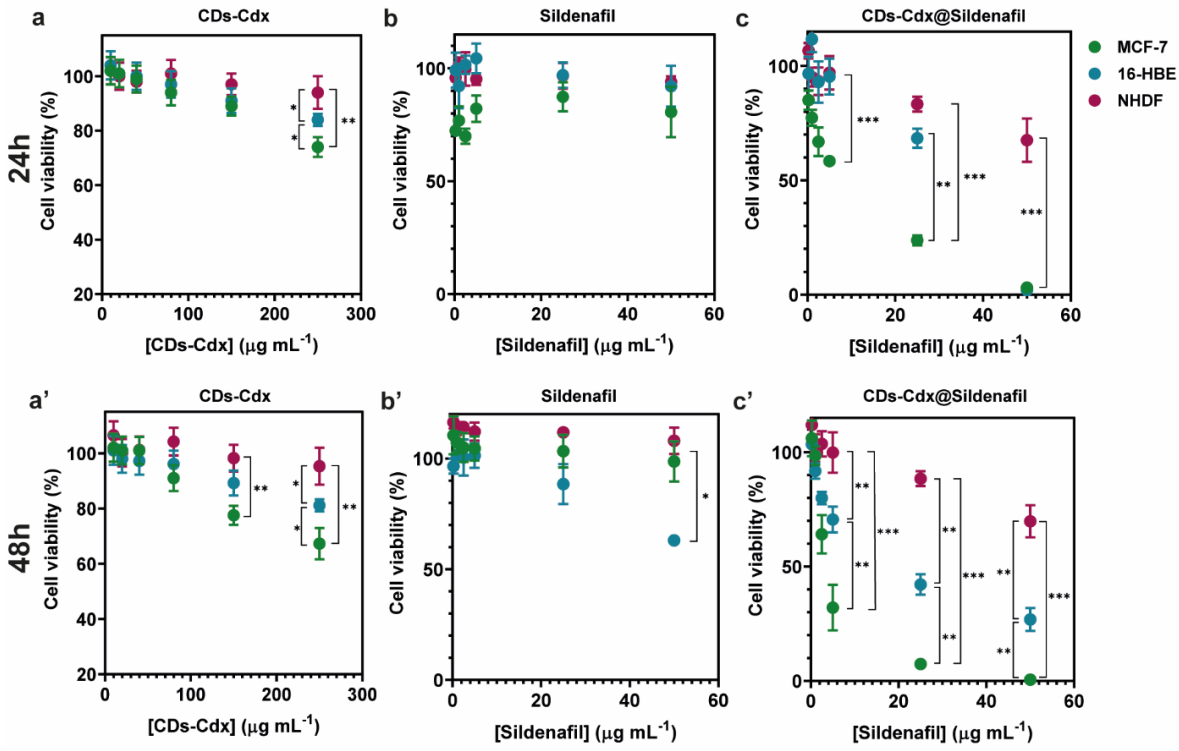

Figure 15. Cytotoxicity studies on human breast cancer (MCF-7, green), human bronchial pre-cancerous (16-HBE, blue), and normal human dermal fibroblast (NHDF, purple) evaluated by MTS cell viability assay. Cell viability for CDs-Cdx conjugates after 24 h (a) and 48 h (b) of incubation. Cell viability for free sildenafil after 24 h (a) and 48 h (b) of incubation. Cell viability of CDs-Cdx@sildenafil at equivalent drug concentration of free sildenafil, after 24 h (a) and 48 h (b) of incubation. Data are reported as mean ± SD (N = 3).

Besides, the incubation with sildenafil as a free drug did not impinge on cell viability, with the only exception of a significant decrease of 16-HBE cell viability at the higher concentration tested (50 μg mL^{-1}) after 48 h (Figure 15 b-b'). This particular behavior can be due to the overexpression of the target PDE-5, which has been reported to synergize with cGMP-mediated production of ROS, causing an enhanced cytotoxic effect.

Interestingly, incubating cells with CDs-Cdx@Sildenafil at equivalent drug concentration we observed a huge decrease in cell viability, especially regarding MCF-7 cells which showed cell death > 97% at the higher concentration. Whereas the nanosystem provoked only a slight decrease in NHDF cell viability, a significant toxic effect was also displayed by 16-HBE, reaching 2 % cell viability after 24h of incubation, and 26 % after 48 h (Figure 15 c-c'). The difference between the cytotoxic effect induced in pre-cancerous 16-HBE and breast cancer MCF-7 cells is more evident considering the half-maximal effective concentrations (EC50) reported in Table 2, which is about four-fold bigger for MCF-7 if compared with 16-HBE cells. Moreover, the EC50 of CDs-Cdx@Sildenafil at 24 h is almost two-fold bigger than at 48h, highlighting a time-dependent efficacy.

Cell line	**Sample**	$\boldsymbol{EC_{50}^{24h}}$ (μg mL^{-1})	$\boldsymbol{EC_{50}^{48h}}$ (μg mL^{-1})
NHDF	Sildenafil	> 50	> 50
	CDs-Cdx@sildenafil	> 50	> 50
16-HBE	Sildenafil	> 50	> 50
	CDs-Cdx@Sildenafil	31	16
MCF-7	Sildenafil	> 50	> 50
	CDs-Cdx@Sildenafil	8	4

Table 2. Half-maximal effective concentrations values after 24 h ($\boldsymbol{EC_{50}^{24h}}$) and 48h ($\boldsymbol{EC_{50}^{48h}}$) of incubation with either free sildenafil or CDs-Cdx@sildenafil at equivalent drug concentration. Values were calculated by plotting the dose-response fitting obtained from the experimental points of the cytotoxicity studies and performing interpolation for y = 50 % (OriginLab Software 8.5, $R^2 > 0.993$).

Overall, from cell viability evaluations emerges an enhanced effect of CDs-Cdx@Sildenafil towards cells overexpressing PDE-5, which are more sensitive to sildenafil-mediated inhibition in combination with CDs-Cdx mediated cytotoxic effect. These results are also coherent with the observed faith of the nanosystem after cellular internalization, indicating that the delivery of the payload to different intracellular compartments influences the outcome of sildenafil action, contributing to a selective anticancer effect.

3.1.4. CDs-Cdx@Sildenafil promote ROS production and upregulation of ROS-related genes

Presuming a critical role of ROS production in the synergistic effect observed, we investigated the total amount of ROS in cells treated with CDs-Cdx, sildenafil, or CDs-Cdx@sildenafil for 24 h or 48 h. As reported in Figure Ja-a', both CDs-Cdx and the free drug provoke a feeble increment of ROS level, as expected for sulfur-doped carbon nanodots and coherently with the literature. The enhancement of ROS production is exacerbated when sildenafil is delivered by CDs-Cdx, resulting in about 3-4 fold higher ROS levels in MCF-7 and 16-HBE compared to cells treated with the free drug or the empty vehicle. Moreover, the ROS production in NHDF was 1-2 fold lower compared to pre-cancerous and cancerous cells, corroborating the higher sensitivity of PDE-5 overexpressing cells to the treatment. Altogether these results indicate that the specific action of CDs-Cdx@Sildenafil towards cancerous and pre-cancerous cells derives from a combination of concomitant factors, including the peculiar intracellular distribution of the nanosystem, the sildenafil-mediated signaling, and the overexpression of PDE-5.

Subsequently, we performed a gene expression analysis to evaluate the mRNA expression of 24 genes involved in oxidative stress signaling to evaluate the sustained production of ROS in the MCF-7 cell lines following sildenafil, CDs-Cdx, or CDs-Cdx@Sildenafil treatments. The genes of this pathway-specific analysis were selected based on their role in ROS signaling, including ROS metabolism (ALOX12, NOS2, SOD1, SOD2, TXN, c), antioxidants (CAT, GPX, GSR, GSTP1, PRDX1, PTGS2), oxidative stress-responsive genes (AKR1C2, FTH1, GCLC, GCLM, HMOX1, NQO1, SQSTM1), and genes involved in the DNA damage and repair mechanisms (ATR, CHEK1, GADD45A, MRE11A, RAD51). Data reported in Figure Jb confirm that CDs-Cdx are cytocompatible and do not impinge on mitochondrial homeostasis, since only two genes over 24 were two-folds upregulated after 24 h of incubation, whereas the expression levels were similar to untreated MCF-7 cells, or slightly downregulated after 48 h.

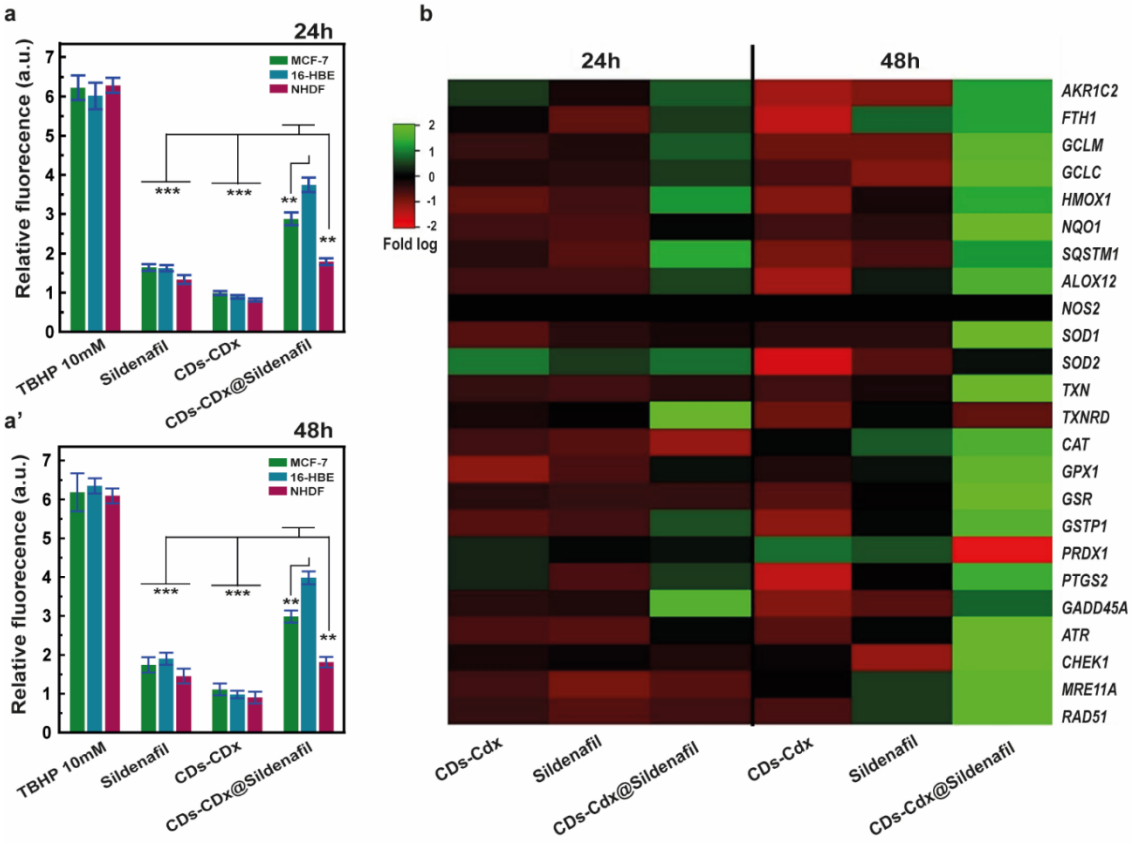

Figure 16. Evaluation of the impact of CDs-Cdx and CDs-Cdx@Sildenafil on ROS production and ROS signaling. Relative amount of ROS produced by human breast cancer (MCF-7, green), human bronchial pre-cancerous (16-HBE, blue), and human healthy dermal fibroblast (NHDF, purple), after 24 h (a) and 48 h (a') of incubation. Values are expressed as mean ± SEM (N = 3). Gene expression analysis of ROS-triggered signaling on the breast cancer cell line MCF-7 (b); the heat map from red (low) to green (high) represents the mRNA levels of analyzed genes in the presence of CDs-Cdx, sildenafil, and CDs-Cdx@Sildenafil, after 24 h and 48 h of incubation. Data are presented as fold-changes in log (2) transformed values.

Likewise, sildenafil treatment did not affect the ROS signaling since the expression pattern does not highlight significant changes among the analyzed genes after 24h. The

effect of sildenafil on ROS production emerges after 48 h of incubation, resulting in significant upregulation of genes involved in ROS metabolism, antioxidant response, and DNA damage.

As expected, unlike free drug and plain CDs-Cdx, CDs-Cdx@Sildenafil induced considerable changes in gene expression patterns already after 24 h, inducing from 2- to 20-fold increased mRNA levels in 12 genes. In detail, we recorded an upregulation of ALOX12, SOD2, and TXNRD, involved in ROS production and metabolism, as well as an enhancement of antioxidant and stress-induced response mediated by FTH1, GCLM, GCLC, HMOX1, SQSTM1, GSTP1, PTGS2, and DNA repair signaling (GADD45). After 48h, the levels of gene expression of all the pathways analyzed were further increased, reaching 10—250-fold in mRNA levels. Such massive upregulation of oxidative stress signaling together with the higher measured ROS levels following CDs-Cdx@Sildenafil treatment definitely validates the ability of the nanosystem to trigger oxidative stress in exposed breast cancer cells.

3.2. Leveraging the inherent anticancer properties of carbon nanodots with IDO-pathway inhibition to perform dual-mode breast cancer immunotherapy

3.2.1. Synthesis of carbon nanodots/indoximod conjugates exhibiting multicolor self-fluorescence

Carbon nanodots (CDs, 5.3 ± 0.4 nm), prepared as described by Mauro et al. (2022), were conjugated with indoximod through a biocompatible spacer in a three-step synthetic protocol. Firstly, CDs were functionalized with a bis-amine poly(ethylene glycol) (PEG) by amide coupling, using EDC and NHS as activating agents. The PEG coating should improve the circulation time of the nanosystem by forming a hydrophilic shell that increases the hydrodynamic diameter of CDs above the renal cutoff of 5.5 nm and mitigates opsonization and protein corona adhesion, thus preventing its early elimination and increasing its bioavailability (Schipper et al., 2009). The terminal amine group of the polymer chains at the CDs-PEG surface was exploited for the subsequent reaction with citraconic anhydride, causing the opening of the ring-anhydride to obtain a free carboxylic terminal group required for the conjugation with indoximod by amide coupling, using again EDC and NHS as activating agents.

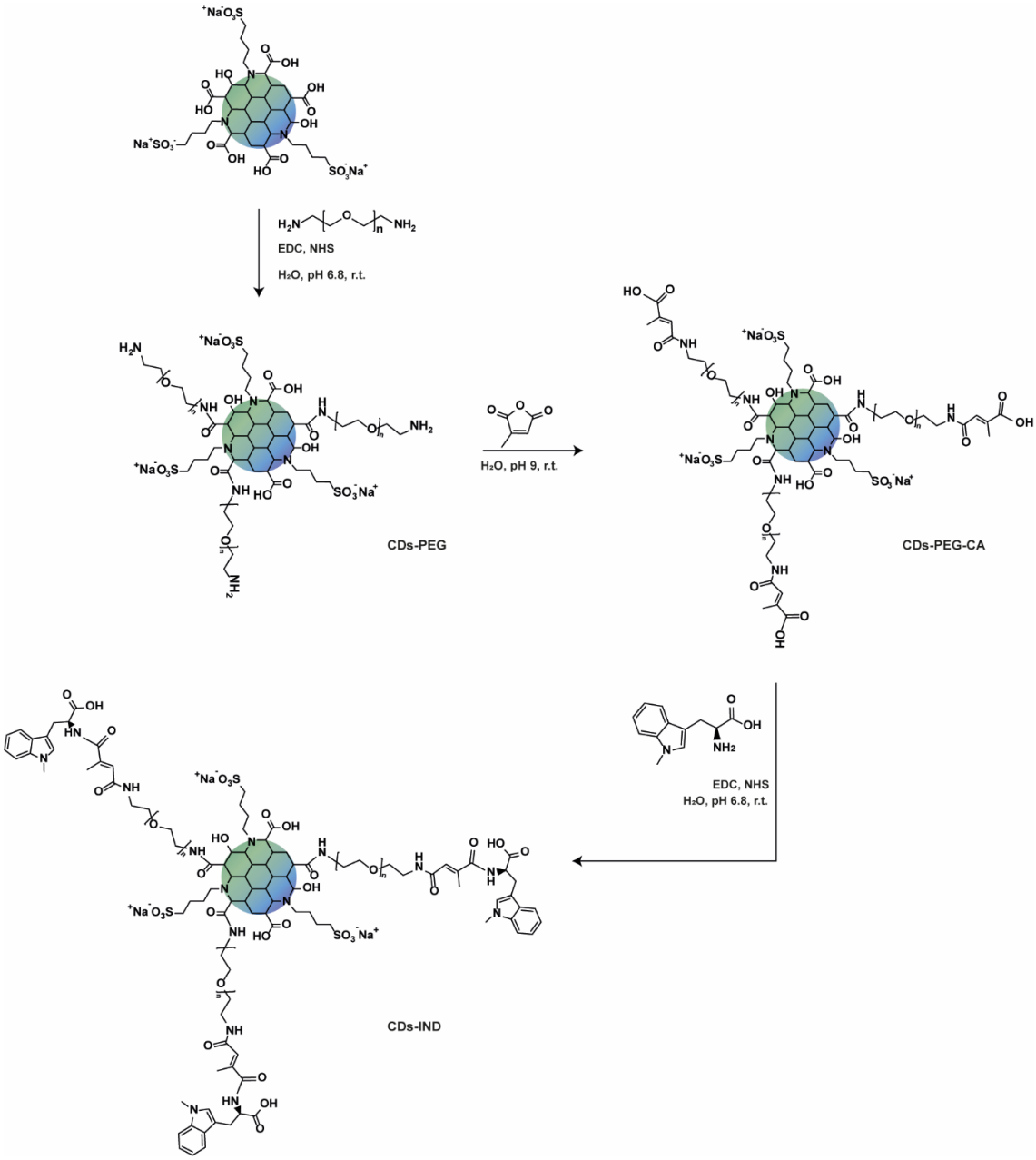

Figure 17. Synthetic pathway of CDs-IND. In the first step, CDs were PEGylated by amide coupling with a bis-amine PEG. Subsequently, the insertion of the citraconate pendant by reaction with citraconic anhydride in basic conditions provides the carboxyl-terminal group needed for the final coupling with indoximod, achieved by amide coupling.

The feasibility of the surface functionalization was established by FT-IR and ^{1}H-NMR comparing the spectra of CDs-IND and its precursors. As shown in Figure 18, the spectrum of CDs-PEG presents the typical bands associated with the presence of PEG, consisting of a diagnostic C-O-C vibration (1104 cm^{-1}) and the aliphatic bands related to C-H vibrations (2890 - 1460 cm^{-1}), which were instead absent in the spectrum of bare CDs. The formation of the amide bond was confirmed by considering the intensity ratio between the peak attributed to carboxylic asymmetric stretching (1712 cm^{-1}) and the amide I band peak (1635 cm^{-1}) in the spectra of CDs and CDs-PEG, which resulted in a shift in favor of the formation of amide bonds after the conjugation. Moreover, the intensity reduction of carboxylic symmetric stretching (1385 cm^{-1}) together with the concomitant increase of C-N vibration (1352 cm^{-1}) further confirms the success of amide coupling. The relative intensity increment of peaks related to of the C-N vibration band (1352 cm^{-1}) and of the amide I band (1640 cm^{-1}) was enhanced by the reaction with with citraconic anhydride, coherently with the formation of new amide bonds. Furthermore, the peak at 1585 cm^{-1} attributable to C=C stretching of α,β-unsaturated carbonyl confirms the formation of the citraconate pendant. A further increase of the relative peaks of amide bond was observed in the spectrum of the conjugate CDs-IND, which also occurred by amide coupling.

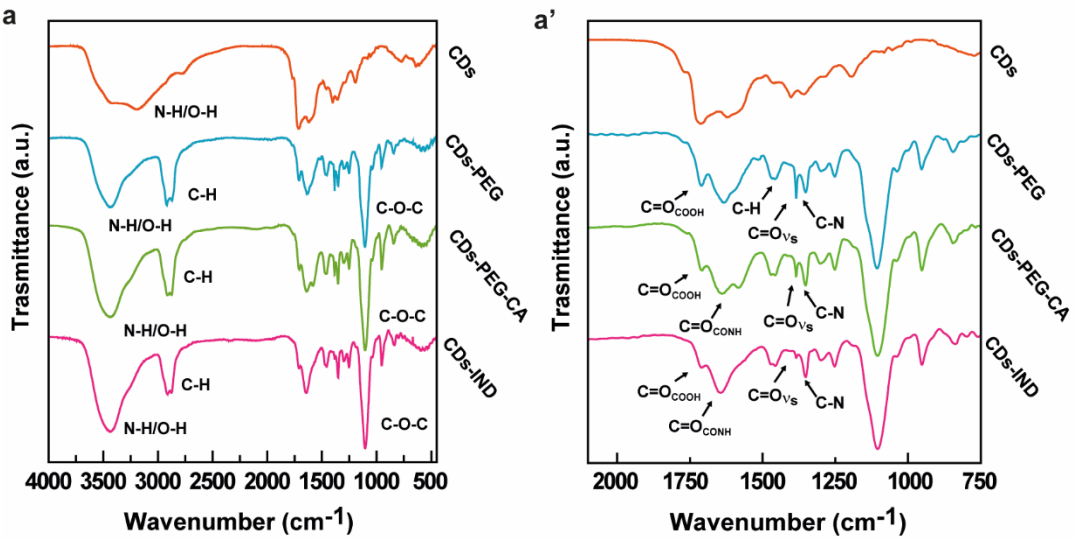

Figure 18. FT-IR spectra of CDs-IND and precursors confirming the proficiency fo the synthetic pathway. (a) FT-IR spectra of CDs (orange), CDs-PEG (blue), CDs-PEG-CA (green), CDs-IND (pink), prepared as KBr pellets and analyzed in the 4000 – 400 cm^{-1} range. (a') Magnification of the same spectra in the 2400 – 750 cm^{-1} range.

The distinctive peaks of PEG repeating units (3.88 – 3.55 ppm) are clearly visible in the ^{1}H-NMR spectrum of CDs-PEG, CDs-PEG-CA, and CDs-IND, corroborating the FT-IR data. ^{1}H-NMR analysis also confirmed the formation of CDs-PEG-CA indicated by the neat peaks at 1.97 ppm and 5.74 ppm, which are attributable to the methyl group and the hydrogen of the citraconate pendant, respectively. Finally, the presence of IND in the structure of the final nanosystem was confirmed by the 7.0 – 7.78 ppm peaks integrating for the 4H of the aromatic ring of IND in the ^{1}H-NMR spectrum of CDs-IND.

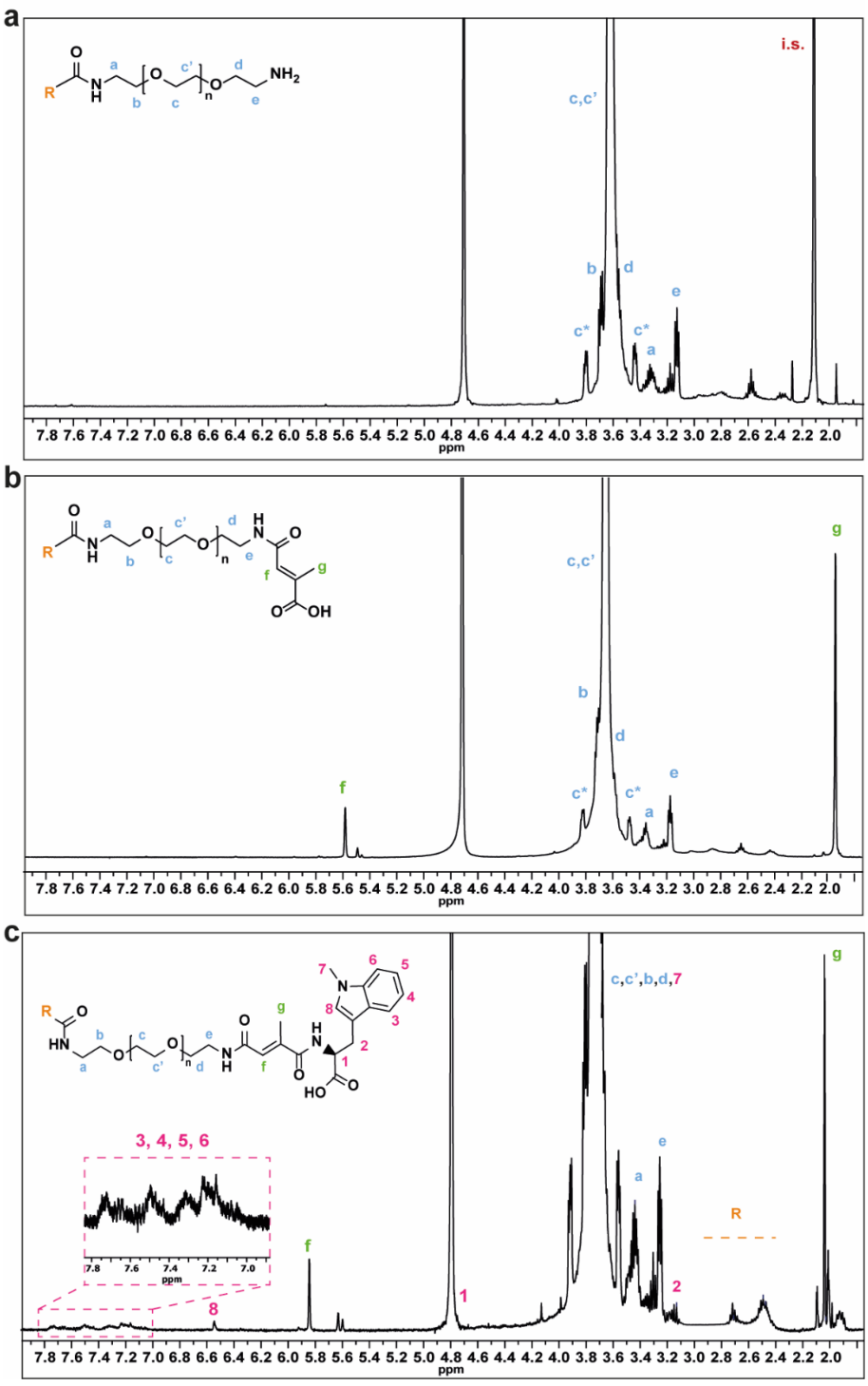

Figure 19. ^{1}H-NMR spectra of CDs-PEG (a), CDs-PEG-CA (b), and CDs-IND (c). i.s. in the spectrum CDs-PEG indicates the peak associated to acetone, used as an internal standard. Spectra were recorded in D_2O operating at 400.15 MHz.

The amount of polymer chains in CDs-PEG was evaluated both by ^{1}H-NMR, using acetone as an internal standard (Figure 19 a), and spectroscopically by performing a ninhydrin assay to calculate the amount of primary amine, which directly correlates to the amine end-chain of the PEG pendants. Combining both methods, it was calculated that CDs-PEG conjugates presented 0.3 mol of PEG per mg.

To evaluate the percentage of PEG chains presenting the citraconate pendants in CDs-PEG-CA we considered the ratio between the diagnostic peaks of PEG repeating units (3.88 – 3.55 ppm) and the peak attributed to the methyl group of citraconate (1.97 ppm) (Figure 19 b). Thus we calculated that 45 % of PEG chains present the citraconate pendant. Similarly, we referred to the ratio between the aromatic hydrogens of IND (7.0 – 7.78 ppm) and PEG repeating units (3.88 – 3.55 ppm) to assess that 13 % of side chains present the IND terminal moiety, which is calculated as 7.7 μg of IND per mg of nanosystem (Figure 19 c).

Atomic-force microscopy (AFM) of CDs-IND displayed homogeneous spherical objects with an average diameter of 6.6 ± 1.7 nm and a narrow size distribution (Fig. 20 a-a', b). The conjugate resulted highly stable, indeed only 18% of the drug payload was released after 10 days under physiological conditions mimicking the pH of bloodstream (7.4), tumor microenvironment (TME) (6.4), and cancer endosomes (5.5) (Fig. 20 c).

The surface functionalization of CDs did not compromise their unique optical properties. Indeed, the absorption spectra of CDs-PEG, CDs-PEG-CA, and CDs-IND maintained the same profile of plain CDs, characterized by broad and complex absorption spectrum extending all along the UV-visible region. However, the main

absorption peaks of CDs at 340 nm and 550 nm underwent a feeble red shift following surface functionalization, while the peak at 460 nm lost its definition (Figure 20 d). Since these main peaks are usually referable to electronic transitions occurring at the surface of nanoparticles, the slight differences observed are coherent with changes of the electronic state due to the surface passivation with polymers, as extensively described in the literature

The ability of CDs to absorb light in a wide range of wavelengths results in brilliant multicolor photoluminescence. The 3D emission spectrum of CDs-IND, recorded by exciting the sample in the 340 – 650 nm range, show with main emission peaks in the blue-green region, specifically at 445 nm and 540 nm (λ_{EX} 370 nm and 450 nm respectively), and a tail extending into the red region (Fig. 20 e). The inherent photoluminescence of CDs-IND confers self-tracking properties to the nanosystem, enabling its monitoring by bioimaging *in vitro*.

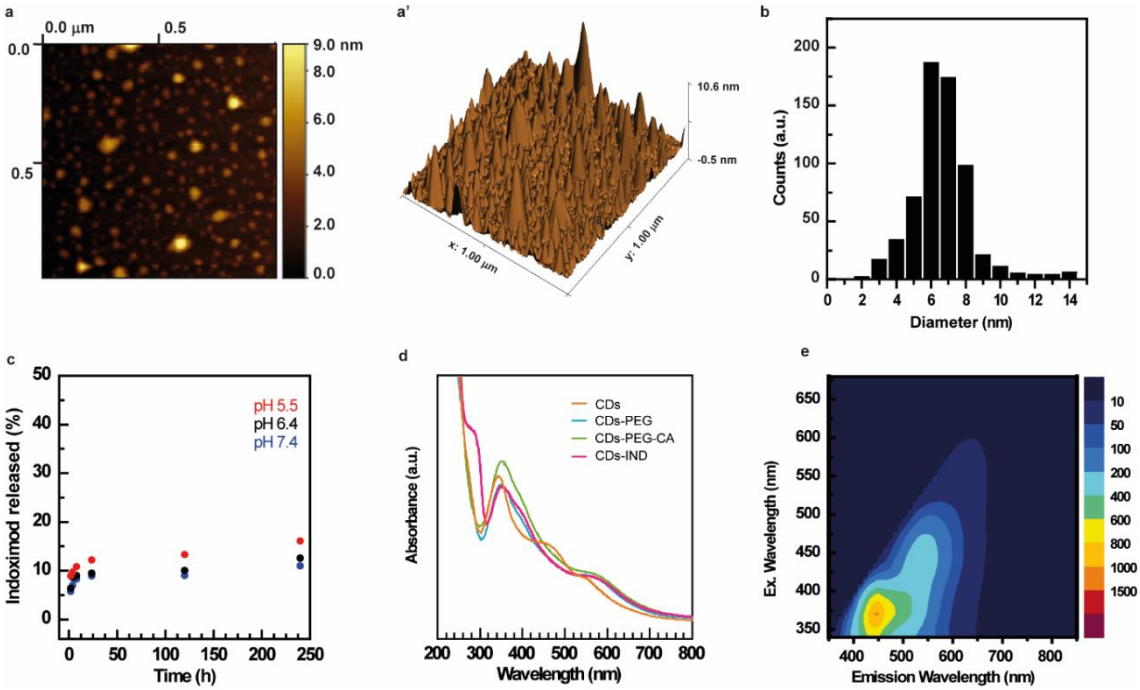

Figure 20. Physicochemical characterization of CDs-IND and their precursors. (a) Atomic force microscopy (AFM) micrograph and (a') 3D reconstruction of AFM signal of CDs-IND. (b) Size distribution obtained from the analysis of AFM heights. (c) Evaluation of CDs-IND stability in buffered solutions at pH 5.5 (red), 6.4 (black), and 7.4 (blue) performed by HPLC analysis. (d) UV-visible absorption spectra of CDs (orange), CDs-PEG (blue), CDs-PEG-CA (green), and CDs-IND (pink), recorded in the 200-800 nm range. (e) 3D emission spectrum of CDs-IND aqueous solution recorded in the 350 – 850 nm range (λ_{EX} 340 – 680 nm).

3.2.2. The conjugation with indoximod does not compromise the inherent antitumoral properties of carbon nanodots *in vitro*

The self-tracking fluorescence of CDs-IND in the green region was exploited to monitor their cellular uptake in a murine mammary cancer cell line (E0771). Cells were incubated for 24 h, 48 h, and 72 h, then nuclei were stained with Hoechst 33342 dye. Micrographs acquired by confocal microscopy show that CDs-IND can enter the cytosol of E0771 already after 24 h, with a maximum accumulation after 48 h corresponding to the maximum intensity of the green fluorescence signal (Figure 21). The amount of CDs-IND within the cells decreases after 48 h, but a feeble signal is still appreciable up to 72 h, confirming the ability of the nanosystem to be retained in cancer cells for at least 3 days. The overlap of blue and green signal did not occurred, indicating that CDs-IND did not diffuse into the cellular nuclei.

Notably, uptake studies were conducted without labeling the nanosystem with any fluorescence dye corroborating the self-tracking ability of CDs-IND for *in vitro* evaluations.

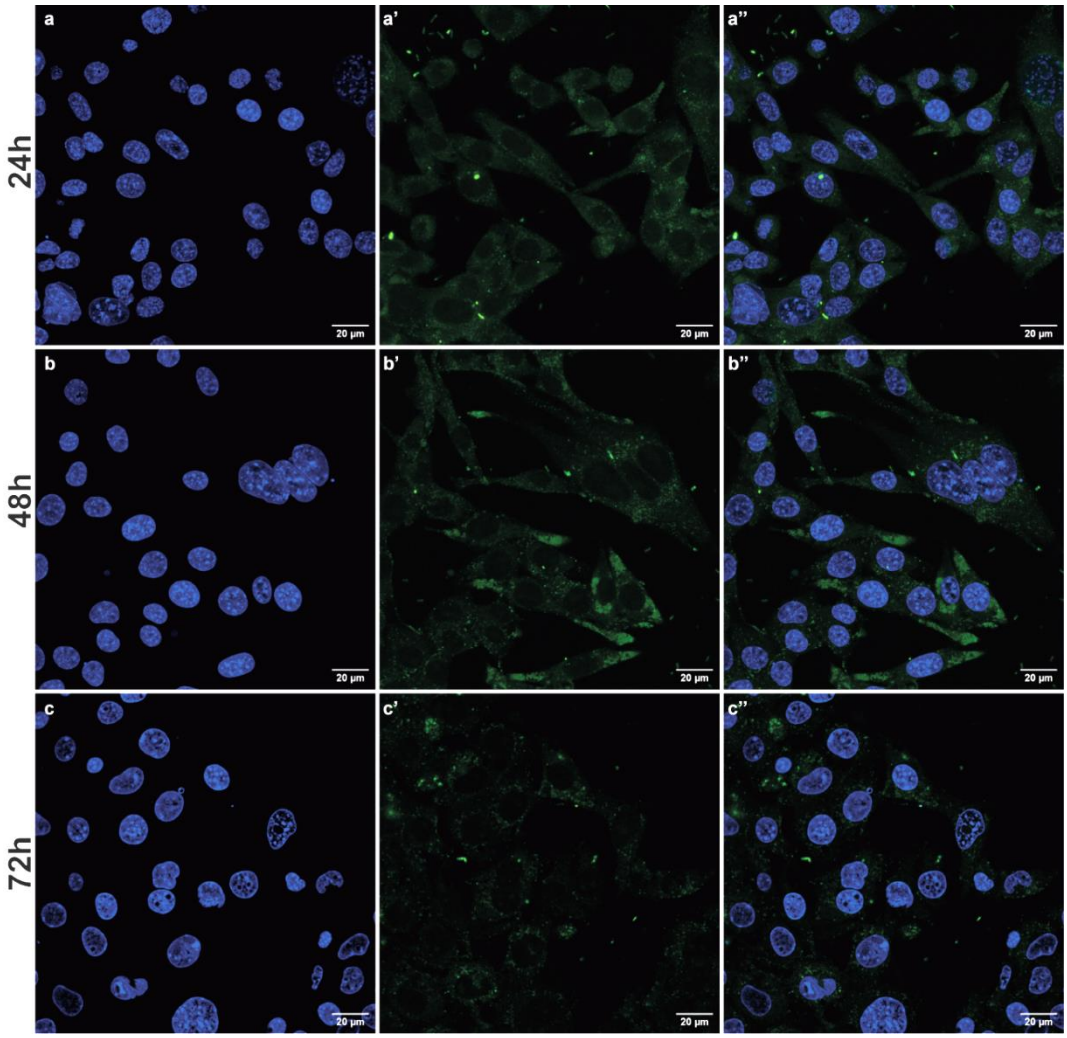

Figure 21. Cellular uptake kinetics of CDs-IND on the murine breast cancer cell line E0771 by confocal fluorescence microscopy. The analysis was performed after 24 h (**a-a'**), 48 h (**b-b'**), and 72 h (**c-c'**) of incubation with CDs-IND. Cells were fixed in PFA 4% and nuclei were stained with Hoechst 33342 dye. Micrographs were obtained by acquisitions in DAPI (a, b, c) and FITC (a', b', c') channels. The green signal is only attributable to CDs-IND self-fluorescence. (a'', b'', c'') Merge of DAPI and FITC channels.

The effect of CDs-IND treatment on cell viability after internalization was evaluated *in vitro* on the non-cancerous murine cell line NIH/3T3 and the murine mammary

cancer cell line E0771, and compared with the effect of CDs-PEG and free indoximod treatments (Figure 22 a). CDs-PEG demonstrated a dose-dependent cytotoxic effect with a significant selectivity towards breast cancer cells, with the half-maximal effective concentration (EC50) on NIH/3T3 calculated to be almost two-folds the EC50 on E0771 (1,138 vs 660 mg mL^{-1})(Figure 22 b). After the conjugation with indoximod, the cytocompatibility of the nanosystem increased, indeed at the higher concentration CDs-PEG displayed a significantly greater cytotoxicity, especially toward the E0771 cell line. This behavior is coherent with the already established inherent anticancer properties of our N/S-doped CDs, which have been associated with alterations in the ROS signaling pathway. On the contrary, free IND resulted totally cytocompatible at all the tested concentrations, with no differences between tumoral and non-tumoral cells. Since the drug payload does not exhibit any cytotoxic effect, the ability of CDs-IND to induce cancer cell death is only attributable to the inherent toxicity of CDs-PEG, highlighting the underrated potential of nanosystems as therapeutic tools, besides their application as drug delivery systems. Thus emerges the promise of cancer nanomedicine to reduce the reliance on highly cytotoxic chemotherapeutics or harmful radiation therapy.

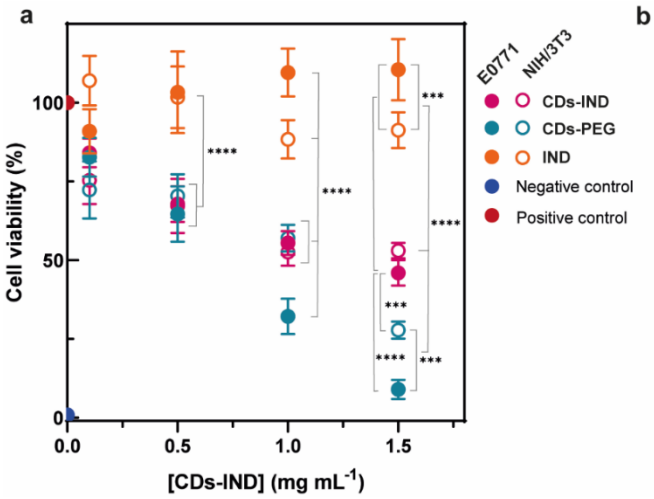

Sample	E0771 EC_{50} μg mL^{-1} [μM]	NIH/3T3 EC_{50} μg mL^{-1} [μM]
IND	> 11.5 [53.5]	> 11.5 [53.5]
CDs-PEG	660	1138
CDs-IND	1200 [42]	> 1500 [53.5]

Figure 22. *In vitro* evaluation of the cytotoxic effect of CDs-IND compared to CDs-PEG and free indoximod (IND). (a) Results of MTT cell viability assay for CDs-IND (pink), CDs-PEG (blue), and IND (orange) on the murine breast cancer cell line E0771 (full dots) and on the murine fibroblast cell line NIH/3T3 (empty dots), after 48 h of incubation. Data are reported as mean ± SD (N = 5-6). (b) Table reporting the half-maximal effective concentrations (EC_{50}) values calculated from interpolation (y = 50) of the fitting curves of the cytotoxicity studies.

3.2.3. *In vivo* CDs-IND controls tumor progression promoting immune activation

The CDs-IND conjugate was designed to control breast cancer progression by integrating the inherent anticancer properties of CDs with the indoximod-mediated immune system stimulation through IDO pathway inhibition. The expected synergistic anti-tumoral effect was evaluated *in vivo* in C57BL/6j mice bearing the E0771 syngeneic mammary adenocarcinoma model. Tumor-bearing mice were treated with free IND, CDs-PEG, or CDs-IND intratumorally (IT), following the treatment schedule reported in Figure 23 a. The treatments' tolerability was evaluated by

monitoring the body weight changes of the animals during the study, which resulted in positive increments with no evidence of mice sufferance (Figure 23 b). The average tumor volume of each treatment group was measured six times during the experiments, obtaining growth curves that clearly display an exponential increment of tumor masses in untreated controls and CDs-PEG or free IND treated mice, while the tumor burden was contained in the CDs-IND-treated group. On day 20 after tumor inoculation, the average tumor volume of untreated mice was 3.5-fold higher compared to mice treated with CDs-IND, whereas no significant differences were observed between controls and CDs-PEG or free IND treatment (Figure 23 c-c'). Such a difference is appreciable from the representative photographs of harvested tumors, reported in Figure 23 d. Thus, CDs-IND demonstrated an enhanced antitumoral activity that was not displayed either by the free drug or by plain CDs.

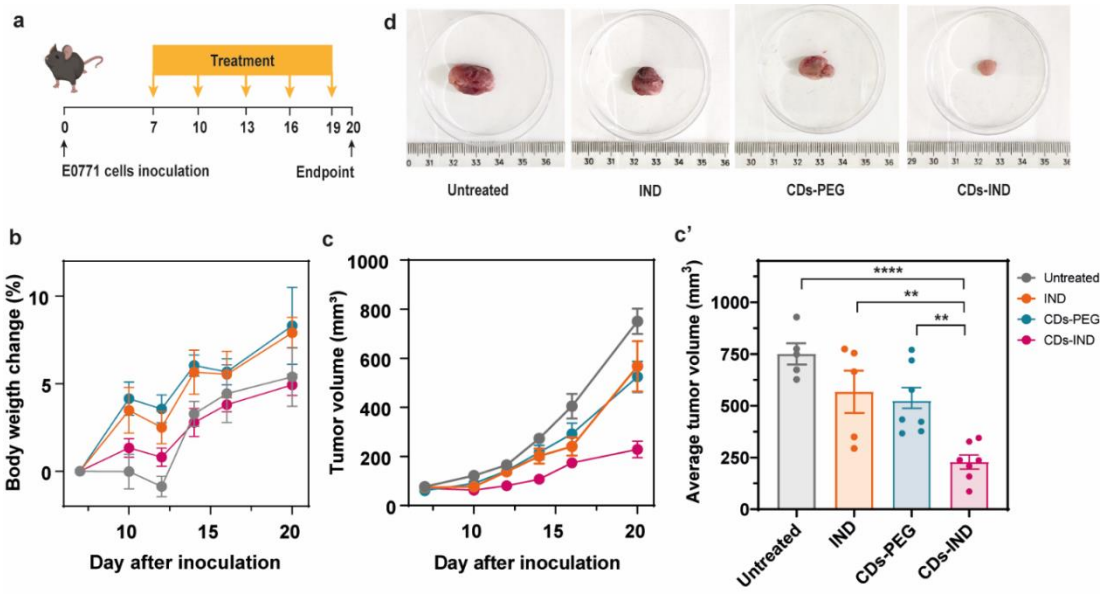

Figure 23. In vivo evaluation of CDs-IND antitumoral effect after intratumoral administration. (a) Timeline (days) indicating the treatment schedule, starting with the inoculation of E0771 cells, and concluding with the endpoint of the study. Mice

were treated with CDs-IND (1.12 mg mL^{-1}, 2.8 mg kg^{-1}) or equivalent concentrations of CDs-PEG or IND three days apart starting from day 7; untreated mice were used as control (N = 5-7 mice). All animals were euthanized on day 20, and tumors were harvested for further characterization. (b) Mice's average body weight changes from day 7, corresponding to the first day of treatment, reported as a percent difference ± SEM (N = 5-7). (c) Tracking of tumor volumes during the study and (c') average tumor volumes at the endpoint. Data refer to untreated (gray), IND (orange), CDs-PEG (blue), and CDs-IND (pink). (d) Representative photographs of harvested tumors from each treatment group.

To assess if the synergistic effect observed from the combination of CDs with indoximod involves a boosted antitumoral immune response, we characterized the immune profile of harvested tumors by fluorescence-activated cell sorting (FACS). The analysis was performed by adopting the gating strategy reported in Figure 24.

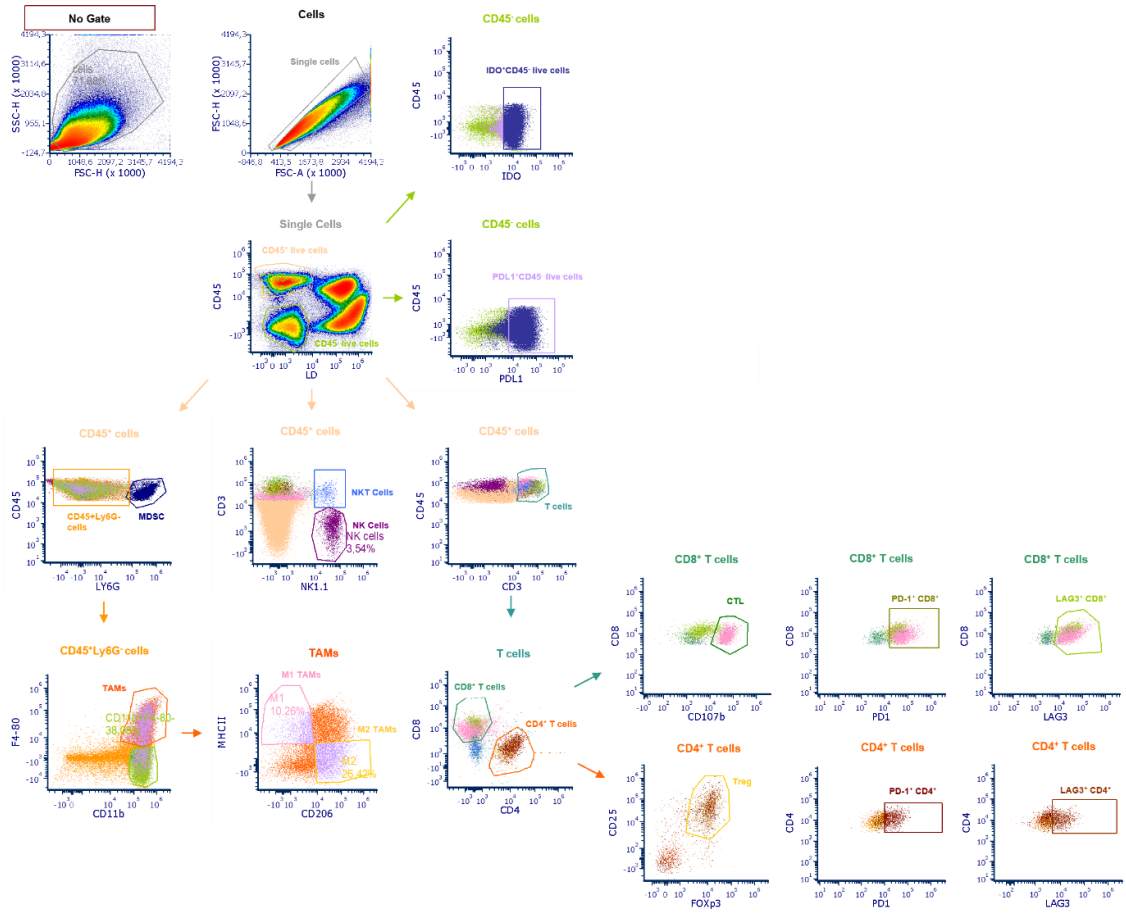

Figure 24. Gating strategy adopted for fluorescence-activated cell sorting (FACS) analysis. Representative plots obtained from the flow cytometry analysis of the TME gated for single cells, $CD45^+$ live cells, $CD45^-$ live cells, IDO^+CD45^- cells, $PD\text{-}L1^+CD45^-$ cells, T cells, $CD4^+$ T cells, $CD8^+$ T cells, cytotoxic T lymphocytes (CTL), regulatory T cells (Tregs), $PD\text{-}1^+CD4^+$ T cells, $PD\text{-}1^+CD8^+$ T cells, $LAG3^+CD4^+$ T cells, $LAG3^+CD8^+$ T cells, natural killer (NK) cells, NKT cells, myeloid-derived suppressor cells (MDSC), tumor-associated macrophages (TAMs), M1-TAMs, and M2-TAMs.

As shown in Figure 25, CDs-IND induced the greatest immune infiltration among all treatment groups. In particular, the TME of mice treated with the conjugate exhibited

greater infiltration of T cells, natural killer (NK) cells, natural killer T (NKT) cells, and tumor-associated macrophages (TAMs), compared with controls. Moreover, infiltrating TAMs presented prevalently the pro-inflammatory M1 phenotype, instead of an anti-inflammatory M2 phenotype, suggesting a favorable antitumoral immune response. However, the high levels of myeloid-derived suppressor cells (MDSC), significantly different from those in non-treated tumors indicate a feedback response that potentially hinders complete tumor remission CDs-IND.

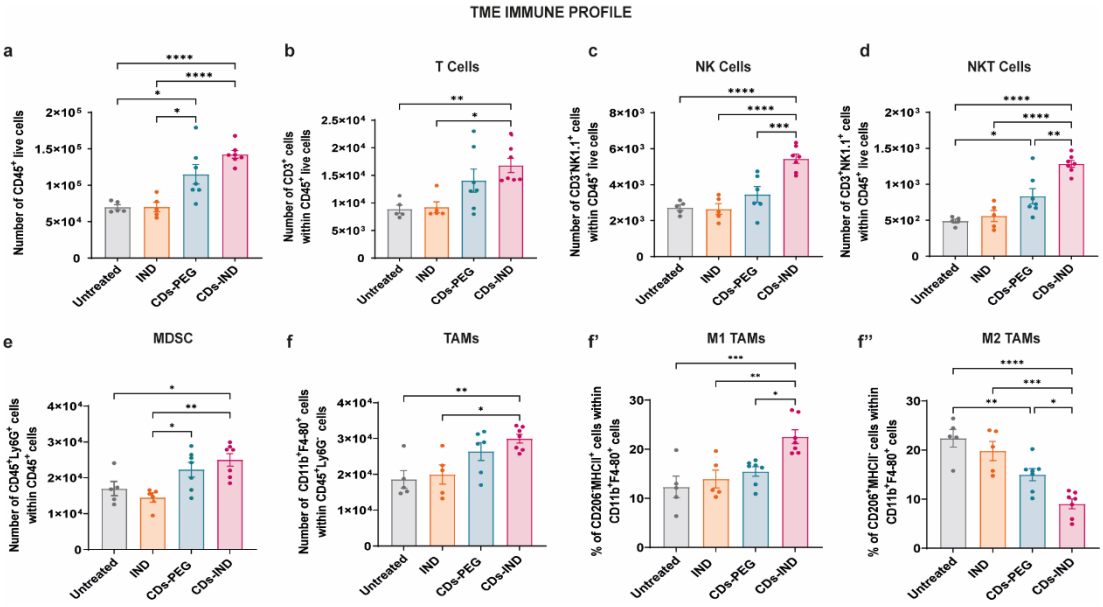

Figure 25. TME immune profile of harvested tumors evaluated by FACS. Cells' suspensions obtained from harvested tumors of untreated (gray), IND (orange), CDs-PEG (blue), and CDs-IND (pink) treatment groups were opportunely stained with labeled antibodies for performing FACS analysis. Graphs resume data obtained from FACS analysis, including determination of number of $CD45^+$ live cells (a), number of T cells (b), natural killer (NK) cells (c), number of NKT cells (d), number of myeloid-derived suppressor cells (MDSC) (e), number of tumor-associated macrophages

(TAMs) (f), percentage of M1 TAMs (f'), and percentage of M2 TAMs (f''). Data are presented as mean ± SEM (N = 5-7 mice).

Besides, the lower levels of T cells exhaustion markers, including LAG-3, IDO, PD-1, and PD-L1, demonstrate a reduced immune suppression in the TME after treatment with CDs-IND (Figure 26).

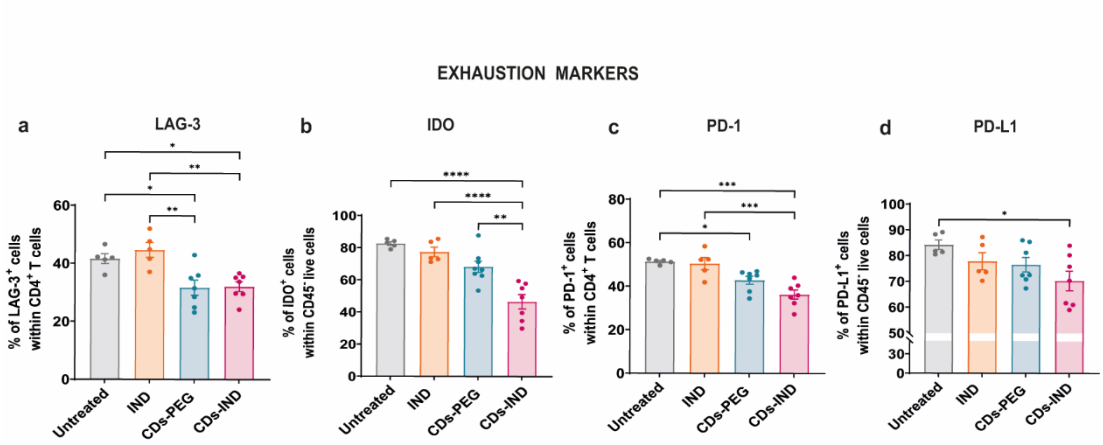

Figure 26. Exhaustion marker expression in the TME of harvested tumors. Cells' suspensions obtained from harvested tumors of untreated (gray), IND (orange), CDs-PEG (blue), and CDs-IND (pink) treatment groups were opportunely stained with labeled antibodies for performing FACS analysis. The percentage of exhaustion markers was evaluated as a parameter of TME immunosuppression. Graphs report the percentage expression of LAG-3 (a), IDO (b), PD-1 (c), and PD-L1 (d). Data are presented as mean ± SEM (N = 5-7 mice).

Altogether, the TME immune profile underscores the ability of CDs-IND to arm a robust immune response against breast cancer, although the indiscriminate increase of immune mediators in the TME precludes discerning between pathways directly stimulated by treatment and those ascribable to secondary feedback responses.

Interestingly, non-conjugated CDs-PEG also induced TME remodeling favoring the infiltration of immune mediators and reducing tumor immunosuppression, probably due to the local release of debris as a consequence of the inherent cytotoxic effect of CDs toward cancer cells. However, the immune response induced by unconjugated CDs-PEG and their intrinsic antitumoral properties were insufficient to limit tumor growth. Therefore, the different antitumor effect after conjugation with indoximod should be sought in the pathways where CD-PEG and CD-IND diverge. Comparing the immune profile of the two treatment groups actually reveals significant differences in terms of NK and NKT cell infiltration levels and IDO expression levels. The downregulation of IDO can be attributed to the presence of IND within the nanosystem, which is known as an inhibitor of the IDO downstream pathway. Nevertheless, IND-treated mice present a comparable TME immune profile to untreated controls, indicating that IND as a single agent is ineffective in promoting an antitumoral immune response or relieving TME immunosuppression. Although these data may seem inconsistent with *in vitro* evaluations of IND activity on T cell stimulation reported in the literature (Fox et al., 2018), they are actually coherent with the results of clinical trials reporting only a modest immunostimulatory effect for IND monotherapy (Soliman et al., 2016). Instead, more interesting results are reported by clinical trials combining IND with other therapies, which clearly prove IDO down-regulation within the TME, supporting our findings (Zakharia et al., 2021). Reducing IDO expression can increase the sensitivity of cancer cells to NK cells *in vitro* and promote NK infiltration in the tumor stroma of breast cancer. The role of innate immunity mediated by NK and NKT cells is emerging in cancer immunotherapy due to their role in managing tumor progression, with better prognosis correlated to high

levels of these cell types in tumor tissues (X. Liu et al., 2021; Rezaeifard et al., 2021; Roberti et al., 2012). The immunosuppressive effect of IDO may impair cytotoxicity and accumulation of NK cells, whereas IND treatment can restore NK-mediated anti-tumor functions by reactivating mTORC1 and thereby restoring cell metabolism (Della Chiesa et al., 2006; Frumento et al., 2002; Jing et al., 2024; Marçais et al., 2014). These considerations support our results, indicating that increased infiltration of NK and NKT cells along with downregulation of IDO play a critical role in determining the outcome of CDs-IND treatment.

3.2.4. The pharmacological outcome of CDs-IND does not depend on the administration route

Despite the encouraging results obtained with local injection of CDs-IND, the limited applicability of the IT route of administration poses considerable issues in terms of therapeutic translatability to clinics. Therefore, we evaluated the reproducibility of the CDs-IND antitumoral effect following systemic administration and compared the results to those of CDs-IND IT-treated mice and untreated control. In particular, CDs-IND, CDs-PEG, or free IND were administrated by injection in the mice's tail vein following the schedule previously described. The tumor volume monitoring, reported in Figure 27 a, shows that IV and IT treatment were similarly efficient in controlling tumor growth, resulting in a 4 fold lower average tumor volume compared to untreated control at day 20. The considerable volume difference between treated and untreated tumor masses, also appreciable from the photographs of harvested tumors, corroborates the anticancer activity of CDs-IND, regardless of the administration

route, suggesting that the nanosystem explicates the same effect after both IT and IV administration (Figure 27 b-c).

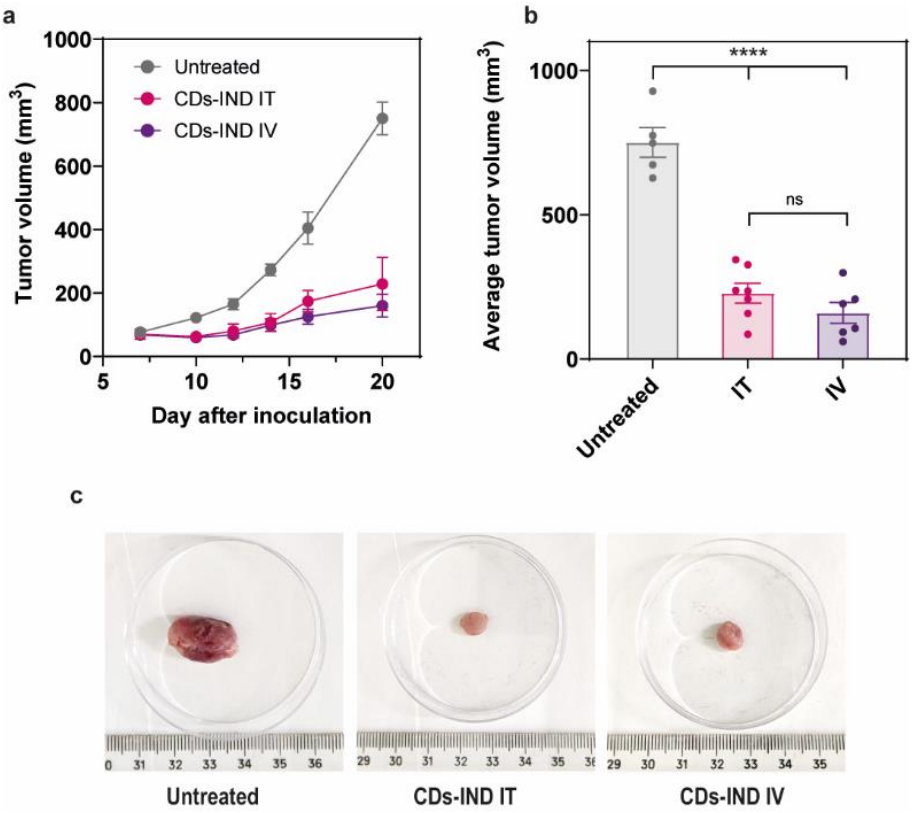

Figure 27. *In vivo* evaluation of CDs-IND anticancer effect after IT and IV administration. (a) Trand of tumor volume during the treatments and (b) average tumor volume at the endpoint for CDs-IND IT (pink), CDs-IND IV (purple), and untreated (gray) groups. (c) Representative photographs of harvested tumors from each group. Data are presented as mean ± SEM (N = 6-7 mice).

Notwithstanding the tumor burden control obtained following IV treatment, the TME of mice treated with CDs-IND systemically presented an immunosuppressive profile characterized by high infiltration of MDSC, M2-antiinflammatory TAMs, and elevated percentages of LAG-3 and PD-1 exhaustion markers on T-helper

lymphocytes. However, the presence of such immunosuppressive features did not affect the overall therapeutic outcome, suggesting that these immune cell types are not directly involved in the mechanism of action of CDs-IND. Instead, the TME of both IV and IT treatment groups presented comparable low levels of IDO expression and similar infiltration of NK and NKT cells. Thus, this experimental set corroborates our previous interpretation, highlighting the central role of IDO and NK/NKT pathways in the CDs-IND mediated antitumoral effect.

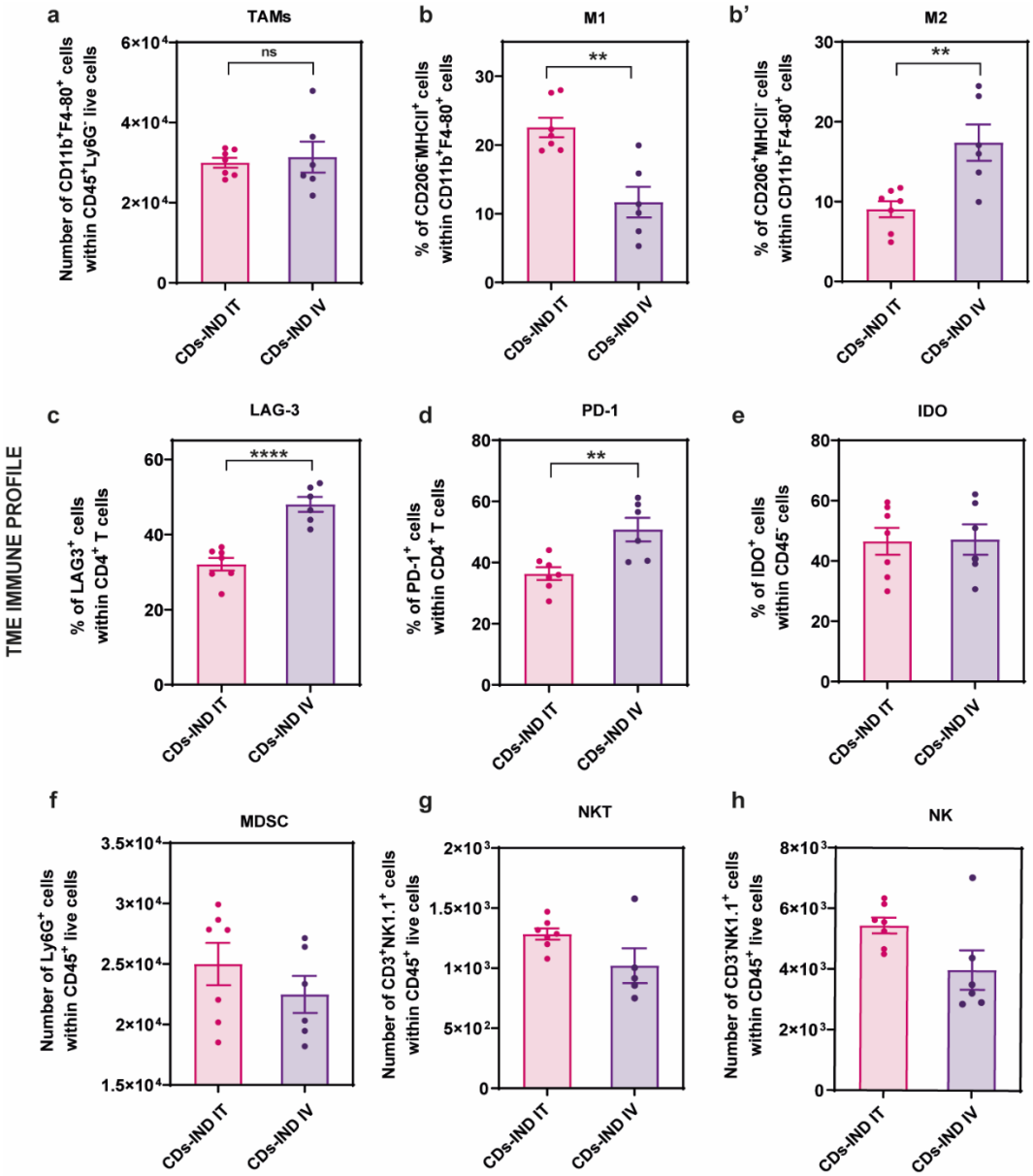

Figure 28. TME immune profile of harvested tumors determined by FACS, including number of myeloid-derived suppressor cells (MDSC), number of tumor-associated macrophages (TAMs), percentage of M1 TAMs, and percentage of M2 TAMs, quantification of exhaustion markers including LAG-3 and IDO, number of NKT cells, and number of natural killer (NK) cells. Data are presented as mean ± SEM (N=6-7 mice).

The effectiveness of CDs-IND treatment after IV administration validates the high potential of the nanotherapeutic tool developed, demonstrating that its promising anticancer efficacy is not limited to its local administration thus paving the way for real-life applicability through the more accessible systemic route.

3.3. Glucose-functionalized hybrid gold/carbon nanodots for multimodal breast cancer imaging exploiting the "Warburg effect"

3.3.1. Synthesis and characterization of ultrasmall hybrid gold/carbon nanodots functionalized with glucose as targeting moiety

Hybrid gold/carbon nanodots (AuCDs) were obtained by introducing gold seeds among the precursor of carbon nanodots during the synthesis of the carbonaceous nanostructures. This synthetic strategy aims to incorporate gold within the core of carbon nanodots during the formation of the crystalline nuclei, making a difference with the decoration of carbon nanodots with gold layers or nanoparticles that has been described in the literature. To prepare gold seeds we applied the first step of the seed-mediated synthesis of gold nanorods, consisting of the reduction of Au^{+3}, provided as $HAuCl_4$, using $NaBH_4$ as the reducing agent and CTAB as stabilizer (Figure 29) (Varvarà et al., 2020). The excess of CTAB was withdrawn by precipitation and centrifugation, taking advantage of its temperature-dependent solubility in water, thus preventing its potential toxicity (Sharma et al., 2019; Y. Zhang et al., 2015). The UV-Vis absorption spectrum of the gold seed suspension did not present the typical peak related to surface plasmon resonance phenomena, confirming that the gold nanoparticles in solution were smaller than 2 nm (Figure 30 a)(Watt et al., 2015). Subsequently, the light-red dispersion of gold seeds was treated with glutathione, exploiting the favored sulfur-gold interactions to replace the CTAB stabilizing the nanoparticles (Xue et al., 2014). The aqueous solution of glutathione-stabilized gold seeds was concentrated by rotary evaporation and mixed with a citric acid and urea solution in DMF. The mixture was kept reacting in a steel autoclave at 170°C for 4h.

The selected molecular precursors, citric acid and urea, have been extensively utilized as carbon and nitrogen donors during the solvothermal synthesis of CDs, due to their low cost, biocompatibility, and ease of availability. The reaction parameters employed have been accurately optimized to obtain highly fluorescent carbon nanocrystals presenting valuable hydrophilic functional groups at the surface.

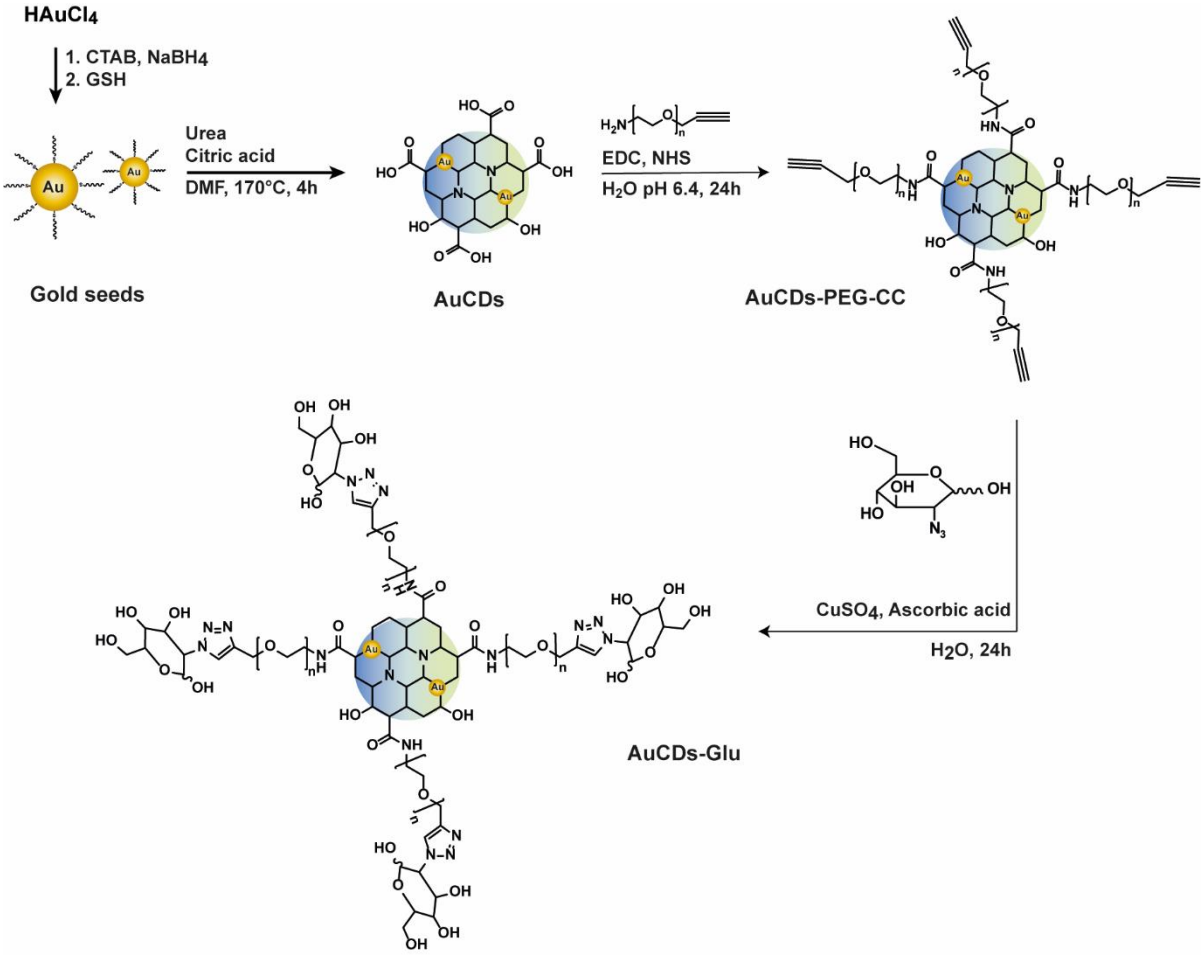

Figure 29. Synthesis pathway adopted for AuCDs-Glu. Gold seeds were prepared by reduction of Au^{III}, provided as $HAuCl_4$, using $NaBH_4$ as a reducing agent and CTAB as stabilizer, then GSH was used to replace CTAB at the surface of the seeds. The obtained gold seeds participated in the formation of carbonaceous structures via solvothermal decomposition of citric acid and urea, obtaining hybrid gold/carbon

nanoparticles (AuCDs). Subsequently, AuCDs were functionalized with amino-PEG-alkyne by amide coupling, providing the alkyne terminal groups needed for the subsequent click-chemistry reaction with 2-azido-2-deoxy-(D)-glucose.

After removing the organic solvent, the raw product was extensively purified by size exclusion chromatography, using a Sephadex® stationary phase packed with increasing cutoff (G10–G15–G25), to separate fractions with different size distribution, and thus different chemo-physical properties. The collected fractions were analyzed by UV-visible spectroscopy and spectrofluorimetry and gathered based on their optical properties in 4 groups, named A-D (Figure 30 b). Compared to the others, fraction D presented a more complex absorption spectrum extending to the red region, with main absorption peaks at 348 and 435 nm, and stronger multicolor fluorescence emission tunable by adjusting the excitation wavelength, with main peaks in the blue/green region (Figure 30 f). In contrast, fractions A-C were characterized by a less interesting absorption profile, consisting of a single main peak at 335–340 nm and a shoulder at 395–400 nm, and feeble fluorescence emission (Figure 30 c,d,e).

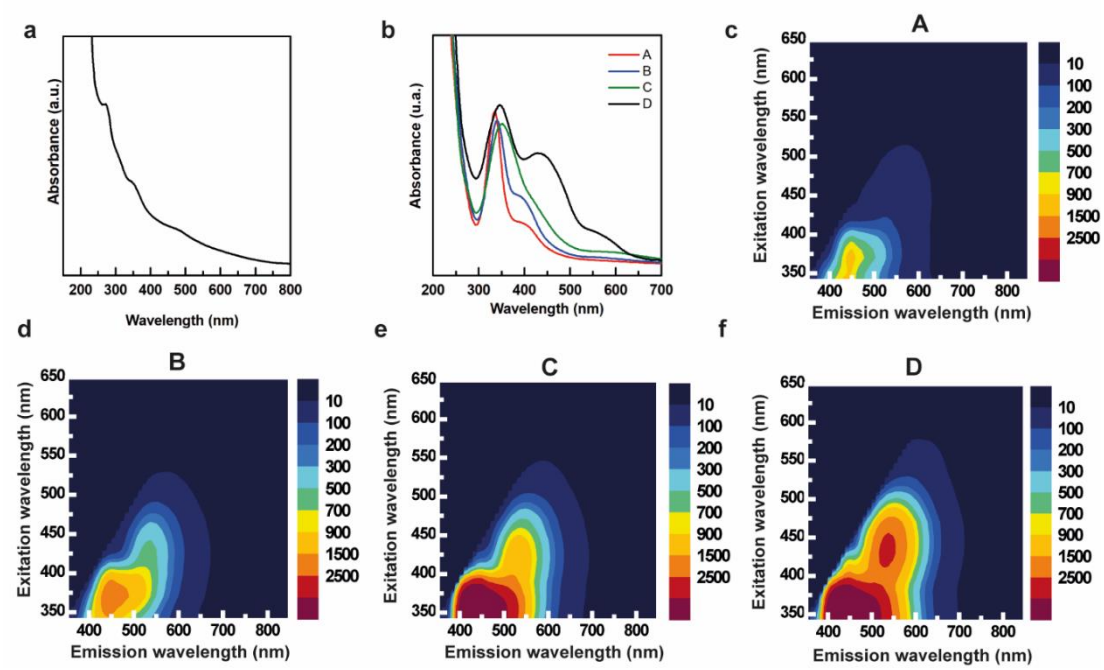

Figure 30. Optical characterization of AuCDs. UV-Vis absorption spectra of the gold seed suspension (a) and of the fractions collected from the purification process of AuCDs (b). 3D fluorescence emission spectra of fraction A (c), fraction B (d), fraction C (e), and fraction D (f) recorded in the 360 – 750 nm range (λ_{EX} 350 – 600 nm).

Therefore, only fraction D, hence referred to as AuCDs, was selected for the subsequent functionalization with 2-deoxy-(D)-glucose used as a targeting agent, with the aim of exploiting the Warburg effect to selectively direction the nanosystem to breast cancer cells. The conjugation was achieved by Cu(I)-catalyzed alkyne–azide Huisgen cycloaddition using 2-azido-2-deoxy-(D)-glucose and AuCDs modified to bring alkyne terminal functions (AuCDs-PEG-CC). In detail, a bi-functional poly(ethylene) glycol baring an alkyne terminal function (H_2N-PEG-CC) was obtained by coupling a poly(ethylene glycol) bis(amine) (2kDa) with 4-pentynoic acid, using EDC and NHS as activating agents. Then, the remaining free terminal amine of H_2N-

PEG-CC was conjugated to AuCDs through amide coupling leveraging on the high amount of carboxylic functional groups of the surface of AuCDs. Subsequently, the obtained AuCDs-PEG-CC was conjugated with 2-azido-2-deoxy-D-glucose in the presence of $CuSO_4$ and ascorbic acid, enabling the *in situ* reduction of Cu(II) to Cu(I), that serves as reaction catalyst (229).

The feasibility of the synthetic pathway adopted was confirmed by FT-IR analysis. In detail, the very peculiar peak at 1385 cm^{-1} in the spectrum of AuCDs can be attributed to the symmetric stretching of carboxylic groups interacting with the gold metallic surface, while the asymmetric stretching of carboxylic groups results shifted (1637 cm^{-1}) due to the proximity with the high electron density of the metallic surface (Figure 31 a). The spectrum of AuCDs also presents the intense I amide and II amide vibration bands at 1620 and 1495 cm^{-1}. After the functionalization with H_2N-PEG-CC, the reduced ratio of carboxylic to amidic vibrations indicates that an aliquot of the carboxylic groups of AuCDs has been involved in the amide coupling with PEG. Moreover, the spectrum of AuCDs-PEG-CC presents the typical vibrations of PEG chains, consisting of aliphatic C-H stretching at 2900 cm^{-1} and C-O-C stretching at 1100 cm^{-1}, confirming the presence of the polymer repeating units in the product (Figure 31 b). The spectrum of the conjugate AuCDs-Glu maintains the vibration bands of PEG just described, and shows a fingerprint region very similar to that of 2-azido-2-deoxy-(D)-glucose, characterized by C–O–C asymmetric stretching and C–C–O–H stretching (1475, 1370, and 1240 cm^{-1}). Instead, the neat peak of the azido group (2115 cm^{-1}) is absent in the spectrum of AuCDs-Glu, indicating that the azido group has been involved in the conjugation with 2-deoxy-(D)-glucose which successfully occurred. Moreover, the presumed formation of the triazole following the

Huisgen cycloaddition was confirmed by the intense C=N vibration band at 1642 cm^{-1} in the AuCDs-Glu spectrum (Figure 31 c-c').

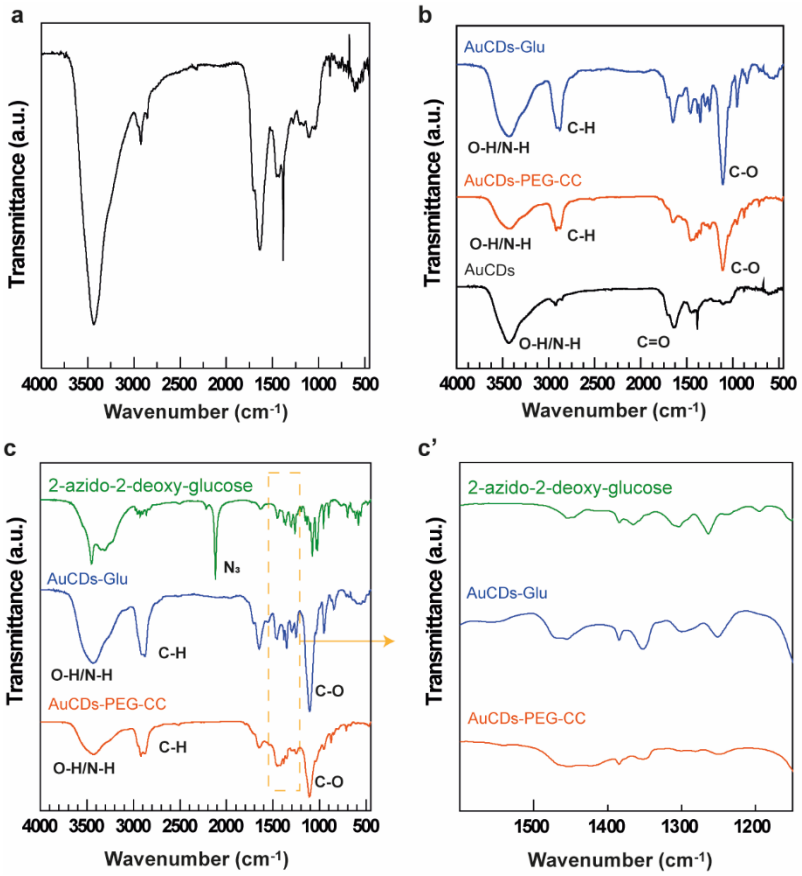

Figure 31. FT-IR spectra of AuCDs-Glu and precursors. FT-IR spectra of AuCDs (a), AuCDs-Glu (blue), AuCDs-PEG-CC (orange), and AuCDs (black) (b), (c); samples were prepared as KBr pellets and spectra were recorded in the 4000 – 400 cm^{-1} range. (c') Magnification of the FT-IR spectra of 2-azido-2-deoxy-glucose (green), AuCDs-Glu (blue), and AuCDs-PEG-CC (orange) in the 1600 – 1150 cm^{-1}.

The diameter and the size distribution of AuCDs and AuCDs-Glu were investigated by atomic force microscopy (AFM). Micrographs, reported in Figure 32, show that AuCDs appear as spherical objects with an average diameter of about 6 nm and a

narrow size distribution. The low heterogeneity of the sample validates the accurate purification performed to ensure low variability among the synthesized nanoparticles. After the conjugation with 2-deoxy-(D)-glucose, the average diameter of the nanosystem increased to almost 12 nm, almost doubling the size of bare AuCDs. Such dimensional increase is desirable to raise the size of the nanosystem above the renal cutoff of 5 nm, ensuring reduced renal clearance while maintaining an ultrasmall nanostructure ideal for favoring the penetration through the stiff tumor microenvironment (TME) and into the tumor parenchyma. The considerable diameter increment obtained is attributable to the presence of PEG chains at the surface of AuCDs-Glu, which is also functional in reducing the unspecific caption of the nanoparticles by reticuloendothelial system (RES) (Schipper et al., 2009), thus prolonging the blood circulation time of the nanoparticles and favoring their distribution to the tumor.

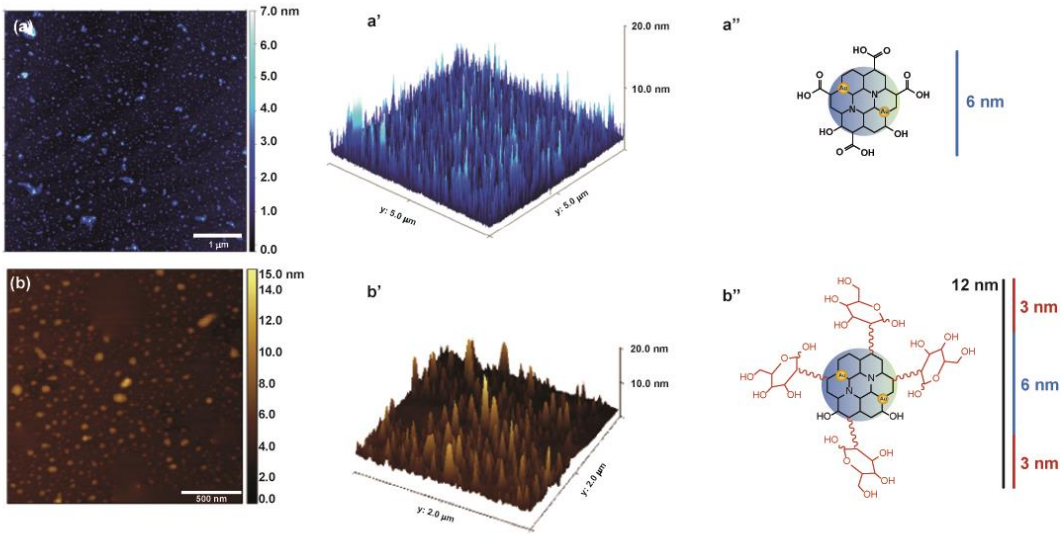

Figure 32. Atomic force microscopy characterization of AuCDs and AuCDs-Glu. AFM micrographs of AuCDs (a) (scalebar 1 μm) and AuCDs-Glu (b) (scalebar 500

nm); 3D reconstructions of AFM signals of AuCDs (a') and AuCDs-Glu (b'); schematic representation of nanoparticles size before (a'') and after (b'') functionalization of AuCDs.

The quantification of gold embedded within the structure of AuCDs was performed using the Spectroquant® Gold Test (Merck) kit, following the manufacturer's instructions. The kit uses a rhodamine B in sulfuric solution to form a red-violet complex with free Au^{+3}, enabling the qualitative detection of extracted ions and the spectrometric determination of Au^{+3} concentration in comparison with a calibration curve. To release and oxidate to Au^{+3} the gold ions entrapped in the crystalline core of AuCDs, the nanoparticles underwent a mineralization process consisting of high-temperature treatment in HNO_3 10% solution. Subsequently, the sample was tested using the Spectroquant® Gold Test allowing to establish that gold represents the 0.43% w/w of AuCDs.

3.3.2 The incorporation of gold confers CT contrast to AuCDs-Glu

The hybrid gold/carbon core of AuCDs-Glu was designed to confer computed tomography (CT) contrast to the nanosystem, enhancing its bioimaging application potential by providing deep-tissue imaging with high resolution. The CT contrast of AuCDs was evaluated by micro-CT analysis by acquiring micrographs of a nanosystem sample in aqueous solution (0.5 mg mL^{-1}) placed in a glass capillary. Compared to ultrapure water, used as a negative control, AuCDs displayed a remarkable X-ray scattering, confirming a strong CT contrast (Figure 33 a-a'). Next, the applicability of the CT contrast observed for imaging living tissue was established in an *in vivo* fungi model, consisting of tridimensional *P. Italicum* hyphae. The hyphal

living culture was incubated for 24 h with AuCDs-Glu (0.5 mg mL^{-1}), and analyzed by micro-CT. Micrographs, reported in Figure 33, demonstrate that while untreated hyphae cultures were not visible by micro-CT, treated hyphae showed a bright signal proving the cellular internalization of AuCDs-Glu and the efficacy of the nanosystem as CT contrast agents to image living cultures.

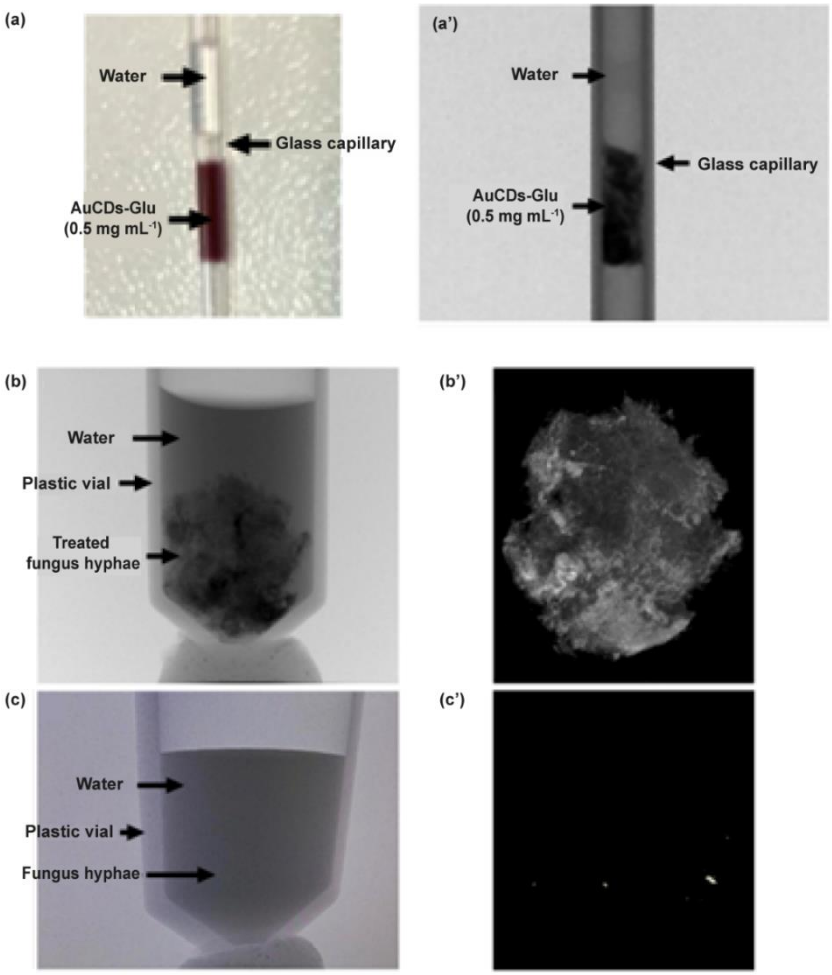

Figure 33. CT contrast characterization of AuCDs-Glu. (a) Samples of AuCDs-Glu and ultrapure water used as control within a glass capillary; (a') CT micrographs of AuCDs-Glu and water inside the capillary. Micro-CT measurements (b) and 3D reconstruction of the contrast signal (b') of *P. Italicum* fungi hyphae incubated for 24

h with a dispersion of AuCDs-PEG-Glu (0.5 mg mL^{-1}). Micro-CT measurements (c) and 3D reconstruction of the contrast signal (c') of *P. Italicum* fungi hyphae in water (negative control).

3.3.3. The self-fluorescence of AuCDs-Glu enables tracking its glucose-dependent cellular uptake

CDs are known for their photoluminescence suitable for applications in fluorescence imaging, whose high spatial resolution and sensibility are ideal for sub-cellular investigation, conferring self-tracking ability to the nanosystem for *in vitro* and *ex vivo* studies. The incorporation of gold within the structure of CDs and the functionalization with 2-deoxy-(D)-glucose should not impinge on their optical properties, conferring instead bi-functional imaging potential and active targeting properties. AuCDs, indeed, present a fascinating absorption spectrum characterized by multiple absorption peaks at 348, 440, and 560 nm, attributable to electronic transitions occurring at the surface due to the presence of various functional groups. The absorption spectra of AuCDs-PEG-CC and AuCDs-Glu maintain a very similar profile, with an intense absorption below 300 nm attributable to CDs' core state transitions, and a broad absorption extending all along the UV-visible region, although less defined than AuCDs' spectrum (Figure 34 a).

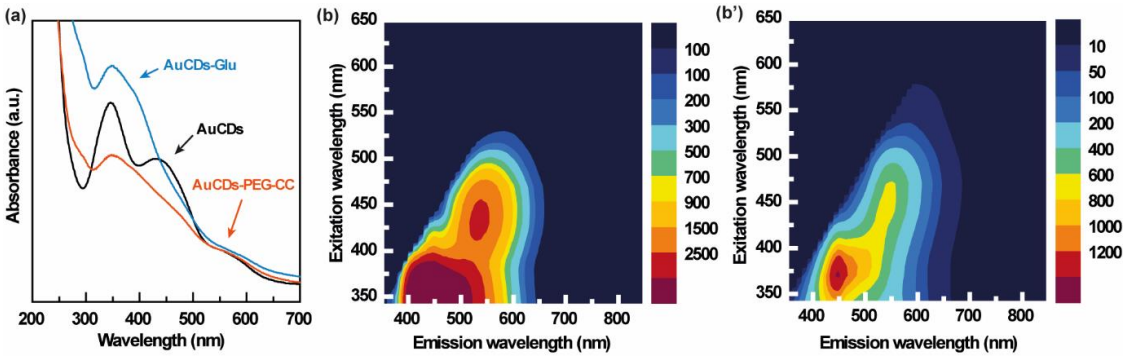

Figure 34. Optical properties of AuCDs-Glu and precursors. (a) UV-Vis absorption spectra of AuCDs (black), AuCDs-PEG-CC (orange), and AuCDs-Glu (blue). 3D emission spectra of AuCDs (b) and AuCDs-Glu (b') recorded in the 360 – 750 nm range (λ_{EX} 350 – 600 nm).

The optical absorption of AuCDs results in a multicolor emission spectrum, tunable based on the excitation wavelength, presenting a strong blue fluorescence with a maximum at 450 nm and a secondary peak in the green region (535 nm), obtained by exciting the sample at 360 and 440 nm respectively (Figure 34 b). After the conjugation with 2-deoxy-(D)-glucose, the nanosystem maintained the emission profile of AuCDs, presenting the same emission peaks at 450 nm and 535 nm. Furthermore, the emission spectra of AuCDs and AuCDs-Glu present a tail extending to the red region with decreasing intensity (Figure 34 c). Although the fluorescence emission of AuCDs-Glu is feeble in the window of biological transparency (Rao et al., 2007), the bright photoluminescence in the blue/green region is ideal for preliminary *in vitro* evaluation and *ex vivo* studies, conferring self-tracking ability to the nanosystem. The *in vivo* monitoring of the nanosystem is instead feasible by CT, due to the X-ray attenuation properties provided by the gold-doping of the carbonaceous

structure, which moreover provide high resolution with better contrast even in deep tissues.

The self-tracking properties of AuCDs-Glu were exploited to monitor their cellular uptake by both healthy (Human Schwann Cells, HSC - hTERT ipn02.3 2λ) and breast cancer cells (MCF-7) (Figure 35 a-d). In detail, cells were incubated with AuCDs-Glu for 24 h, then micrographs were obtained by widefield fluorescence microscopy in the blue/green channel. In a parallel experimental set, we evaluated the impact of glucose-mediated targeting on cellular internalization by performing the uptake study on cells pre-treated with a concentrated solution of glucose (250 mM), which should avoid glucose-mediated uptake. As shown in Figure 35, the maximum blue fluorescence intensity, corresponding to the higher accumulation of AuCDs-Glu, was observed in breast cancer cells not treated with D-glucose. On the contrary, MCF-7 cells with impaired glucose uptake displayed a slight fluorescence, indicating a lower internalization of AuCDs-Glu. These data suggest that the nanosystem mostly enters cancer cells through glucose-dependent mechanisms. Besides, the fluorescence intensity of healthy HSC cells due to AuCDs-Glu internalization is feeble compared to the bright signal observed in breast cancer cells, with negligible differences in the presence or absence of glucose pre-treatment, excluding a glucose-driven uptake (Figure 35 e). Thus, the use of glucose as a targeting agent effectively led to a preferential uptake by cancer cells, validating the targeting strategy adopted. It is noteworthy that the sefl-fluorescence of AuCDs-Glu enabled monitoring the cellular internalization of the nanosystem without labeling it with any fluorescent dye, demonstrating the proficiency of the obtained nanostructure as a fluorescence imaging probe for *in vitro* or *ex vivo* evaluations.

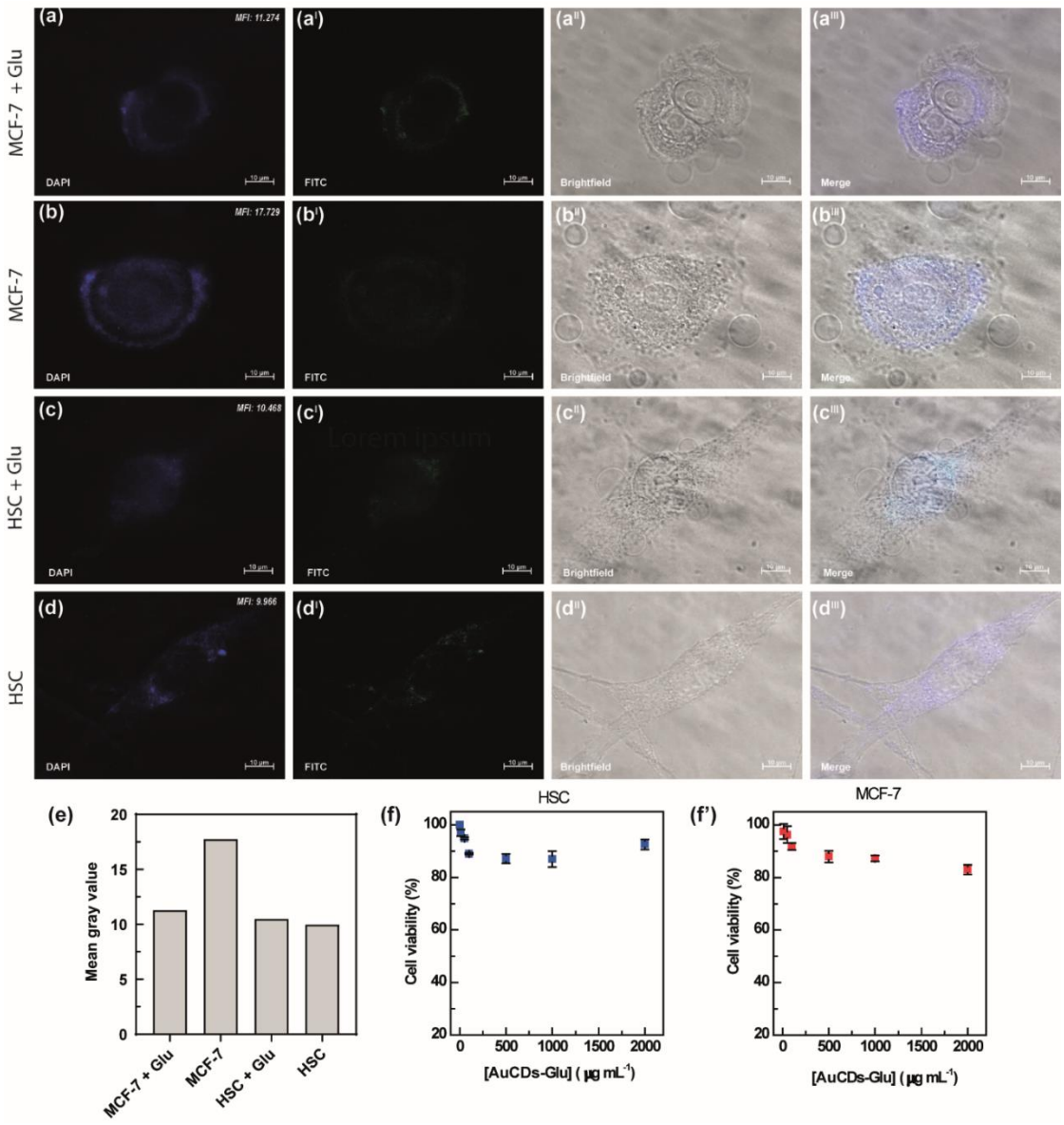

Figure 35. Biological properties of AuCDs-Glu. Fluorescence microscopy acquisitions after cellular uptake on breast cancer (MCF-7, a-b) and human Schwann cells (HSC, c-d), with (a-c) or without (b-d) pre-incubation with D-glucose; AuCDs-PEG-Glu are self-fluorescent in blue (DAPI channel) (a-d), and slightly in green (FITC channel) (a^{I}-d^{I}), brightfield micrographs (a^{II}-d^{II}), and all channels merged (a^{III}-d^{III}). 100X magnification. (e) Mean fluorescence intensity values calculated using the

ImageJ software. Cytocompatibility of AuCDs-Glu on HSC (f) and MCF-7 (f') evaluated by MTS assay. Data are reported as mean ± SD (N = 3).

The cytocompatibility of AuCDs-Glu was evaluated on HSC and MCF-7 cells by MTS assay (Figure 35 f-f'). In detail, cells were incubated with increasing concentrations of AuCDs-Glu for 48 h before performing the cell viability assay. Results, reported in Figure X, demonstrate the complete biocompatibility of the nanosystem, which induces only negligible reduction of cell viability at all the tested concentrations. Indeed, even at the highest concentration of 1.0 mg mL^{-1}, the nanosystem caused less than 15 % reduction of cell viability of both MCF-7 and HSC cells, which presented 87.0 ± 3.0 % and 87.1 ± 1.1 % cell viability respectively. The insignificant cytotoxic effect induced by AuCDs-Glu on both tested cell lines underscores the higher biocompatibility of carbon nanodots compared to other fluorophores, encouraging their potential use for biomedical applications.

3.4. Gadolinium-doped carbon nanodots for bi-modal imaging guided theranostic applications in breast cancer

3.4.1. Gadolinium ions entrapped within the core of carbon nanodots provide unique crystalline structures

The rationale adopted to incorporate gadolinium-(III) ions within the structure of CDs relies on introducing $GdCl_3$ among the molecular precursors of CDs during their synthesis in solvothermal conditions (Figure 36). The solvothermal synthesis of CDs is a validated approach to obtain carbon nanodots (CDs) presenting fascinating optical properties, tailorable by adjusting the reaction parameters. In this process, the chemical composition of the obtained nanoparticles derives from the structure of the small molecules employed during the decomposition process. Urea and citric acid are commonly used for the synthesis of N-doped photoluminescent carbon nanodots presenting hydrophilic groups at the surface, including amidic, hydroxylic, and carboxylic functions. Performing the synthesis in presence of Gd^{+3} ions, provided as $GdCl_3$, should favor the incorporation of gadolinium ions within the carbonaceous structure of CDs, leading to hybrid nanoparticles endowed with both optical and paramagnetic properties, valuable for FLI/MRI bi-modal imaging. Considering the ability of citric acid to interact with Gd^{+3} ions forming 2:1 complexes, we selected a 1:10 molar ratio of gadolinium ions to citric acid, thus to obtain in solution both free citric acid molecules, playing a major role in the formation of the crystalline core of carbon nanodots, and citric acid/Gd^{+3} complexes involved in the core doping with Gd^{+3} ions.

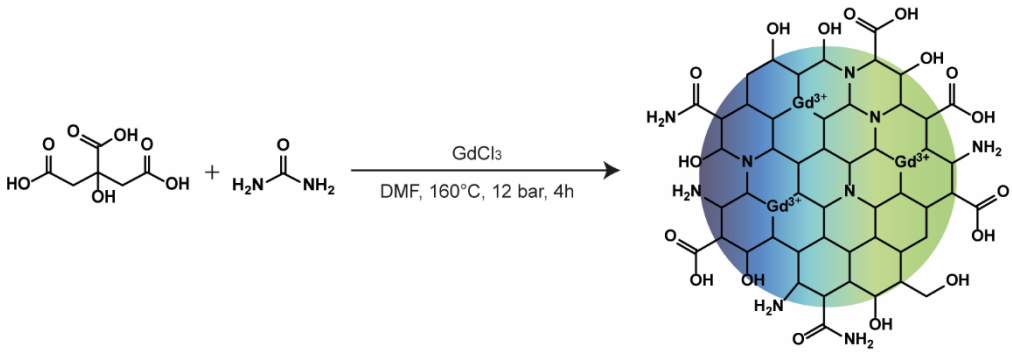

Figure 36. Synthetic pathway of GdCDs.

The pressure recorded during the solvothermal decomposition process reached 12 bar, a condition that usually leads to green-emitting CDs of 1-5 nm presenting a crystalline structure. The raw product was purified by size exclusion chromatography, using a Sephadex® G-10/G-15/G-25 stationary phase to separate fractions with different size distributions. The collected fractions were gathered in three main groups, named R_1 – R_3, based on their UV-Vis absorption spectra (Figure 37). Among them, R_3 displayed the most interesting spectrum with a main absorption in multiple absorption peaks at 350, 460, and 570 nm, indicating a complex surface chemistry characterized by different functions involved in electronic transitions. On the contrary, R_1 and R_2 presented less defined spectra with main absorption in the blue region and low definition, probably due to the inhomogeneity of the samples (Figure 37 a).

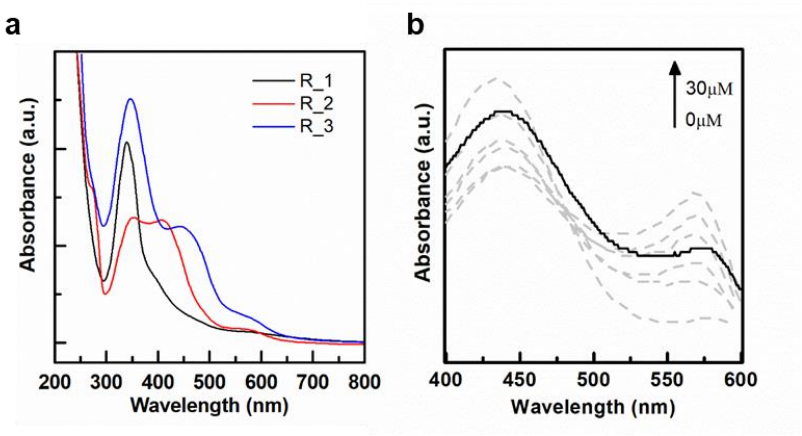

Figure 37. UV-Visible absorption spectra of collected fractions from the purification of GdCDs (a) and UV-Visible absorption of GdCDs complexed with Gd^{+3} (black) compared with the spectra of the gadolinium chloride standard solutions employed to build the calibration curve (b).

Therefore, only fraction R_3 was selected for further purification by size exclusion chromatography in acidic conditions (pH 1.0), performed to remove Gd^{+3} ions eventually complexed at the surface of CDs by protonating all the carboxylic groups. The presence of gadolinium interacting mildly with the surface of CDs is, indeed, undesirable as it could easily result in unintended Gd^{+3} release by simple diffusion causing possible side effects due to the toxicity of the doping agent and compromising the integrity of the nanosystem under physiological conditions.

The quantification of Gd^{+3} integrated into the structure of the gadolinium-doped carbon nanodots (GdCDs) was performed spectroscopically, using xylenol orange tetrasodium salt (XO) as a metal indicator. Briefly, XO is an organic dye presenting two characteristic absorption peaks at 433 and 573 nm. In solution, XO forms a complex with metal cations, such as Gd^{+3}, which causes a change in the relative

intensity of the two absorption bands, detectable by UV-vis spectroscopy. GdCDs were firstly mineralized by dissolution in HNO_3 (10%) and high temperatures treatment, to degrade the carbonaceous structure thus releasing Gd^{+3} ions eventually entrapped in the core of GdCDs. The sample was then treated with XO, and its absorbance at 573 nm and 433 nm were measured (Figure 37 b). The ratio of the two values was compared to that obtained from the UV analysis of $GdCl_3$ standard solutions, thus calculating that 0.34 % w/w of GdCDs consists of Gd^{+3} ions.

The chemical characterization of GdCDs was performed by combining different analysis techniques, such as FT-IR, ^{1}H-NMR, and XPS analysis. The FT-IR spectrum of GdCDs displays the diagnostic bands of carboxyl (1715 cm^{-1}) and amide I (1665 cm^{-1}) asymmetric stretching, together with the O-H and N-H stretching (3400-3200 cm^{-1}), C-N stretching (1385 cm^{-1}) and N-C-O (1200 cm^{-1}) (Figure 38 a). The presence of several polar functional groups at the surface of GdCDs was corroborated by analyzing the ^{1}H-NMR spectrum of GdCDs, which displays distinguishing resonances of carboxyl (10.0 – 10.2 ppm), amide (5.69 – 7.92 ppm), and hydroxyl (3.84 ppm) groups (Figure 38 b). Altogether, FT-IR and ^{1}H-NMR data indicate that the surface of GdCDs is characterized by several polar functional groups, such as amine, hydroxyl, and carboxyl, which confer high dispersibility in different solvents and are valuable for coupling reactions to obtain surface functionalization. XPS analysis further confirms the presence of the described functional groups at the surface of GdCDs, besides providing indications of Gd^{+3} doping. In detail, the O 1s signal, reported in Figure 38 c, displays typical peaks of hydroxyl and carbonyl groups, with the latter as the principal contributor (25.36%). Since the N 1s signal (~ 400 eV) is characterized by a single peak mainly due to amine groups, the contribution of amide to the O 1s

signal can be considered negligible, indicating a major presence of carboxylic groups (Figure 38 c'). Coherently, the C 1s signal shows the characteristic contributions of C−C/C−H (~285.5 eV), C−O/C−N (~287 eV), and O=C (~288.5 eV) (Figure 38 c''). The presence of Gd^{+3} ions was investigated in the 140 – 160 eV range, corresponding to the Gd 4d signal. In this region, the binding energy of Gd signals can be correlated with the oxidation state of the detected ion. In our analysis, the signal detected at 154 eV suggests that gadolinium is present as paramagnetic Gd^{+3} ions in the sample, as desirable for MRI purposes. However, the low intensity of the signal indicates that Gd^{+3} ions are present only in small amounts at the surface of GdCDs (Figure 38 c'''').

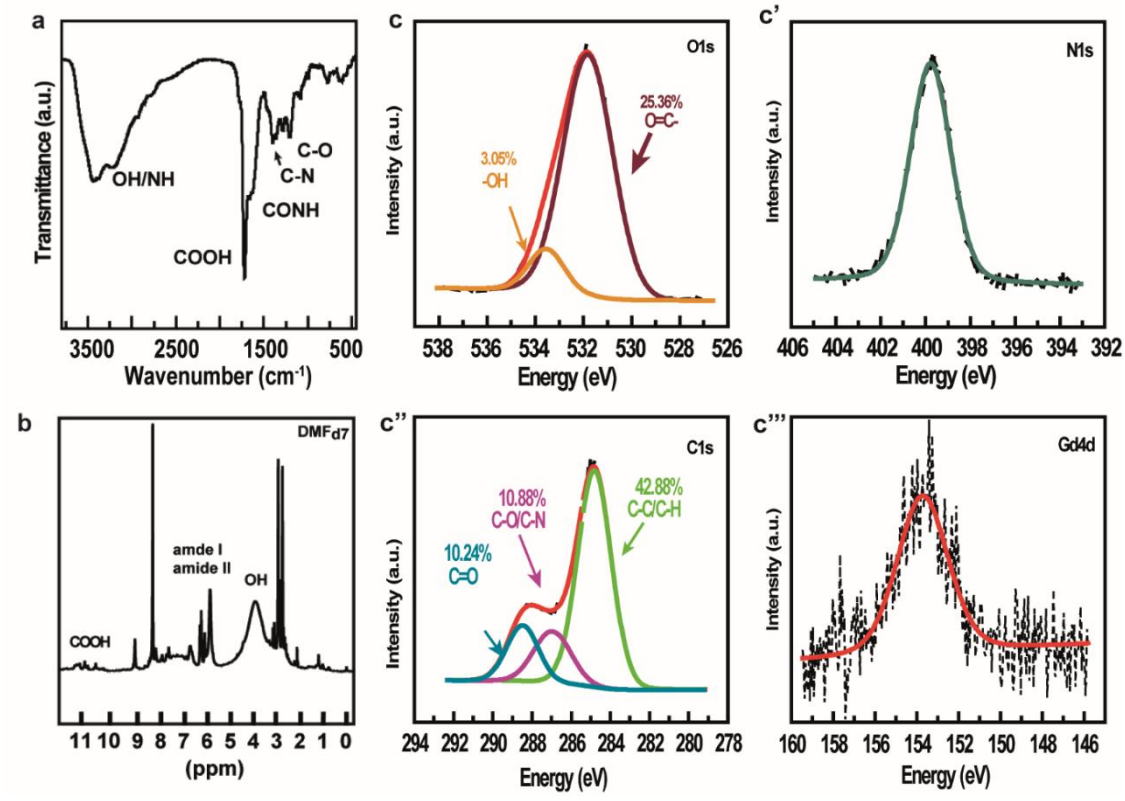

Figure 38. Chemical characterization of GdCDs. (a) FT-IR spectrum of CDs-Gd prepared as a KBr pellet and recorded in the 4000 – 400 cm^{-1} range. (b) ^{1}H NMR

spectrum of CDs-Gd solution in DMF-*d7* reorded operating at 400.12 MHz. (c−c’’’) XPS analysis and deconvolutions of the rough spectra.

Although XPS data show a negligible amount of gadolinium on the nanosystem surface, gadolinium quantification by colorimetric assay proved the presence of a higher concentration of Gd^{+3} in GdCDs. Therefore, assuming that Gd^{+3} ions were enclosed within the core GdCDs we investigated its structure by high-resolution transmission electron microscopy (HR-TEM). HR-TEM micrographs showed homogeneous nanocrystals of about 5 nm diameter with a peculiar *d*-spacing pattern in which the lattice planes appear deflected, although maintaining a regular structure, as indicated by the constant d-spacing value of 0.244 ± 0.013 nm. (Figure 39 a-a’). Such deflection can be attributed to structural defects of the crystalline core coherent with the entrapment of Gd^{+3} ions within the core of GdCDs. The unconventional crystalline structure observed is a unique feature of our hybrid nanoparticles, marking a difference from other gadolinium-containing carbon nanodots reported in the literature, which usually have amorphous or regular crystalline cores with aligned lattice planes. Moreover, the incorporation of Gd^{+3} is commonly obtained by coordination to carboxyl functions at the surface of CDs, rather than incorporation in the carbonaceous core. Entrapping Gd^{+3} within the nanocrystal instead of chelating it at the surface is particularly advantageous as it favors retaining the ions inside the nanostructure, thus preventing their uncontrollable release throughout the body after administration, which could cause undesired toxic effects.

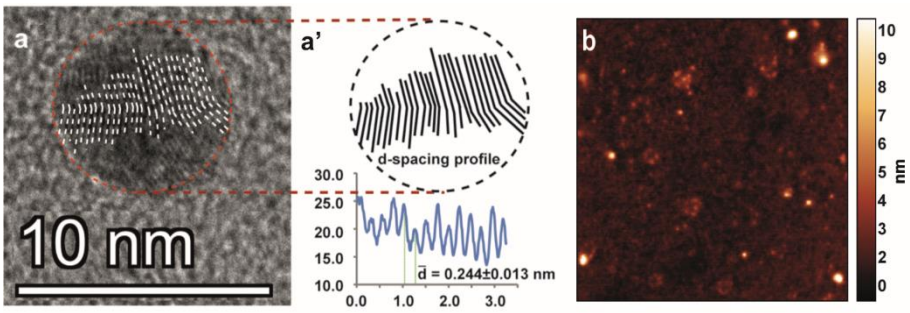

Figure 39. Structural characterization of GdCDs. HR-TEM micrograph (a) and details of the *d*-spacing profile (a') of GdCDs. AFM micrograph of GdCDs (b).

The size distribution of GdCDs was assessed by atomic force microscopy (AFM). The micrograph, reported in Figure 39 b, shows objects with spherical shape and 5.10 ± 0.20 nm average heights, corroborating HR-TEM data. Only a few aggregates are visible in the sample, which appears overall homogeneous, demonstrating the effectiveness of the purification process adopted.

3.4.2. CDs-Gd display pH-dependent MRI contrast and photoluminescence suitable for bioimaging purposes

The MRI contrast of GdCDs was investigated to evaluate if the incorporation of gadolinium ions effectively confers paramagnetic properties to the nanosystem. T_1-weighted magnetic resonance images were acquired using a 1.5T clinical MRI scanner. Acquisitions were performed at increasing concentrations of Gd^{+3} and different pH values, selected to mimic the pH conditions of the bloodstream (7.4), the tumor microenvironment (6.4), and the cancer endosomes (5.5) (Figure 40 a). The MRI signal recorded, shown in Figure 40 b, confirms that all the samples displayed a paramagnetic behavior resulting in an MRI signal enhancement. The MRI signal plot against inversion time (T_1) was used to calculate the relaxation time (T1) and the

relaxation rate ($R_1 = 1/T_1$), which was also reported plotted as a function of pH (Figure 40 b') and Gd^{+3} concentration (Figure 40 b''). Results highlighted a reduction of R_1 as the pH value increases, which is remarkable passing from pH 5.5 to 6.4, reaching the maximum 20% reduction at the higher concentration tested (10.8 μM), and less evident between pH 6.4 and 7.4. The observed pH-related changes in R_1 are attributed to the different H^+ concentrations which directly influence the longitudinal relaxation by altering proton exchange phenomena and cause the protonation of carboxyl groups at the surface of the GdCDs, changing the hydration state of the contrast agents thus modifying their exchange rate with water and therefore altering the MR contrast. As expected, the relaxation time (T_1) decreased as the sample concentration increased, as a consequence of the higher amount of paramagnetic spices in the solution. This relationship is described by the following formula:

$$R_{1\,obs} = R_{1\,int} + \rho_1[Gd^{+3}]$$

Where $R_{1\,obs}$ is the observed relaxation rate, $R_{1\,int}$ is the relaxation rate in the absence of the paramagnetic species, and ρ_1 is the longitudinal relaxivity. The relaxivity of the samples was calculated by linear fitting of R_1 plotted against Gd^{+3} concentration, and compared with the relaxivity of Gadobutrol, a commonly used MRI contrast agent. As reported in Table 3, the ρ_1 of all samples exceeded that of clinical standard, proving the efficacy of GdCDs as MRI contrast agents. Moreover, the ρ_1 at pH 5.5 (11.3 ± 0.2 $\mu M^{-1}\,s^{-1}$) results almost two times higher than $\rho_1$at pH 6.4 and 7.4 (6.1 ± 0.7 $\mu M^{-1}\,s^{-1}$ and 5.0 ± 1.1 $\mu M^{-1}\,s^{-1}$, respectively), indicating a remarkable sensitivity of GdCDs mediated MRI contrast at lower pH values. The influence of pH on MRI properties can be exploited to monitor the pH changes in the TME, obtaining real-time

information about the therapeutic outcome. The pH of the TME is usually lower than the physiological value, but it passes from acidic (pH 5.5 – 6.4) to physiological conditions during cancer regression, thus pH monitoring can be exploited for real-time evaluation of therapeutic efficacy, allowing adjustments of the treatment based on the patient individual response. Therefore, theranostic nanosystems endowed with pH-sensing imaging properties are promising to implement non-invasive personalized therapeutic approaches, going beyond the use of MRI for patients' stratification.

The optical properties of GdCDs are also influenced by the pH of the surrounding environment. GdCDs are characterized by a wide absorption spectrum extending in all the UV/visible regions, with three main absorption peaks at 350, 450, and 575 nm (Figure 40 c) corresponding to electronic transitions occurring at the nanoparticle's surface due to its complex chemistry. The wavelength of the absorption peaks does not shift by changing the solution pH, indicating that absorption phenomena are not sensitive to pH alterations. The broad absorption spectrum corresponds to a multicolor fluorescence emission, tunable by adjusting the excitation wavelength. In particular, GdCDs display a strong emission in the blue/green region, with a decreasing tail that extends to red wavelengths. Their marked photoluminescence is a fascinating feature of GdCDs, useful to perform cell labeling and intracellular tracking by FLI. Unlike the absorption spectrum, the main emission peak of GdCDs seems to be influenced by the pH, as indicated by the stronger emission of the blue peak detected at acidic pH values (Figure 40 d-d''). The fluorescence-mediated pH-sensing offers additional opportunities for cancer intracellular monitoring exploiting the high spatial resolution of fluorescence microscopy.

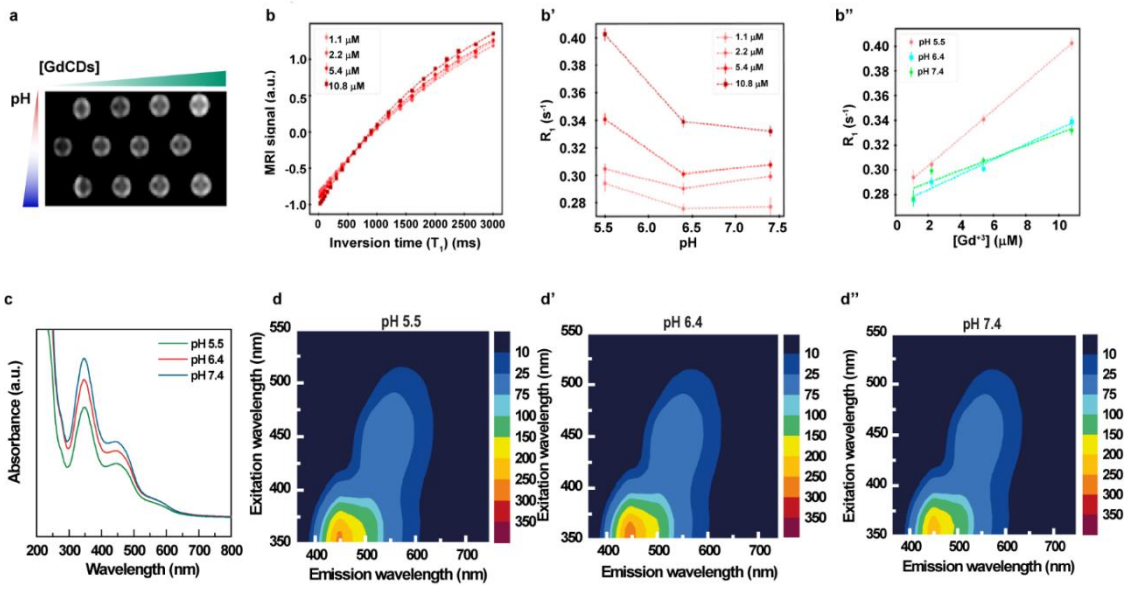

Figure 40. Bioimaging properties of GdCDs. (a) T1-weighted MR acquisition on samples of GdCDs at increasing concentrations (1.1 - 10.8 μM) and different pH values (5.5, 6.4, and 7.4) (TR = 4000 ms, TI = 3000 ms). (b) MRI signal as a function of the inversion time (TI); typical saturation trends are observed, with the magnetization recovery being faster for higher Gd^{+3} contents. (c) Longitudinal relaxation rate R_1 as a function of the pH for various Gd^{+3} concentrations. (d) Longitudinal relaxation rate R_1 as a function of the Gd^{+3} concentration for various pH values. (c) UV/Visible absorption spectra of GdCDs at pH 5.5 (green), 6.4 (red), and 7.4 blue, recorded in the 800 – 200 nm range. (d-d'') 3D emission spectra of GdCDs at different pH values (5.5, 6.4, and 7.4) recorded in the 360 – 740 nm range (λ_{EX} = 350 – 550 nm).

Sample	Relaxivity ($\mu m^{-1} s^{-1}$)
GdCDs pH 5.5	11.3 ± 0.2
GdCDs pH 6.4	6.1 ± 0.7
GdCDs pH 7.4	5.0 ± 1.1
Gadobutrol	3.3 ± 0.2

Table 3. Relaxivity values calculated based on the MRI analysis.

Furthermore, the absorption and emission spectra of GdCDs aqueous solutions are not altered over time (Figure 41 a-b), validating their stability as optical imaging probes. Compared to conventional fluorescent probes consisting of small molecule organic dyes, GdCDs are not subjected to photobleaching phenomena, as the fluorescence emission decadence observed after 300 s of continuative irradiation rapidly recovers reaching again the fundamental state after 600 s in the dark (Figure 41 c).

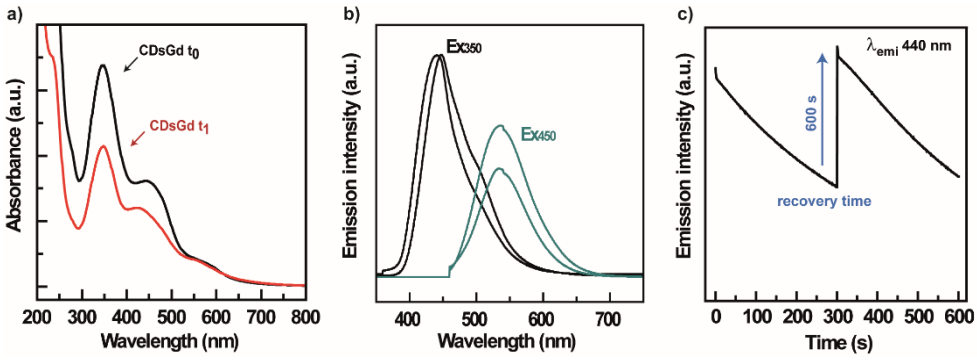

Figure 41. Stability of GdCDs optical properties. Absorption (a) and emission (b) spectra of a fresh CDs-Gd dispersion in ultrapure water (0.1 mg mL^{-1}) compared with a dispersion stored for four months at room temperature. (c) Emission registered for a dispersion of CDs-Gd in ultrapure water (0.1 mg mL^{-1}) up to 5 minutes of continuous excitation at 350 nm (λem = 440 nm), repeating the experiment two times with a recovery time (storage in the dark) of 10 minutes.

The self-tracking properties of GdCDs have been exploited to evaluate their cellular uptake *in vitro* by breast cancer (MCF-7) and epithelial (16-HBE) cell lines, using widefield fluorescence microscopy.

In detail, cells were treated with GdCDs in DMEM (0.15 mg mL^{-1}) for 2, 6, and 24 h, then cells' nuclei were stained with DAPI before acquiring fluorescence microscopy micrographs. As shown in Figure 42, the green bright photoluminescence of GdCDs (FITC channel) enabled tracking the cellular internalization of the nanosystem, that efficiently occurs in both the tested cell lines, also obtaining details about intracellular trafficking. Indeed, the DAPI signal colocalizes with the GdCDs' green fluorescence, indicating that the nanosystem also enters cell nuclei, probably by simple passive accumulation due to the ultrasmall diameter of our nanosystem. The intracellular distribution of GdCDs is similar in MCF-7 and 16-HBE cells up to 6h, instead after 24 h incubation it is possible to notice a significant accumulation of the nanosystem within vesicular structures, especially in 16-HBE cells. This evidence suggests that the elimination of GdCDs through exocytosis processes occurs earlier in 16-HBE cells, whereas cancer cells display a prolonged retention of the nanosystem.

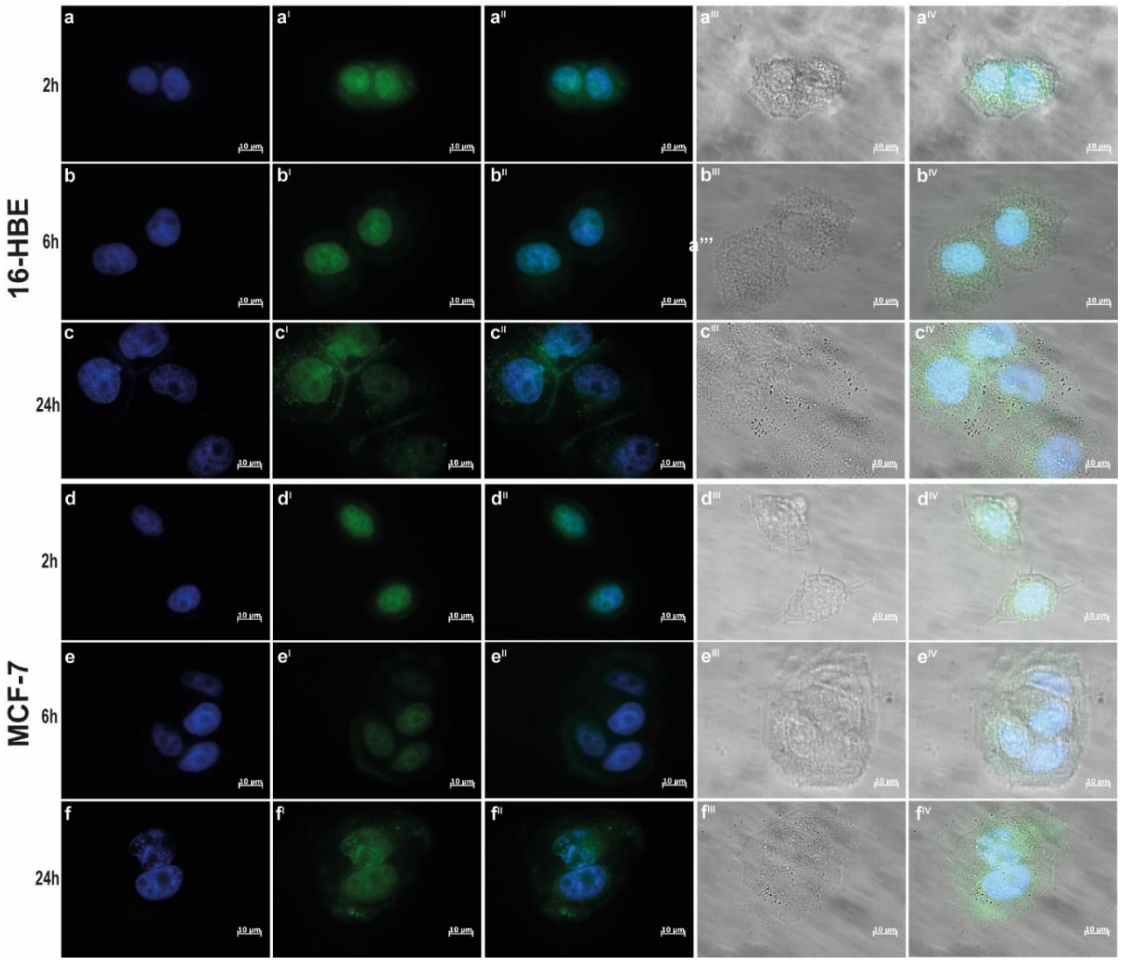

Figure 42. Cellular uptake kinetics of GdCDs on breast cancer (MCF-7) and bronchial epithelial (16-HBE) cells followed by widefield fluorescence microscopy. Nuclei are stained with DAPI (a−f), CDs-Gd are self-fluorescent in green (FITC channel) (a'−f'), merge (a''−f''), brightfield micrographs (a'''−f'''), and all channels merged (a^{IV}−f^{IV}). 100× magnification.

3.4.3. The NIR-triggered photothermal conversion ability of CDs-Gd enables local hyperthermic anticancer treatments

Carbon nanodots can also re-emit absorbed light by nonradiative processes, leading to local heat production. This phenomenon can be exploited to implement photothermal

treatments consisting in inducing local conditions of mild hyperthermia (42-49 °C) which directly damages cancer cells. To assess the photothermal conversion ability of GdCDs we evaluated the temperature increase produced in aqueous solutions at increasing concentrations of nanosystem, under 300s irradiation with a laser diode in the NIR region (λ = of 808 nm, 5 W cm^{-2}). The obtained kinetics, reported in Figure 43a, reveal that GdCDs exposed to a mild-power density of NIR light provoke a significant rise in solution temperature (ΔT = 20-31°C) compared to the pure solvent (ΔT = 13°C). The temperature increase is concentration- and time-dependent, thus a precise control of operative treatment conditions can be obtained by adjusting GdCDs dose and irradiation time.

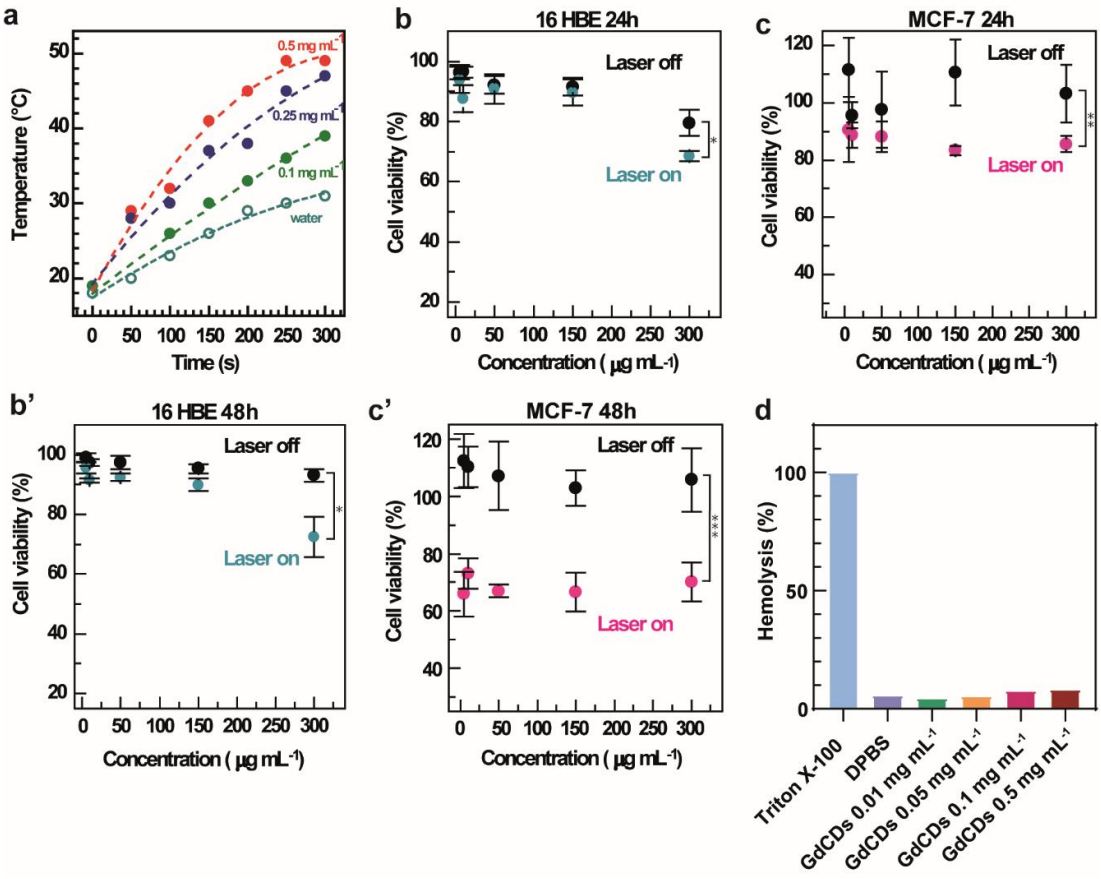

Figure 43. Properties of GdCDs as potential PTT agent against breast cancer. (a) Temperature kinetics of GdCDs aqueous dispersions or ultrapure water irradiated with an 810 nm diode laser for 300 s (2.5 W cm^{-2}). Photoinduced cytotoxic effect of GdCDs on 16-HBE (b−b') and MCF-7 (c−c') evaluated by MTS assay, evaluated after 24 h (b−c) or 48 h (b'−c') of incubation with increasing concentrations of CDs-Gd (0.05−0.3 mg mL^{-1}). Data are reported as mean ± SD (N = 3).

The effect of GdCDs treatment on cell viability was assessed by MTS assay after incubating both MCF-7 and 16-HBE cells with increasing concentrations of GdCDs (0.05 – 0.3 mg mL^{-1}) for 24 h or 48 h. Without exposure to NIR light, the nanosystem GdCDs induce only negligible cytotoxic effect on both tested cell lines, with cell viability beyond 80% even at the maximum concentration tested. Otherwise, NIR exposure of GdCDs treated cells (808 nm, 5 W cm^{-2}, 300s) caused a significant decrease in cell viability, although with remarkable distinctions between MCF-7 and 16-HBE cells. The NIR-triggered cytotoxic effect of GdCDs on breast cancer cells is more incisive compared to that on 16-HBE cells, which show significant cell viability reduction only at the higher concentration tested while demonstrating a good cytocompatibility up to 0.15 mg mL^{-1} of GdCDs. The time-dependent accumulation of the nanosystem, already observed in cellular uptake evaluation, resulted in an outstanding cytotoxic effect induced by irradiating cancer cells after 48 h incubation with GdCDs. The proven selectivity of NIR-triggered GdCDs' anticancer properties represent a huge advantage of our theranostic nanosystem over conventional treatments, such as chemotherapy, that indiscriminately target also healthy cells, provoking the well-known adverse effects of oncological therapy. Moreover, the

unique imaging properties of GdCDs can be exploited to guide the photothermal activation of the nanosystem on demand, enabling for extremely targeted treatments.

A preliminary assessment of the hemolytic activity of GdCDs was also performed to exclude any incompatibility with a possible parenteral administration. In particular, the 520 nm absorbance of erythrocytes' solutions treated with GdCDs (0.01 – 0.5 mg mL^{-1}) was evaluated as a parameter of hemoglobin release consequent to hemolysis. The relative hemolysis rate was calculated by comparing results to that of erythrocytes treated with DPBS pH 7.4 (negative control) and Triton X-100 (positive control), assumed as 100% of erythrocytes' lysis. As shown in Figure 43 d, GdCDs induced negligible hemolytic effect, comparable to that of negative control, at all the tested concentrations, demonstrating an excellent hemocompatibility.

4 – Materials and Methods

4.1. Materials

Urea (99%), citric acid (99.5%), amino-PEG_4-alkyne, Poly(ethylene glycol) bis(amine) (Mw=2000), ninhydrin, p-toluenesulfonyl chloride, citraconic anhydride (98 %), 1-Ethyl-3-(3-dimethylamino propyl) carbodiimide (EDC, 99.5 %), N-Hydroxysuccinimide (NHS, 99.5%), L-ascorbic acid (99%), copper (II) sulfate (99.5 %), 4-pentynoic acid (99.5%), 1,1,2,2-tetrachloroethane (99.9 %), Cetyltrimethylammonium bromide (CTAB, 99%), tetrachloroauric (III) acid trihydrate ($HauCl_4 \bullet 3H_2O$, 99 %), sodium borohydride ($NaBH_4$, 99.5%), reduced glutathione (GSH, 99.5%), sildenafil citrate (pharmaceutical secondary standard), 1-methyl-D-tryptophan (indoximod, 95 %), gadolinium chloride ($GdCl_3$), xylenol orange tetrasodium salt (XO), 2-azido-2-deoxy-D-glucose (97 %), SpectraPor® Float-A-Lyzer®G2 (MWCO 100–500 Da), SpectraPor® Pre-wetted RC Tubing (MWCO 1 kDa), cation exchange resin Dowex® (50 W × 8 100–200 mesh), Sephadex® G-10, G-15, and G-25 resins, thiazolyl blue tetrazolium bromide (97.5 %), N,N-dimethylformamide (DMF), tetrahydrofuran (THF), phosphate buffered saline (PBS), and Dulbecco's phosphate-buffered saline (DPBS) were purchased from Sigma Aldrich (Milan, Italy).

β-cyclodextrin (99%) and sodium azide (NaN_3 99.5%) were purchased from Fisher Scientific (Milan, Italy). 4′,6-Diamidino-2phenylindole (DAPI) was purchased from Life Technologies (Fisher Scientific - Milan, Italy).

Dulbecco's Minimum Essential Medium (DMEM), fetal bovine serum (FBS), L-glutamine, penicillin, streptomycin, and amphotericin B were purchased from EuroClone (Milan, Italy). CellTiter 96® AQueous One Solution Cell Proliferation Assay (MTS) was purchased from Promega (Milan, Italy).

The Reactive Oxygen Species (ROS) Detection Assay Kit was purchased from abcam plc. and used following the supplier's instructions for adherent cells.

4.2. Physical and chemical characterization

Fourier-transform infrared (FT-IR) spectroscopy

FT-IR spectra were recorded using a PerkinElmer Spectrum Two IR spectrometer (Waltham, MA) operating in the 4000 – 400 cm^{-1} range. Samples were prepared as KBr pellets, and dried under vacuum before the analysis.

Nuclear magnetic resonance (NMR)

^{1}H-NMR spectra were recorded by using a 400 MHz Advance II 400 spectrometer (Bruker Biospin) or an Avance II 300 spectrometer operating at 300.12 MHz.

Atomic force microscopy (AFM)

AFM micrographs were obtained using a FAST-SCAN microscope (Bruker) provided with a closed-loop scanner (Maximum scan region: X = 35 mm, Y = 35 mm, and Z = 3 mm) and equipped with a FAST-SCAN-A probe (5 nm optical radius), obtaining micrographs with a resolution comparable to the tip radius. Samples in water solution were deposited on a mica substrate and dried under vacuum before the analysis.

High-resolution transmission electron microscopy (HR-TEM)

HR-TEM micrographs were acquired using a JEM-2010 (JEOL) microscope at 200 kV electron energy. Samples were deposited as water solution on a commercial 400 μm mesh Cu-grid (Plano 01824) covered by a holey amorphous carbon film with a nominal thickness of 3 nm.

X-ray photoelectron spectroscopy (XPS)

X-ray photoelectron spectroscopy (XPS) spectra were recorded using a PHI 5000 VersaProbe II system (ULVAC-PHI, Inc.) equipped with a Kα source (1486.6 eV). Samples in aqueous solution were deposited on an aluminum plate (0.5 mL), that was dried under vacuum overnight before the analysis. Acquisition parameters: a beam of 100 μm ϕ, 25 W; time per step: 10 ms; energy step: 0.05 eV; pass energy: 23.50 eV; analyzer mode: FAT. The carbon (C 1s) line at 284.8 eV was used as reference energy.

UV/Visible absorption spectroscopy

UV/Visible absorption spectra were recorded using a double-beam spectrophotometer (Shimadzu UV-2401PC) operating in the 200-800 nm range (1 nm bandwidth).

Fluorescence spectroscopy

Fluorescence emission spectra were recorded using a Jasco FP-8500 spectrofluorometer (Milan, Italy) operating in 3D-spectra acquisition modality in the 350 – 850 nm range (λ_{EX} 340 – 650 nm).

Differential scanning calorimetry and thermogravimetric analysis (DSC/TGA)

Differential scanning calorimetry (DSC) and thermogravimetric analysis (TGA) were performed using a DSC/TGA EVO instrument (by SETARAM Instruments). Samples (~ 4 mg of dry powder) were placed into an aluminum crucible under an inert atmosphere (N_2 flow: 1 mL min^{-1}). Data were recorded in the 30-600 °C range, applying a heating rate of 10 °C min^{-1}.

4.3. Cell culture and animal models

Human breast cancer cell line MCF-7 (ER^+, overexpressing PDE-5) was obtained from "Istituto Zooprofilattico Sperimentale della Lombardia e dell' Emilia Romagna", Italy. Human immortalized bronchial epithelial cells 16-HBE and primary normal human dermal fibroblasts (NHDF) were purchased from Life Technologies (ThermoFisher Scientific). Human Schwann cell line - hTERT ipn02.3 2λ (ATCC CRL-3392) was purchased from ATCC.

Cells were cultured in 75 cm^2 culture flasks with a vented filter cap (Biosigma) at 37 °C in a humidified atmosphere of 5% CO_2. DMEM used for cell culture was supplemented with 10% (v/v) FBS, 100 units/mL penicillin G, 100 μg mL^{-1}, streptomycin, 0.1% (v/v), amphotericin B, and 2 mM L-glutamine.

The murine mammary cancer cell line E0771 was employed as an immune-resistant breast cancer *in vitro* model. Cells were cultured in Dulbecco's Modified Eagle Medium (DMEM) supplemented with heat-inactivated fetal bovine serum (FBS, 10 % v/v) and penicillin/streptomycin (100 unit mL^{-1}).

The E0771 cells were used to establish a syngeneic mammary adenocarcinoma model in C57BL/6j mice. Female C57BL/6j mice (10-12 weeks old) were purchased from

Instituto Gulbenkian Ciência (Portugal) and housed in the animal facility of the Faculty of Pharmacy (University of Lisbon). Animals were kept under a 12h-light/12h-dark cycle, with available food and water, and handled in compliance with the National Institutes of Health (NIH) and European Union guidelines (Directive 2010\63\EU). Animals were treated in compliance with the Portuguese competent authority for animal protection.

The inoculation was performed by orthotopic subcutaneous injection of E0771 cells (1.0×10^6 cells) suspended in a 1:1 mixture PBS/Matrigel® (100 μL) at the animal's fourth inguinal mammary fat pad. Mice weight and tumor size were monitored three times a week for the entire study duration. Tumors were measured using a digital caliper, and their volume was calculated by applying the ellipsoid volume formula.

4.4. Synthesis and characterization of β-cyclodextrins conjugated carbon nanodots loaded with sildenafil

4.4.1. Synthesis and characterization of mono-6-azido-6-deoxy-β-cyclodextrins (β-Cdx-N_3)

β-cyclodextrins (10 g, 8.8 mmol) were dispersed in ultrapure water (90 mL) and 35.2 mL of NaOH (2.5 M, 88 mmol) were added under magnetic stirring. After obtaining a fine dispersion, p-toluenesulfonyl chloride (2.52 mg, 13.22 mmol) was added and the solution was kept stirring at room temperature for 1h. The formed precipitate was withdrawn by filtration, and the filtered solution was treated with a pre-swollen cation exchange resin (Dowex®, 50 W × 8 100–200 mesh) and kept under stirring for 20 min. The exchange resin was removed by vacuum filtration through a Büchner funnel

with glass wool and washed with water and acetone. The product (β -Cdx-OTs) was dried under vacuum and obtained as a white powder with a 31 % yield.

β-Cdx-OTs (2.5 mg, 1.95 mmol) and NaN_3 (2.5 mg, 38.45 mmol) were dispersed in water under magnetic stirring and kept reacting at 100°C under reflux overnight. The reaction mixture was then cooled to room temperature and filtered through a paper filter. The filtrate was concentrated to about 15 mL by rotary evaporation and 3 mL of 1,1,2,2-tetrachloroethane were added dropwise. The resulting emulsion was maintained under week stirring for 30', then the aqueous phase was removed by centrifugation (3000 rpm, 5'). The organic phase was removed by rotary evaporation and the solid residue was crystalized twice in water. The product (Cdx-N_3) was obtained as white crystals by centrifugation (3000 rpm, 5') and vacuum drying (Yield: 40%).

β-Cdx-OTs: ^{1}H NMR (DMSO-d6, 300.12 MHz): δH 7.74–7.72 (2H, H8 Ph), δ 7.43–7.40 (2H, H7 Ph), δ5.75 (14H, OH-2/OH-3), δ 4.83–4.76 (7H, H1 Cdx), δ 4.33–4.29 (2H, H'6 Cdx, overlap with water), δ 4.18 (1H, H'5 Cdx, overlap with water), δ 3.31 (14H, H2/H4 Cdx, overlap with water), δ 2.14 (3H, Ph-CH3) ppm.

β-Cdx-N3: ^{1}H NMR (DMSO-d6, 300.12 MHz): δH 6.90 (C2H2Cl4 trace), δ 5.78–5.65 (14H, OH-2/OH-3 Cdx), δ 4.82 (7H, H1 Cdx), δ 4.57 (6H, OH-6 Cdx), δ 3.33–3.30 (14H, H2/H4 Cdx, overlap with water).

4.4.2. Synthesis of PEGylated carbon nanodots bearing an alkyne terminal group

Carbon nanodots (5.3 ± 4 nm) obtained as reported by CIT (20 mg, 2.86 mg mL^{-1}) and amino-PEG_4-alkyne (25 mg) were dispersed in PBS. The pH was adjusted to 6.4 and

EDC (24.92 mg, 0.13 mmol) and NHS (14.96 mg, 0.13 mmol) were added at once under stirring. The reaction was kept at pH 6.4 for 24 h, then the product (CDs-PEG-CC) was purified by dialysis against water using a SpectraPor® Float-A-Lyzer®G2 (MWCO 100–500 Da) for 36 h, and obtained by freeze-drying with a 77.3 % yield.

4.4.3. Conjugation of CDs-PEG-CC with Cdx-N_3

CDs-PEG-CC (10 mg) and Cdx-N_3 (20 mg) were dispersed in ultrapure water (6 mL), and copper II) sulfate (4 mg- 10 % cat.) and ascorbic acid (15 mg- 10 % cat.) were added to the mixture under stirring. The reaction was kept under nitrogen atmosphere and magnetic stirring overnight. The reaction mixture was treated with a cation exchange resin (Dowex®, 50 W × 8 100–200 mesh) for 10', then the resin was removed by filtration using a Büchner funnel with glass wool. The product (CDs-Cdx) was purified by size exclusion chromatography using a Sephadex® G15 and obtained as a dark powder after freeze-drying (Yield: 91%).

4.4.4. Preparation of sildenafil-loaded CDs-Cdx (CDs-Cdx@sildenafil)

Dried powders of CDs-Cdx (20 mg) and sildenafil citrate (5 mg) were pounded in a mortar to obtain a homogeneous mixture, which was then kneaded while adding aliquots of ethanol/water (70:30) solution dropwise. After the complete evaporation of the solvents, the obtained thin film was resuspended in 4 mL of ultrapure water by kneading. The suspension was kept stirring for 1h and dialyzed against water using a SpectraPor® Float-A-Lyzer®G2 (MWCO 500 Da) for 1h. The product was retrieved as brown powder by freeze-drying (Yield: 89 %).

4.4.5. Evaluation of drug loading and *in vitro* drug release kinetics

CDs-Cdx@sildenafil were solubilized in an acetonitrile/water (pH 4.0) (35:65) solution and sonicated for 2h. The sample was filtered (0.45 μm) and analyzed by HPLC using an Agilent 1260 infinity HPLC System equipped with a C6-Phenyl column (Phenomenex®) under isocratic conditions using the same mixture as eluent solution (flow rate 0,8 mL min^{-1}, temperature 25 °C, UV detector λ = 291 nm). The retention time was 4.8 min. To evaluate the amount of sildenafil, the peak area of each sample was compared to a calibration curve obtained using sildenafil citrate standard solutions ranging from 0.1 to 0.005 mg mL^{-1} (y = 28,705x, R2 = 0.999). (Drug loading, DL = 19.9 % w/w).

To evaluate the drug release kinetics, CDs-Cdx@sildenafil or free sildenafil at equivalent drug concentration (0.19 mg mL^{-1}) were dispersed in 1 mL of a 1 % Tween80 PBS pH 7.4 solution, and dialyzed against 10 mL of the same medium. At scheduled time intervals (1 h, 2 h, 4 h, 6 h, 8 h, 24 h and 48 h), the external medium (0.5 mL) was withdrawn and replaced with fresh medium. The amount of sildenafil was then determined by HPLC, using the above described method. The cumulative release of sildenafil was plotted over time (N = 3).

4.4.6. *In vitro* cellular uptake and intracellular distribution studies

The internalization of CDs-Cdx by healthy (NHDF), pre-cancerous (16-HBE), and breast cancer (MCF-7) cell lines was evaluated by fluorescence microscopy. In detail, cells were seeded on an 8-well-chambered coverglass at 5×10^3 cells per well density, and cultured in DMEM for 24 h. Successively, the medium was replaced with 200 μL

of CDs-Cdx dispersion in DMEM (150 μg mL^{-1}). After 24 h of incubation, the medium was removed and each well was washed twice in DPBS. Cell uptake micrographs were obtained using a fluorescence microscope Axio Cam MRm (Zeiss) leveraging the intrinsic multicolor emission of CDs-Cdx for intracellular tracking.

4.4.7. *In vitro* evaluation of CDs-Cdx@sildenafil mediated cytotoxicity

The cytocompatibility of CDs-Cdx and CDs-Cdx@sildenafil was assessed *in vitro* on NHDF, 16-HBE, and MCF-7 cell lines. Each cell line was seeded on a 96 wells-plate with 1.5×10^4 cells per well density, and cultured for 24 h in DMEM at 37 ◦C and 5 % CO^2. After that, the culture medium was replaced with dispersions of CDs-Cdx (200 μL, 10 - 250 μg mL^{-1}), sildenafil citrate 0.5 – 50 μg mL^{-1}), or CDs-Cdx@sildenafil at equivalent drug concentration. Cell were incubated for 24 h or 48 h, then the dispersion was removed and each well was washed three times with DPBS at pH 7.4 before performing the cell viability assay. The cell viability was evaluated using the cell proliferation MTS assay, incubating each well with 120 mL of an MTS working solution (1:5 MTS assay solution/DMEM) for about 2 h. Cell viability was obtained by measuring the absorbance at 492 nm using a microplate reader (Multiskan, Thermo, U.K.). Untreated cells were used as control and assumed as 100% cell viability. All biological experiments were performed in triplicate.

4.4.8. Detection of reactive oxygen species (ROS) on cells treated with CDs-Cdx@sildenafil

NHDF, 16-HBE, and MCF-7 were seeded in a 96 wells-plate at a 2.5×10^4 cells per well density, and cultured in DMEM at 37 °C and 5 % CO_2. After 24h, the culture

medium was replaced with DMEM solutions of CDs-Cdx, sildenafil citrate, or CDs-Cdx@sildenafil at the IC50 concentration, for 24h or 48h. The medium was then withdrawn, and cells were treated with the ROS Assay Buffer I/ROS Label following the supplier's instructions (Reactive Oxygen Species - ROS - Detection Assay Kit by abcam plc.). Thus, cells were washed up with DPBS pH 7.4 (200 μL) and treated with ROS Assay Buffer I/ROS Assay Buffer (100 μL) to measure fluorescence immediately by a multiplate reader (Ex/Em = 495/529 nm, Multiskan, Thermo, U.K.). Untreated cells were used as negative control, while cells treated with tert-Butyl hydroperoxide (100 μL, 1 μM) were used as positive control. The signal of the cells' autofluorescence was subtracted from the measures.

4.4.9. Analysis of gene expression

Cells treated with CDs-CDx, sildenafil citrate, or CDs-Cdx@sildenafil, and untreated cells were treated with the TRIzol Reagent (Invitrogen Corporation, Carlsbad, CA, USA) following the manufacturer's instructions for the total RNA extraction. Samples were stored at – 80°C. RNA samples were treated with DNase I (Amplification Grade, Sigma-Aldrich, Milan, Italy) at 37°C for 30' to remove any genomic DNA contamination. Subsequently, the DNase I was inactivated by adding 50 mM EDTA. First-strand cDNA was synthesized from RNA samples using the High-Capacity cDNA Reverse Transcription Kit (Thermo Fischer Scientific, Carlsbad, CA, USA), following the manufacturer's instructions. The cDNA mixture was diluted 1:5 before use in Real-Time qPCR experiments. qPCRs analyses were performed using the BIO-RAD CFX96 system equipped with BlasTaq 2X qPCR MasterMix (Applied Biological Materials Inc, Richmond, BC, Canada) as detection chemistry. ACTB and

GAPDH genes were selected as control genes based on their expression stability in all tested conditions. A normalization factor was calculated based on geometric averaging of ACTB, and GAPDH expression and was used to quantify the mRNA levels of the target genes (Vandesompele et al., 2002). Serial dilutions of pooled cDNAs from both control and treated samples were prepared to determine the PCR efficiency of the target and reference genes (data not shown), with amplification efficiency ranging from 1.9 to 2.1. Primer sequences used in this study are listed in Table 4. The amplification conditions were: 3' of initial denaturation at 95°C, 40 cycles of 15s at 95°C and 60s at 60°C, followed by a melting curve from 60°C to 95°C. Amplicons were detected by agarose gel analysis after each PCR to confirm the amplification of the specific gene product. Gene expression results are presented as heat maps mRNA levels are represented as mean-centered; S.D. (n = 3) were below 0.5%. The graphs were generated via R software v. 3.5.0.

Gene name	Primer pairs	GeneBank accession numbers	Gene name	Primer pairs	GeneBank accession numbers
ALOX12 FOR	CCTCGTTATGCTGAAGATGGAGC	NM_000697	PTGS2 FOR	CGGTGAAACTCTGGCTAGACAG	NM_000963
ALOX12 REV	ATTTCGGACCCAGGACTTTGCC		PTGS2 REV	GCAAACCGTAGATGCTCAGGGA	
CAT FOR	GTGCGGAGATTCAACACTGCCA	NM_001752	SOD1 FOR	CTCACTCTCAGGAGACCATTGC	NM_000454
CAT REV	CGGCAATGTTCTCACACAGAG		SOD1 REV	CCACAAGCCAAACGACTTCCAG	
FTH1 FOR	TGAAGCTGCAGAACCAACGAGG	NM_002032	SOD2 FOR	CTGGACAAACCTCAGCCCTAAC	NM_000636
FTH1 REV	GCACACTCCATTGCATTCAGCC		SOD2 REV	AACCTGAGCCTTGGACACCAAC	
GCLC FOR	GGAAGTGGATGTGGACACCAGA	NM_001498	SQSTM1 FOR	TGTGTAGCGTCTGCGAGGGAAA	NM_003900
GCLC REV	GCTTGTAGTCAGGATGGTTTGCG		SQSTM1 REV	AGTGTCCGTGTTTCACCTTCCG	

GPX1 FOR	GTGCTCGGCTTCCCGTGCAAC	NM_000581	AKR1C2 FOR	CAGTGGATCTCTGTGCCACATG	NM_001354
GPX1 REV	CTCGAAGAGCATGAAGTTGGGC		AKR1C2 REV	CTGGTTGCAGACAGGCTTGTAC	
GSR FOR	TATGTGAGCCGCCTGAATGCCA	NM_000637	GCLM FOR	TCTTGCCTCCTGCTGTGTGATG	NM_002061
GSR REV	CACTGACCTCTATTGTGGGCTTG		GCLM REV	TTGGAAACTTGCTTCAGAAAGCAG	
GSTP1 FOR	TGGACATGGTGAATGACGGCGT	NM_000852	HMOX1 FOR	CCAGGCAGAGAATGCTGAGTTC	NM_002133
GSTP1 REV	GGTCTCAAAAGGCTTCAGTTGCC		HMOX1 REV	AAGACTGGGCTCTCCTTGTTGC	
NOS2 FOR	GCTCTACACCTCCAATGTGACC	NM_000625	NQO1 FOR	CCTGCCATTCTGAAAGGCTGGT	NM_000903
NOS2 REV	CTGCCGAGATTTGAGCCTCATG		NQO1 REV	GTGGTGATGGAAAGCACTGCCT	
PRDX1 FOR	CTGCCAAGTGATTGGTGCTTCTG	NM_002574	TXN FOR	GTAGTTGACTTCTCAGCCACGTG	NM_003329
PRDX1 REV	AATGGTGCGCTTCGGGTCTGAT		TXN REV	CTGACAGTCATCCACATCTACTTC	
ATR FOR	GGAGATTTCCTGAGCATGTTCGG	NM_001184	TXNRD1 FOR	GTAGTTGACTTCTCAGCCACGTG	NM_003330
ATR REV	GGCTTCTTTACTCCAGACCAATC		TXNRD1 REV	CGCACTCCAAAGCGACATAGGA	
CHEK1 FOR	GTGTCAGAGTCTCCCAGTGGAT	NM_001114121	MRE11A FOR	CAGCAACCAACAAAGGAAGAGGC	NM_005590
CHEK1 REV	GTTCTGGCTGAGAACTGGAGTAC		MRE11A REV	GAGTTCCTGCTACGGGTAGAAG	
GADD45A FOR	CTGGAGGAAGTGCTCAGCAAAG	NM_001199741	RAD51 FOR	TCTCTGGCAGTGATGTCCTGGA	NM_001164269
GADD45A REV	AGAGCCACATCTCTGTCGTCGT		RAD51 REV	TAAAGGGCGGTGGCACTGTCTA	
ACTB FOR	CACCATTGGCAATGAGCGGTTC	NM_001101	GAPDH FOR	GTCTCCTCTGACTTCAACAGCG	NM_002046
ACTB REV	AGGTCTTTGCGGATGTCCACGT		GAPDH REV	ACCACCCTGTTGCTGTAGCCAA	

Table 4. Primer sequenced used for gene expression analysis.

4.5. Synthesis and characterization of indoximod conjugated carbon nanodots

4.5.1. PEGylation of carbon nanodots

Carbon nanodots (CDs, 50 mg), prepared as reported by Mauro et al., 2022, and poly(ethylene glycol) bis(amine) (Mw 2000, 200 mg) were solubilized in ultrapure water (5 mL). The pH of the solution was adjusted to 6.8 and EDC (19.2 mg, 0.1 mmol) and NHS (11.5 mg, 0.1 mmol) were added at once, and the reaction was kept under stirring overnight at pH 6.8. The product (CDs-PEG) was purified by dialysis using a SpectraPor® Pre-wetted RC Tubing (MWCO 1kDa), and freeze-dried.

The amount of PEG bound to CDs was determined indirectly using ninhydrin as indicator for the quantitative spectroscopical evaluation of the terminal -NH_2 pendants. In details, a sample of CDs-PEG (1 mL, 0.2 mg mL^{-1}) was treated with 1 mL of 1 % (w/v) ninhydrin solution in ethanol (2.5%). The absorbance of the mixture at 570 nm was compared to those of glycine standard solutions (0 – 10 mM) treated similarly.

In parallel, the amount of PEG chains in CDs-PEG was evaluated by ^{1}H-NMR using acetone (2.5 μL) as an internal standard (i.s.).

4.5.2. Conjugation of CDs-PEG with indoximod though a citraconate linker

178 mg of CDs-PEG were solubilized in water and the pH was adjusted to 9. Citraconic anhydride (357 μL, 3.97 mmol) diluted in THF (2 mL) and added dropwise under stirring to the solution of CDs-PEG, while maintaining the pH at 9.0 ± 1.0 with NaOH (1M). The mixture was kept reacting for 3 h, then the product was purified by dialysis

against water, using a SpectraPor® Pre-wetted RC Tubing (MWCO 1kDa). The product (CDs-PEG-CA) was obtained after freeze-drying with a 77.8% yield. Lastly, 88 mg of CDs-PEG-CA and 12 mg of indoximod (IND) (55 μmol) were solubilized in 12 mL of ultrapure water and the pH was adjusted to 6.8. Then, EDC (8.5 mg, 55 μmol) and NHS (6.3 mg, 55 μmol) were added under magnetic stirring, and the mixture was kept reacting overnight. The product (CDs-IND) was dialyzed against water using a SpectraPor® Pre-wetted RC Tubing (MWCO 1kDa), and freeze-dried (Yield = 70%).

4.5.3. *In vitro* evaluation of CDs-IND mediated cytotoxic effect

The impact of CDs-IND on cell viability was evaluated *in vitro* on murine fibroblasts (NIH/3T3) used as healthy cellular model, and on a murine mammary cancerous cell line (E0771), by MTT assay. Briefly, cells were seeded at 3.5×10^3 cells per well density on a 96 well-plate, and cultured at 37 °C and 5% CO_2 for 24h. Then, the culture medium was replaced with 150 μL of either CDs-IND solutions in DMEM (0.1 – 2 mg mL^{-1}), or CDs-PEG or free IND at an equivalent concentration. After 48h the cell culture medium was retrieved and the wells were washed twice with PBS, pH 7.4, then cells were incubated with a thiazolyl blue tetrazolium bromide solution in DMEM (50 μL, 0.5 mg mL^{-1}). After 2h, 100 μL of DMSO were added to each well resuspend the formed crystals. The absorbance of the samples at 570 nm was measured using a Varioskan Lux microplate reader (Thermofisher scientific). Cells treated with Tween 20 were used as positive control and untreated cells were used as negative control, assumed as 100% cell viability. The experiment was performed twice in triplicate.

4.5.4. *In vitro* cellular uptake of CDs-IND evaluated by fluorescence microscopy

E0771 cells were seeded in an ibidi® μSlide-8well at a cell density ranging from 9.0 × 10^3 to 3.0 × 10^3 cells per well, and cultured for 24 h. Then, the culture medium was withdrawn and cells were treated with CDs-IND (150 μL, 1.5 mg mL^{-1}), or with fresh medium for autofluorescence controls. At scheduled time intervals (24, 48, and 72 h), cells were washed with PBS and fixed with 4 % buffered formaldehyde (PFA). Nuclei were stained using the Hoechst 33342 dye (150 μL, 5 μg mL^{-1}). Confocal fluorescence microscopy was performed using a Leica TCS SP8 (Leica Microsystems CMS GmbH, Mannheim, Germany) inverted microscope (DMi8) with a 63× oil (1.4 numerical aperture) HC PL APO objective.

4.5.5. *In vivo* evaluation of CDs-IND mediated antitumoral effect

At day 7 after the inoculation of E0771 cells, mice presenting palpable tumor masses of ~67 mm^3 average volume were randomized into four treatment groups (N=5-7 per group). Animals were treated by intratumoral (IT) administration of CDs-IND 1.12 mg mL^{-1} (50 μL, 2.8 mg kg^{-1}) or equivalent amounts of CDs-PEG or free IND (8.6 μg mL^{-1}, 40 μM), and untreated animals were used as control. The treatment was repeated 5 times, three days apart. Tumor sizes and mice weight were monitored three times a week. At day 20, all mice were euthanized, and spleens and tumors were harvested and preserved in cold sterile PBS (pH 7.4) for subsequent experiments.

In a parallel experimental set, mice were treated by intravenous (IV) administration of CDs-IND (1.12 mg mL^{-1}, 100 μL, 5.6 mg kg^{-1}), following the same treatment schedule (N=5). The day after the last treatment (day 20), mice were euthanized, and the spleen

and the tumor were harvested and preserved in cold sterile PBS (pH 7.4) for subsequent experiments.

4.5.6. Flow cytometry evaluation of immune profile

Tumors and spleens were disrupted mechanically and treated with an enzymatic digestion solution, consisting of RPMI medium with 0.5% (m/v) BSA, 0.1% (m/v) collagenase type II, 0.1% (m/v) dispase, and DNAse, for 20' at 37°C. The obtained cell suspension was filtered through a 70 μm filter (BD Biosciences) and diluted with cold PBS (pH 7.4). Cells were seeded in U-bottom 96 well plates (3.0×10^6 cells per well), washed with PBS, and stained with Ghost Dye™ Red 780 for cell viability. Cells were then washed with FACS buffer (0.5% (m/v) BSA, 2 mM EDTA in PBS) and stained for surface markers: CD45 (AF532, clone 30-F11), CD3 (FITC, clone 17A2), CD4 (perCP-Cy5.5, clone GK1.5), CD8 (AF700, clone 53-6.7), IDO (PE, clone Mido-48), CD279 (SB600, clone J43), CD107b (AF647, M3/84), CD25 (PECy5, clone PC61), NK1.1 (BV570, clone PK136), CD274 (BV711, clone 10F.9G2), CD223 (PE-Cy7, clone eBioC9B7W), CD11b (BV785, clone M1/70), CD11c (PECy5, clone N418), F4-80 (BV711, clone BM8), MHCII (AF700, clone M5/114.15.2), CD206 (PECy7, clone C086C2). All staining was performed in FACS buffer. To analyze FOXP3 expression, cells were further fixed and permeabilized using the eBioscience™ FOXP3/Transcription factor staining buffer set, according to the manufacturer's protocol, and stained with FOXP3 (eFluor450, clone FJK-16s). Cells were analyzed using a Cytek Aurora (Cytek) and data analysis was performed using FCS Express (De Novo Software).

4.6. Synthesis and characterization of glucose-functionalized gold/carbon nanodots

4.6.1. Synthesis of gold seeds

The synthetic protocol for gold seeds was performed according to the first step of seed-mediated synthesis of gold nanoparticles, reported in literature (Varvarà et al., 2020). Briefly, $HAuCl_4$ (25 mL, 50 mM) was added to a CTAB solution (4.7 mL, 0.1 M) under vigorous stirring. 300 μL of $NaBH_4$ (10 mM) were added at once to the mixture, which color immediately changed from light yellow to dark pink. The excess of CTAB was precipitated at 4 °C and removed by centrifugation (12,000 rpm, 20′). To further stabilize the colloidal dispersion, GSH (7.5 mg) was added and the solution was kept equilibrating for 2 h. The effective achievement of a stable dispersion of gold seeds was evaluated by recording their UV–Vis absorption spectrum.

4.6.2. Synthesis and characterization of hybrid gold-carbon nanodots (AuCDs)

Six batches of gold seeds were reunited and concentrated by rotary evaporation to a final volume of ~ 6 mL. The concentrated dispersion of gold seeds was added to a solution of citric acid (3 g, 16 mmol) and urea (6 g, 98 mmol) in DMF. The mixture was kept reacting in a steel autoclave (Büchi AG, Miniclave steel type 3, Gschwaderstrasse, Switzerland) at 170 °C for 4 h. The solvent was removed by rotary evaporation and the product was washed with a ethanol/diethyl ether (1:9) mixture, which was also removed by rotary evaporation. The product was resuspended in ultrapure water and purified by size exclusion chromatography using a glass column packed with, in turn, Sephadex® G-10, G-15, and G-25, and using water as eluent. The

collected fractions were grouped based on their optical properties, and freeze-dried. The most interesting fraction, named AuCDs, was selected for the subsequent functionalization processes.

Quantification of gold incorporated within AuCDs

The amount of gold embedded in the structure of AuCDs was evaluated using the Spectroquant® Gold Test (Merck) kit, following the manufacturer's instructions. Before performing the analysis, a sample of AuCDs was solubilized in 10% (v/v) HNO_3 and mineralized by undergoing heating cycles (5′ at 100 °C and 15′ at 200 °C) using a microwave synthesizer Discover SP (CEM). The gold concentration was calculated by comparison with a calibration curve obtained with Au (III) solutions (60–5 mM).

4.6.3. Synthesis of 2-Deoxy-D-Glucose-Functionalized AuCDs (AuCDs-Glu)

A three-step synthetic protocol was adopted to obtain the surface functionalization of AuCDs with 2-deoxy-D-glucose moieties. In the first preliminary step, poly(ethylene glycol) bis(amine) (Mw 2000) (500 mg) and 4-pentynoic acid (29.4 mg) were dissolved in 8 mL of PBS and the pH was adjusted to 6.4. Then, EDC (57.6 mg) and NHS (34.8 mg) were added and the reaction was kept under magnetic stirring overnight. The obtained hetero bi-functional PEG bearing an alkyne terminal function was purified by size exclusion chromatography using a Sephadex® G15-G25 stationary phase, and freeze-dried (38% yield). Subsequently, 125 mg of H_2N-PEG-CC were added to 5 mL of an AuCDs aqueous solution (2 mg mL^{-1}), and the pH was adjusted to 6.4. Then, EDC (15 mg, 0.078 mmol) and NHS (9.01 mg, 0.078 mmol)

were added and the mixture was kept under magnetic stirring overnight. The product (AuCDs-PEG-CC) was purified by dialysis (1 kDa MWCO) against water for 72 h, and then it was freeze-dried, obtaining a dark powder with a 30.2% yield. Lastly, 2-azido-2-deoxy-D-glucose (2.1 mg, 1.0 mmol) and AuCDs-PEG-CC (20 mg) were solubilized in ultrapure water (3 mL), and copper (II) sulfate (1.0 mg, 6.0 mmol) and ascorbic acid (10 mg, 6.0 mmol) were added in order under inert atmosphere and magnetic stirring. After 24 h of reaction, the mixture was purified by dialysis against water using a SpectraPor® Pre-wetted RC Tubing (MWCO 1kDa). After 72 h the purified product, named AuCDs-Glu, was obtained by freeze-drying (98.6% yield).

4.6.4. Evaluation of computed tomography (CT) contrast of AuCDs-Glu

The performance of AuCDs-Glu as contrast agents for computed tomography (CT) was evaluated by acquiring micro-CT micrographs of an aqueous solution of AuCDs-Glu (0.5 mg mL^{-1}) inside a capillarity (~ 5 cm), using a Bruker SKYSCAN 1272 (Karlsruhe, Germany) operating with a power of 40 kV, an intensity of 250 μA, and using an aluminum filter to optimize acquisitions. Water was used as control.

The experiment was repeated on a living fungi model to establish the CT contrast of AuCDs-Glu in organic tissues. Briefly, pieces cutted from the hyphal fronts of *P. Italicum* were placed in a malt medium agar plates (malt extract broth, Oxoid, Unipath Ltd., Hampshire, England) to establish a fungi culture. After 25 days, fungi hyphae of about 2.5 mm were retrieved and incubated with AuCDs-Glu (0.5 mg mL^{-1} in water), or ultrapure water for controls, for 24 h. Then, the micro-CT analysis was performed adopting the same analysis parameters previously described.

4.6.5. Evaluation of glucose-mediated cellular uptake of AuCDs-Glu

The cellular internalization of AuCDs-Glu was evaluated *in vitro* on breast cancer (MCF-7) and non-cancerous Schwann cells (HSC - hTERT ipn02.3 2λ). Cells were seeded on a 8-well Nunc Lab-Tek chambered coverglass (Thermo Fisher Scientific,Waltham, MA USA) at a 10^4 cell density, and cultured in complete DMEM. After 24 h, the culture medium was removed, and cells were incubated with 120 μL of a D-glucose solution in DMEM (250 mM) or 120 mL of DMEM for 30'. Then, 30 μL of an AuCDs-Glu dispersion in DMEM (1.0 mg mL^{-1}) were added to each well. After 24 h, cells were washed twice with PBS, and fixed with 4% buffered formalin. Micrographs were obtained using a widefield fluorescence microscope Axio Cam MRm (Zeiss) (100× magnification).

4.6.6. Cytocompatibility assay

The cytocompatibility of AuCDs-Glu was assessed in vitro by MTS cell viability assay on both human breast cancer (MCF-7) and non cancerous human Schwann (HSC-hTERT ipn02.3 2λ) cell lines. Cells were seeded in a 96-well plate (1.5×10^4 cells per well) and cultured in complete DMEM at 37 °C and 5 % CO_2. After 24 h, the culture medium was replaced with either 150 mL AuCDs-Glu dispersions in DMEM (1.00–0.01 mg mL^{-1}) or fresh medium for negative controls. After 48 h, cells were washed with PBS (pH 7.4) and treated with 120 mL of an MTS working solution (1:5 MTS assay solution/DMEM). After 2 h of incubation, a Multiskan microplate reader (Thermo, Dublin, UK) was used to record the 492 nm absorbance of the samples. Data were reported as percentage of cell viability, calculated by comparing the data to negative controls, assumed as 100% cell viability.

4.7. Synthesis and characterization of gadolinium-doped carbon nanodots

Urea (6 g, 99.9 mmol), citric acid (3 g, 15.6 mmol), and gadolinium(III) chloride (579.8 mg, 1.56 mmol) were solubilized in DMF and kept under solvothermal conditions at 160 °C in a steel autoclave (Büchi AG, Miniclave steel type 3, Gschwaderstrasse, Switzerland) for 4 h. Then, the reaction mixture was cooled to room temperature, and the organic solvent was removed by rotary evaporation. The dark crude was resuspended in ultrapure water by sonication and filtered through a paper filter. The product was purified by size exclusion chromatography using water as eluant, and a glass column packed with, in turn, Sephadex® G-15 and G-25 as stationary phase. The collected fractions were grouped based on their optical properties, and the most interesting, indicated as GdCDs, underwent a further purification in by size exclusion chromatography in acidic conditions (pH 1.0), using a Sephadex® G-10 as stationary phase. The yield of GdCDs was 109.3 mg.

4.7.1. Quantification of Gd^{+3} ions entrapped within the structure of GdCDs

The amount of Gd^{+3} ions in GdCDs was determined spectroscopically using xylenol orange tetrasodium salt (XO) as metal indicator. A sample of GdCDs (2 mg) was solubilized in HNO_3 (10% v/v) and treated with heating cycles (5' at 100 °C followed by 15' at 200 °C) using a microwave synthesizer Discover SP (CEM). The mineralized sample was cooled to room temperature, and the pH was adjusted to 5.8. Then, 50 μL of the sample were treated with 950 μL of XO in acetate buffer pH 5.8 (16 μg mL^{-1}) and the absorption spectrum of the mixture was recorded in the 400−600 nm range.

The amount of Gd^{+3} was calculated by comparing the 573 nm/433 nm absorbance ratio with a calibration curve obtained with $GdCl_3$ standards (10−30 μM) in acetate buffer solution pH 5.8 (R2 = 0.993).

4.7.2. Evaluation of magnetic resonance imaging (MRI) contrast properties of GdCDs

GdCDs samples were prepared as aqueous solutions (0.01 – 0.5 mg mL^{-1} corresponding to 1.1 – 10.8 μM of Gd^{+3}) in in acetate buffer (pH 5.5, 5 mM), phosphate buffer (pH 6.4, 5 mM), or phosphate buffer (pH 7.4, 5 mM). *In vitro* MRI acquisitions were obtained using a Philips Achieva 1.5T MRI clinical scanner equipped with an eight-channel phased-array-head coil. For the analysis, 3 mL of each sample were transferred in a conical vial and placed in the head coil with the aid of a nonmagnetic holder. The longitudinal relaxation time (*T1)* was measured using an inversion recovery sequence, and images were acquired with variable inversion times (TI) in the 25 – 3000 ms range. Acquisition parameters: echo time (TE) of 15 ms, maximum repetition time (TR) of 4000 ms, matrix size of 256 × 256, slice thickness of 2.5 mm, and field of view of 25.6 × 25.6 cm^2. A Python code was developed to analyze the data identifying a region of interest (ROI) at the center of each sample and calculating the average signal intensity and its standard deviation. T1 values were calculated by applying the equation:

$$(TI) = M0 \times (1 - b \times e{-}TI/T1)$$

where M0, b, and T1 are the fitting parameters.

Finally, the relaxation rate (R1) values were determined to be the reciprocal of T1 (s^{-1}).

4.7.3. Temperature kinetics of GdCDs solutions under NIR irradiation

The photothermal conversion ability of GdCDs was indirectly evaluated by monitoring the temperature increase of GdCDs aqueous solutions (0.1 – 0.5 mg mL^{-1}) over the irradiation time and using an 810 nm diode laser (GBox 15A/B GIGAA laser) at 2.5 W cm^{-2} for 300 s. An infrared optical fiber (CEM) was used for detecting the temperature. Ultrapure water was used as control.

4.7.4. Cellular uptake of GdCDs

The cellular internalization of GdCDs on human bronchial epithelial (16-HBE) and human breast cancer (MCF-7) cell lines was evaluated by widefield fluorescence microscopy. Cells were seeded on 8 well-chambered coverglass (Nunc Lab-Tek - Thermo Fisher Scientific) at a 10^4 cell density and cultured in complete DMEM. After 24 h, the culture medium was replaced with GdCDs dispersions in complete DMEM (250 μL, 0.15 mg mL^{-1}). At scheduled time intervals (2, 6, and 24 h), the medium was replaced with DPBS pH = 7.4, and cells were washed three times. Cells were fixed using 4% buffered formalin and nuclei were stained with DAPI (50 μL × 5 min). Cell uptake micrographs were obtained with a widefield fluorescence microscope Axio Cam MRm (Zeiss) (100× magnification).

4.7.5. Evaluation of NIR-triggered photoinduced cytotoxic effect mediated by GdCDs

The impact of GdCDs on cell viability was assessed *in vitro* on both breast cancer (MCF-7) and human bronchial epithelial (16-HBE) cell lines using the MTS assay (Promega). Briefly, cells were cultured in 96-well plates (1.5×10^4 cells per well) for 24h, then the culture medium was replaced with either GdCDs dispersions in DMEM (200 μL, 0.05−0.3 mg mL^{-1}) or 200 μL of fresh medium (negative controls). After 24 or 48 h of incubation, the medium was removed and each well was washed twice with DPBS (pH 7.4) before incubating with a MTS working solution (120 μL, 1:5 MTS assay solution/DMEM) for 2 h. The percentage of cell viability was calculated by comparing the 492 nm absorbance of the samples with those of negative controls, assumed to be 100% cell viability.

The near-infrared (NIR)-triggered photoinduced cytotoxic effect mediated by GdCDs was evaluated on the same cell lines by MTS assay. Cells, treated as previously described, were further irradiated with a 810 nm diode laser (GBox 15A/B diode GIGAA laser) with a 5 W cm^{-2} power density for 300 s before performing the MTS assay.

To establish eventual hemolysis phenomena occurring in the presence of GdCDs, a suspension of erythrocytes in DPBS pH 7.4 (4% v/v), isolated from a whole blood sample by centrifugation (500g × 10 min × 2), was treated with GdCDs at increasing concentrations (0.01−0.5 mg mL^{-1}) for 1 h. Subsequently, each sample was centrifuged (500g × 5 min), and the absorbance at 520 nm of the supernatant was

measured using a microplate reader (Multiskan, Thermo, UK). The absorbance of samples treated with Triton X-100 were considered as 100% of lysis.

All experiments were performed in triplicate, and the results are expressed as mean values ± standard deviation.

4.8. Statistical data analysis

Statistical analysis was performed by Student's T-test (two-tailed) for comparing two groups, and one-way analysis of variance (ANOVA) followed by Tukey's post-hoc analysis for comparing sets of data composed of multiple groups. Statistical calculations were performed using the Microsoft®-Excel data analysis tool and the software package GraphPad Prism (V.7.03). Data were reported as mean value ± standard deviation (SD) or mean value ± standards errors of the mean (SEM). Comparisons were considered statistically significant at $p < 0.05$ (∗), $p < 0.01$ (∗∗), $p < 0.001$ (∗∗∗), and $p < 0.0001$ (∗∗∗∗).

5 – Conclusions

The present thesis proposed four innovative multifunctional nanoplatforms that proved the huge potential of carbon-based theranostic nanosystems in breast cancer precision medicine. Leveraging the outstanding versatility and unique properties of CDs, the antitumoral nanosystems here presented propose different multimodal antitumoral approaches for breast cancer therapy, including delivery of actives that synergize with the inherent anticancer activity of CDs, thus promoting direct ROS-mediated cancer cells damage and favoring immunostimulation resulting in controlled tumor growth, and development of hybrid nanomaterials endowed with multimodal imaging ability with promising applications in breast cancer targeting and imaging-guided photothermal therapy.

The synthetic protocol adopted to functionalize sulfur- and nitrogen-doped CDs with β-Cdx led to well-organized ultrasmall nanostructures of about 8 nm diameter, that have been successfully employed for loading sildenafil, achieving a remarkable percentage of drug loading (20.6 % w/w). CDs-Cdx@Sildenafil demonstrated a preferential cytotoxic effect towards cells overexpressing PDE-5, enhancing the intrinsic ability of CDs to induce ROS overproduction in tumor cells. Indeed, CDs-Cdx conjugates delivering sildenafil promoted ROS production and upregulation of ROS-responding genes with significant differences compared with CDs-Cdx and free sildenafil. Therefore, sildenafil repurposing as a PDE-5 inhibitor, in combination with the inherent antitumoral properties of CDs through ROS production, holds great promise in precision cancer therapy.

The inherent anticancer properties of CDs were exploited to implement a dual-mode breast cancer immunotherapeutic approach by conjugation with the immune adjuvant indoximod. The conjugation, performed through a simple three-step synthetic protocol, yield an innovative nanostructure that retains the advantageous chemical, physical, and optical properties of the bare CDs, including the bright green photoluminescent that has been exploited to track the internalization of the nanosystem, proving its self-tracking potential for biomedical applications. *In vitro*, CDs-IND showed a dose-dependent antitumoral effect referable to the established antitumoral properties of CDs, although these are mitigated by surface functionalization. *In vivo* studies performed on murine models of breast cancer demonstrated that both IT and IV administration of the CDs-IND conjugate resulted in a significant reduction of tumor burden in mice, whereas neither CDs-PEG nor free IND managed to slow the exponential growth of tumor cells, even when locally administrated at the tumor site. The extensive analysis of the TME immune profile suggested a correlation between CDs-IND mediated antitumoral activity and enhanced immune response, involving recruitment of NK and NKT cells, associated with the reduced expression of IDO. Indeed, systemic administration of the nanosystem controlled tumor progression similarly to intratumoral administration, despite a more immunosuppressive microenvironment in which only NK, NKT, and IDO pathways were comparable with those detected in IT-treated mice. These findings indicate that the CDs-IND conjugate not only exerts direct antitumoral effects but also stimulates an immune response, validating the concept of combining nanomedicine with immunotherapy for breast cancer treatment. The encouraging results of CDs-IND treatments showing a significant control on tumor growth support the combination of

nanotheranostics and immunotherapy for breast cancer treatment, offering interesting alternatives to conventional treatments. Moreover, the efficacy of the therapeutic approach by systemic administration provides a versatile and less invasive alternative to surgical or localized treatments of metastatic breast cancers.

The incorporation of gold within the structure of CDs, obtained by introducing gold seeds among the molecular precursors of their solvothermal synthesis, yielded hybrid nanostructures of approximately 5 nm, exhibiting both fluorescence and CT contrast properties. Similarly, embedding Gd^{+3} ions within the carbonaceous core, by performing the solvothermal synthesis of CDs in the presence of gadolinium chloride, led to hybrid nanoparticles maintaining the photoluminescence of conventional CDs, and endowed with strong MRI contrast, that even overperforms the relaxivity of the clinical standard gadobutrol. Such nanostructures enable synergistic multimodal imaging of cells, potentially valuable in image-guided cancer theranostics, overcoming the drawbacks of FLI-based nanoprobes in vivo. Furthermore, embedding Gd^{+3} ions and gold nanoparticles within the carbonaceous structure provides a huge advantage over the conventional administration of these contrast agents, relieving the major concerns of their clinical application due to their potential toxicity. Both AuCDs and GdCDs demonstrated, indeed, plain cytocompatibility, corroborating the safe profile of these nanomaterials for biomedical purposes.

In addition, the imaging properties of GdCDs showed a pH sensitivity suitable for MRI monitoring of TME. Since pH increases in the TME correlate with tumor regression, obtaining real-time information of the TME conditions enables to adjust the treatment on the basis of the individual response, paving the way for personalized medicine

approaches. GdCDs also demonstrated strong photothermal conversion following exposure to NIR light (810 nm, 300 s, 5 W cm^{-2}), which causes a significant decrease in cell viability preferentially in cancer cells. Thereby, GdCDs can be remotely activated for on-demand killing cancer cells with minimal local side effects, demonstrating present inherent therapeutic efficacy. The potential of this unique nanomaterial could be exploited by proper surface engineering to develop sophisticated theranostic nanoplatforms for personalized multimodal image-guided anticancer approaches as well as TME sensing applications.

A possible functionalization strategy has been proposed for AuCDs, which were conjugated with PEG-glucose moieties to exploit the massive glucose demand of tumor cells, due to the Warburg effect, achieving a preferential delivery towards breast cancer. The tunable fluorescence of the AuCDs-Glu conjugate, conferred by AuCDs used as core element, enable to follow the nanosystem's cellular internalization without recurring to labeling with organic dyes, demonstrating significantly heightened glucose-dependent entry of the conjugate into cancer cells. These results validates the innovative use of glucose as a targeting agent for selectively directing nanoparticles towards cancer cells, while corroborating the considerable promise of the proposed nanosystem for a diverse array of precision anticancer theranostic applications, spanning diagnostic and therapeutic targets.

Although preliminary, the achievements of this thesis indicate the evident potential of CDs-based multifunctional nanoplatforms in breast cancer theranostics. Combining multiple therapeutic approaches with multi-modal imaging and biosensing, nano-theranostics provide unique opportunities for minimally invasive advanced precision

medicine approaches in breast cancer therapy, revolutionizing the current landscape of breast cancer management.

Future research should focus on further developments and clinical translation of carbon-based theranostic nanoplatforms, investigating the long-term stability and bio-compatibility of these nanotheranostics in more complex pre-clinical models, better resembling the complexity of TME, as well as exploring the application of these nanosystems in other types of cancer to further establish their broad-spectrum efficacy.

References

Abouelmagd, S. A., Hyun, H., & Yeo, Y. (2014). Extracellularly activatable nanocarriers for drug delivery to tumors. *Expert Opinion on Drug Delivery*, *11*(10), 1601. https://doi.org/10.1517/17425247.2014.930434

Adekola, K., Rosen, S. T., & Shanmugam, M. (2012). Glucose transporters in cancer metabolism. In *Current Opinion in Oncology* (Vol. 24, Issue 6, pp. 650–654). https://doi.org/10.1097/CCO.0b013e328356da72

Aghebati-Maleki, A., Dolati, S., Ahmadi, M., Baghbanzhadeh, A., Asadi, M., Fotouhi, A., Yousefi, M., & Aghebati-Maleki, L. (2020). Nanoparticles and cancer therapy: Perspectives for application of nanoparticles in the treatment of cancers. In *Journal of Cellular Physiology* (Vol. 235, Issue 3, pp. 1962–1972). Wiley-Liss Inc. https://doi.org/10.1002/jcp.29126

Al Omari, M. M., Zughul, M. B., Davies, J. E. D., & Badwan, A. A. (2006). Sildenafil/cyclodextrin complexation: stability constants, thermodynamics, and guest-host interactions probed by 1H NMR and molecular modeling studies. *Journal of Pharmaceutical and Biomedical Analysis*, *41*(3), 857–865. https://doi.org/10.1016/J.JPBA.2006.01.055

Attia, M. F., Anton, N., Wallyn, J., Omran, Z., & Vandamme, T. F. (2019). An overview of active and passive targeting strategies to improve the nanocarriers efficiency to tumour sites. *The Journal of Pharmacy and Pharmacology*, *71*(8), 1185–1198. https://doi.org/10.1111/JPHP.13098

Balou, S., Shandilya, P., & Priye, A. (2022). Carbon dots for photothermal applications. *Frontiers in Chemistry*, *10*, 1298. https://doi.org/10.3389/FCHEM.2022.1023602/BIBTEX

Banerjee, D., & Sengupta, S. (2011). Nanoparticles in Cancer Chemotherapy. *Progress in Molecular Biology and Translational Science*, *104*, 489–507. https://doi.org/10.1016/B978-0-12-416020-0.00012-7

Bartkowski, M., Zhou, Y., Nabil Amin Mustafa, M., Eustace, A. J., & Giordani, S. (2024). CARBON DOTS: Bioimaging and Anticancer Drug Delivery. *Chemistry – A European Journal*, *30*(19), e202303982. https://doi.org/10.1002/CHEM.202303982

Beik, J., Abed, Z., Ghoreishi, F. S., Hosseini-Nami, S., Mehrzadi, S., Shakeri-Zadeh, A., & Kamrava, S. K. (2016). Nanotechnology in hyperthermia cancer therapy: From fundamental principles to advanced applications. *Journal of Controlled Release*, *235*, 205–221. https://doi.org/10.1016/J.JCONREL.2016.05.062

Bettaieb, A., Wrzal, P. K., Averill-Bates, D. A., Bettaieb, A., Wrzal, P. K., & Averill-Bates, D. A. (2013). Hyperthermia: Cancer Treatment and Beyond. *Cancer Treatment - Conventional and Innovative Approaches*. https://doi.org/10.5772/55795

Bhattacharjee, S. (2021). Understanding the Burst Release Phenomenon: Toward Designing Effective Nanoparticulate Drug-Delivery Systems. *Therapeutic Delivery*, *12*(1), 21–36. https://doi.org/10.4155/TDE-2020-0099

Bray Bsc, F., Laversanne, | Mathieu, Hyuna, |, Phd, S., Ferlay, J., Siegel Mph, R. L., Soerjomataram, I., Ahmedin, |, & Dvm, J. (2024). Global cancer statistics 2022: GLOBOCAN estimates of incidence and mortality worldwide for 36 cancers in 185 countries. *CA: A Cancer Journal for Clinicians*, *74*(3), 229–263. https://doi.org/10.3322/CAAC.21834

Brincks, E. L., Adams, J., Wang, L., Turner, B., Marcinowicz, A., Ke, J., Essmann, M., Mautino, L. M., Allen, C. Van, Kumar, S., Vahanian, N., Link, C., & Mautino, M. R. (2020). Indoximod opposes the immunosuppressive effects mediated by IDO and TDO via modulation of AhR function and activation of mTORC1. In *Oncotarget* (Vol. 11, Issue 25). www.oncotarget.com

Brown, S. R., & Vomhof-DeKrey, E. E. (2024). Current Immunotherapy Treatments of Primary Breast Cancer Subtypes. *Biomedicines 2024, Vol. 12, Page 895*, *12*(4), 895. https://doi.org/10.3390/BIOMEDICINES12040895

Bukowski, K., Kciuk, M., & Kontek, R. (2020). Mechanisms of Multidrug Resistance in Cancer Chemotherapy. *International Journal of Molecular Sciences 2020, Vol. 21, Page 3233*, *21*(9), 3233. https://doi.org/10.3390/IJMS21093233

Burguin, A., Diorio, C., & Durocher, F. (2021). Breast Cancer Treatments: Updates and New Challenges. *Journal of Personalized Medicine 2021, Vol. 11, Page 808*, *11*(8), 808. https://doi.org/10.3390/JPM11080808

Caspani, S., Magalhães, R., Araújo, J. P., & Sousa, C. T. (2020). Magnetic Nanomaterials as Contrast Agents for MRI. *Materials 2020, Vol. 13, Page 2586*, *13*(11), 2586. https://doi.org/10.3390/MA13112586

Chicheł, A., Skowronek, J., Kubaszewska, M., & Kanikowski, M. (2007). Hyperthermia – description of a method and a review of clinical applications. *Reports of Practical Oncology & Radiotherapy*, *12*(5), 267–275. https://doi.org/10.1016/S1507-1367(10)60065-X

Chun, B. M., Page, D. B., & McArthur, H. L. (2019). Combination Immunotherapy Strategies in Breast Cancer. *Current Breast Cancer Reports*, *11*(4), 228–240. https://doi.org/10.1007/S12609-019-00333-3/TABLES/3

Claessens, A. K. M., Ibragimova, K. I. E., Geurts, S. M. E., Bos, M. E. M. M., Erdkamp, F. L. G., & Tjan-Heijnen, V. C. G. (2020). The role of chemotherapy in treatment of advanced breast cancer: an overview for clinical practice. *Critical Reviews in Oncology/Hematology*, *153*, 102988. https://doi.org/10.1016/J.CRITREVONC.2020.102988

Corrie, P. G. (2011). Cytotoxic chemotherapy: Clinical aspects. In *Medicine* (Vol. 39, Issue 12, pp. 717–722). Elsevier Ltd. https://doi.org/10.1016/j.mpmed.2011.09.012

Cortesi, L., Rugo, H. S., & Jackisch, C. (2021). An Overview of PARP Inhibitors for the Treatment of Breast Cancer. *Targeted Oncology*, *16*(3), 255. https://doi.org/10.1007/S11523-021-00796-4

Cutrone, G., Casas-Solvas, J. M., & Vargas-Berenguel, A. (2017). Cyclodextrin-Modified inorganic materials for the construction of nanocarriers. *International Journal of Pharmaceutics*, *531*(2), 621–639. https://doi.org/10.1016/j.ijpharm.2017.06.080

Danhier, F. (2016). To exploit the tumor microenvironment: Since the EPR effect fails in the clinic, what is the future of nanomedicine? *Journal of Controlled Release*, *244*, 108–121. https://doi.org/10.1016/J.JCONREL.2016.11.015

Debien, V., De Caluwé, A., Wang, X., Piccart-Gebhart, M., Tuohy, V. K., Romano, E., & Buisseret, L. (2023). Immunotherapy in breast cancer: an overview of current strategies and perspectives. *Npj Breast Cancer 2023 9:1*, *9*(1), 1–10. https://doi.org/10.1038/s41523-023-00508-3

Decuzzi, P., & Cook, A. B. (2021). Harnessing Endogenous Stimuli for Responsive Materials in Theranostics. *ACS Nano*, *15*(2), 2068. https://doi.org/10.1021/ACSNANO.0C09115

Della Chiesa, M., Carlomagno, S., Frumento, G., Balsamo, M., Cantoni, C., Conte, R., Moretta, L., Moretta, A., & Vitale, M. (2006). The tryptophan catabolite l-kynurenine inhibits the surface expression of NKp46- and NKG2D-activating receptors and regulates NK-cell function. *Blood*, *108*(13), 4118–4125. https://doi.org/10.1182/BLOOD-2006-03-006700

Dieci, M. V., Miglietta, F., & Guarneri, V. (2021). Immune Infiltrates in Breast Cancer: Recent Updates and Clinical Implications. *Cells*, *10*(2), 1–27. https://doi.org/10.3390/CELLS10020223

Djedaini-Pilard, F., Gosnat, M., Steinbruckner, S., Dalbiez, J. P., Crini, G., Perly, B., & Gadelle, A. (1999). Mono-6-Tosyl-ß-Cyclodextrin: Preparation, Hydrolysis and Self-Inclusion Studies in Aqueous Solution. *Proceedings of the Ninth*

International Symposium on Cyclodextrins, 73–76. https://doi.org/10.1007/978-94-011-4681-4_16

Dos, P., Menezes, P., De, T., Andrade, A., Frank, A., Barros, E. P., Soares De Souza, S., Das, G., Gomes Trindade, G., Araújo, I., Trindade, S., Russo Serafini, M., Guterres, S. S., & Antunes De Souza Araújo, A. (2019). *Advances of nanosystems containing cyclodextrins and their applications in pharmaceuticals*. https://doi.org/10.1016/j.ijpharm.2019.01.041

Du, B., Jiang, X., Das, A., Zhou, Q., Yu, M., Jin, R., & Zheng, J. (2017). Glomerular Barrier Behaves As an Atomically Precise Bandpass Filter in a Sub-nanometer Regime. *Nature Nanotechnology*, *12*(11), 1096. https://doi.org/10.1038/NNANO.2017.170

Dunne, M., Regenold, M., & Allen, C. (2020). Hyperthermia can alter tumor physiology and improve chemo- and radio-therapy efficacy. *Advanced Drug Delivery Reviews*, *163–164*, 98–124. https://doi.org/10.1016/J.ADDR.2020.07.007

Ernsting, M. J., Murakami, M., Roy, A., & Li, S. D. (2013). Factors controlling the pharmacokinetics, biodistribution and intratumoral penetration of nanoparticles. In *Journal of Controlled Release* (Vol. 172, Issue 3, pp. 782–794). Elsevier. https://doi.org/10.1016/j.jconrel.2013.09.013

Espina-Casado, J., Fontanil, T., Fernández-González, A., Cal, S., Obaya, Á. J., Díaz-García, M. E., & Badía-Laíño, R. (2021). Carbon dots as multifunctional platform for intracellular pH sensing and bioimaging. In vitro and in vivo studies. *Sensors*

and Actuators B: Chemical, *346*, 130555. https://doi.org/10.1016/J.SNB.2021.130555

Evans, R. A. (2007). The rise of azide-alkyne 1,3-Dipolar 'click' cycloaddition and its application to polymer science and surface modification. In *Australian Journal of Chemistry* (Vol. 60, Issue 6, pp. 384–395). CSIRO PUBLISHING. https://doi.org/10.1071/CH06457

Fam, S. Y., Chee, C. F., Yong, C. Y., Ho, K. L., Mariatulqabtiah, A. R., & Tan, W. S. (2020). Stealth Coating of Nanoparticles in Drug-Delivery Systems. *Nanomaterials*, *10*(4), 787. https://doi.org/10.3390/nano10040787

Feng, T., Tao, S., Yue, D., Zeng, Q., Chen, W., Yang, B., Feng, T., Tao, S., Yue, D., Zeng, Q., Yang, B., & Chen, W. (2020). Recent Advances in Energy Conversion Applications of Carbon Dots: From Optoelectronic Devices to Electrocatalysis. *Small*, *16*(31), 2001295. https://doi.org/10.1002/SMLL.202001295

Figueroa-Magalhães, M. C., Jelovac, D., Connolly, R. M., & Wolff, A. C. (2014). Treatment of HER2-positive breast cancer. *The Breast*, *23*(2), 128–136. https://doi.org/10.1016/J.BREAST.2013.11.011

Fox, E., Oliver, T., Rowe, M., Thomas, S., Zakharia, Y., Gilman, P. B., Muller, A. J., & Prendergast, G. C. (2018). Indoximod: An immunometabolic adjuvant that empowers T cell activity in cancer. *Frontiers in Oncology*, *8*(SEP), 413467. https://doi.org/10.3389/FONC.2018.00370/BIBTEX

Fraguas-Sánchez, A. I., Martín-Sabroso, C., Fernández-Carballido, A., & Torres-Suárez, A. I. (2019). Current status of nanomedicine in the chemotherapy of breast cancer. *Cancer Chemotherapy and Pharmacology 2019 84:4*, *84*(4), 689–706. https://doi.org/10.1007/S00280-019-03910-6

Frumento, G., Rotondo, R., Tonetti, M., Damonte, G., Benatti, U., & Ferrara, G. B. (2002). Tryptophan-derived Catabolites Are Responsible for Inhibition of T and Natural Killer Cell Proliferation Induced by Indoleamine 2,3-Dioxygenase. *The Journal of Experimental Medicine*, *196*(4), 459. https://doi.org/10.1084/JEM.20020121

Funkhouser, J. (2002). Reinventing pharma: The theranostic revolution. *Current Drug Discovery*, *AUG.*, 17–19.

Glassman, P. M., & Muzykantov, V. R. (2019). Pharmacokinetic and Pharmacodynamic Properties of Drug Delivery Systems. *The Journal of Pharmacology and Experimental Therapeutics*, *370*(3), 570. https://doi.org/10.1124/JPET.119.257113

Goel, S., Ferreira, C. A., Dogra, P., Yu, B., Kutyreff, C. J., Siamof, C. M., Engle, J. W., Barnhart, T. E., Cristini, V., Wang, Z., & Cai, W. (2019). Size-optimized Ultrasmall Porous Silica Nanoparticles Depict Vasculature-based Differential Targeting in Triple Negative Breast Cancer. *Small (Weinheim an Der Bergstrasse, Germany)*, *15*(46), e1903747. https://doi.org/10.1002/SMLL.201903747

Goryacheva, I. Y., Sapelkin, A. V., & Sukhorukov, G. B. (2017). Carbon nanodots: Mechanisms of photoluminescence and principles of application. In *TrAC - Trends in Analytical Chemistry* (Vol. 90, pp. 27–37). Elsevier B.V. https://doi.org/10.1016/j.trac.2017.02.012

Gote, V., Nookala, A. R., Bolla, P. K., & Pal, D. (2021). Drug Resistance in Metastatic Breast Cancer: Tumor Targeted Nanomedicine to the Rescue. *International Journal of Molecular Sciences 2021, Vol. 22, Page 4673*, *22*(9), 4673. https://doi.org/10.3390/IJMS22094673

Guo, J., Zeng, H., & Chen, Y. (2020). Emerging Nano Drug Delivery Systems Targeting Cancer-Associated Fibroblasts for Improved Antitumor Effect and Tumor Drug Penetration. *Molecular Pharmaceutics*, *17*(4), 1028–1048. https://doi.org/10.1021/ACS.MOLPHARMACEUT.0C00014/ASSET/IMAGES/LARGE/MP0C00014_0009.JPEG

Guo, S., Burcus, N. I., Scott, M., Jing, Y., & Semenov, I. (2021). The role of reactive oxygen species in the immunity induced by nano-pulse stimulation. *Scientific Reports 2021 11:1*, *11*(1), 1–13. https://doi.org/10.1038/s41598-021-03342-4

Hanahan, D., & Coussens, L. M. (2012). Accessories to the Crime: Functions of Cells Recruited to the Tumor Microenvironment. *Cancer Cell*, *21*(3), 309–322. https://doi.org/10.1016/J.CCR.2012.02.022

He, H., Liu, L., Morin, E. E., Liu, M., & Schwendeman, A. (2019). Survey of Clinical Translation of Cancer Nanomedicines - Lessons Learned from Successes and Failures. *Accounts of Chemical Research*, *52*(9), 2673–2683.

https://doi.org/10.1021/ACS.ACCOUNTS.9B00228/ASSET/IMAGES/MEDIUM/AR9B00228_0007.GIF

Hola, K., Zhang, Y., Wang, Y., Giannelis, E. P., Zboril, R., & Rogach, A. L. (2014). Carbon dots - Emerging light emitters for bioimaging, cancer therapy and optoelectronics. In *Nano Today* (Vol. 9, Issue 5, pp. 590–603). Elsevier B.V. https://doi.org/10.1016/j.nantod.2014.09.004

Huang, J., Zhang, L., Wan, D., Zhou, L., Zheng, S., Lin, S., & Qiao, Y. (2021). Extracellular matrix and its therapeutic potential for cancer treatment. *Signal Transduction and Targeted Therapy 2021 6:1*, *6*(1), 1–24. https://doi.org/10.1038/s41392-021-00544-0

Hussein, Y. H. A., & Youssry, M. (2018). Polymeric Micelles of Biodegradable Diblock Copolymers: Enhanced Encapsulation of Hydrophobic Drugs. *Materials 2018, Vol. 11, Page 688*, *11*(5), 688. https://doi.org/10.3390/MA11050688

Insua-Rodríguez, J., & Oskarsson, T. (2016). The extracellular matrix in breast cancer. *Advanced Drug Delivery Reviews*, *97*, 41–55. https://doi.org/10.1016/J.ADDR.2015.12.017

Jackson, E., Dees, E. C., Kauh, J. S., Harvey, R. D., Neuger, A., Lush, R., Antonia, S. J., Minton, S. E., Ismail-Khan, R., Han, H. S., Vahanian, N. N., Ramsey, W. J., Link, C. J., Streicher, H., Sullivan, D., & Soliman, H. H. (2013). A phase I study of indoximod in combination with docetaxel in metastatic solid tumors. *Https://Doi.Org/10.1200/Jco.2013.31.15_suppl.3026*, *31*(15_suppl), 3026–3026. https://doi.org/10.1200/JCO.2013.31.15_SUPPL.3026

Jha, S., Sharma, P. K., & Malviya, R. (2016). Hyperthermia: Role and Risk Factor for Cancer Treatment. *Achievements in the Life Sciences*, *10*(2), 161–167. https://doi.org/10.1016/J.ALS.2016.11.004

Jia, Q., Zhao, Z., Liang, K., Nan, F., Li, Y., Wang, J., Ge, J., & Wang, P. (2020). Recent advances and prospects of carbon dots in cancer nanotheranostics. In *Materials Chemistry Frontiers* (Vol. 4, Issue 2, pp. 449–471). Royal Society of Chemistry. https://doi.org/10.1039/c9qm00667b

Jiang, X., Xin, H., Ren, Q., Gu, J., Zhu, L., Du, F., Feng, C., Xie, Y., Sha, X., & Fang, X. (2014). Nanoparticles of 2-deoxy-d-glucose functionalized poly(ethylene glycol)-co-poly(trimethylene carbonate) for dual-targeted drug delivery in glioma treatment. *Biomaterials*, *35*(1), 518–529. https://doi.org/10.1016/J.BIOMATERIALS.2013.09.094

Jiang, Y., Jiang, Z., Wang, M., & Ma, L. (2022). Current understandings and clinical translation of nanomedicines for breast cancer therapy. *Advanced Drug Delivery Reviews*, *180*, 114034. https://doi.org/10.1016/J.ADDR.2021.114034

Jing, R., Bai, S., Zhang, P., Ren, H., Jia, L., Li, W., & Zheng, G. (2024). IDO-1 impairs antitumor immunity of natural killer cells in triple-negative breast cancer via up-regulation of HLA-G. *Breast Cancer*, *31*(1), 135–147. https://doi.org/10.1007/S12282-023-01522-W/FIGURES/6

Joshi, H., & Press, M. F. (2018). Molecular Oncology of Breast Cancer. *The Breast: Comprehensive Management of Benign and Malignant Diseases*, 282-307.e5. https://doi.org/10.1016/B978-0-323-35955-9.00022-2

Jung, Y. K., Choi, Y., & Kim, B.-S. (2016). Functionalized Carbon Nanodots for Biomedical Applications. In *Springer Series in Biomaterials Science and Engineering* (Vol. 5, pp. 299–317). Springer International Publishing Switzerland. https://doi.org/10.1007/978-3-319-22861-7_10

Kadam, R. S., Bourne, D. W. A., & Kompella, U. B. (2012). Nano-Advantage in Enhanced Drug Delivery with Biodegradable Nanoparticles: Contribution of Reduced Clearance. *Drug Metabolism and Disposition*, *40*(7), 1380. https://doi.org/10.1124/DMD.112.044925

Kaminskas, L. M., & Boyd, B. J. (2011). *Nanosized Drug Delivery Vectors and the Reticuloendothelial System*. 155–178. https://doi.org/10.1007/978-94-007-1248-5_6

Kasal, P., & Jindřich, J. (2021). Mono-6-Substituted Cyclodextrins—Synthesis and Applications. *Molecules 2021, Vol. 26, Page 5065*, *26*(16), 5065. https://doi.org/10.3390/MOLECULES26165065

Kaurav, H., Verma, D., Bansal, A., Kapoor, D. N., & Sheth, S. (2023). Progress in drug delivery and diagnostic applications of carbon dots: a systematic review. *Frontiers in Chemistry*, *11*. https://doi.org/10.3389/FCHEM.2023.1227843

Kelkar, S. S., & Reineke, T. M. (2011). *Theranostics: Combining Imaging and Therapy*. *22*, 1879–1903. https://doi.org/10.1021/bc200151q

Key, J., & Leary, J. F. (2014). Nanoparticles for multimodal in vivo imaging in nanomedicine. *International Journal of Nanomedicine*, *9*(1), 711. https://doi.org/10.2147/IJN.S53717

Krysko, D. V., Garg, A. D., Kaczmarek, A., Krysko, O., Agostinis, P., & Vandenabeele, P. (2012). Immunogenic cell death and DAMPs in cancer therapy. *Nature Reviews Cancer 2012 12:12*, *12*(12), 860–875. https://doi.org/10.1038/nrc3380

Lassche, G., Crezee, J., & Van Herpen, C. M. L. (2019). *Whole-body hyperthermia in combination with systemic therapy in advanced solid malignancies*. https://doi.org/10.1016/j.critrevonc.2019.04.023

Lecroy, G. E., Messina, F., Sciortino, A., Bunker, C. E., Wang, P., Fernando, K. A. S., & Sun, Y. P. (2017). Characteristic Excitation Wavelength Dependence of Fluorescence Emissions in Carbon ‘quantum’ Dots. *Journal of Physical Chemistry C*, *121*(50), 28180–28186. https://doi.org/10.1021/acs.jpcc.7b10129

Lee, J. H., & Yeo, Y. (2015). Controlled drug release from pharmaceutical nanocarriers. *Chemical Engineering Science*, *125*, 75–84. https://doi.org/10.1016/J.CES.2014.08.046

Li, J., Goh, E. L. K., He, J., Li, Y., Fan, Z., Yu, Z., Yuan, P., & Liu, D. X. (2023). Emerging Intrinsic Therapeutic Targets for Metastatic Breast Cancer. *Biology 2023, Vol. 12, Page 697*, *12*(5), 697. https://doi.org/10.3390/BIOLOGY12050697

Li, L., Tan, J., Miao, Y., Lei, P., & Zhang, Q. (2015). ROS and Autophagy: Interactions and Molecular Regulatory Mechanisms. *Cellular and Molecular Neurobiology*, *35*(5), 615–621. https://doi.org/10.1007/S10571-015-0166-X/FIGURES/1

Li, W., & Chen, X. (2015). Gold nanoparticles for photoacoustic imaging. *Nanomedicine (London, England)*, *10*(2), 299. https://doi.org/10.2217/NNM.14.169

Li, X., Wu, M., Pan, L., & Shi, J. (2015). Tumor vascular-targeted co-delivery of anti-angiogenesis and chemotherapeutic agents by mesoporous silica nanoparticle-based drug delivery system for synergetic therapy of tumor. *International Journal of Nanomedicine*, *11*, 93–105. https://doi.org/10.2147/IJN.S81156

Liberti, M. V., & Locasale, J. W. (2016). The Warburg Effect: How Does it Benefit Cancer Cells? In *Trends in Biochemical Sciences* (Vol. 41, Issue 3, pp. 211–218). Elsevier Ltd. https://doi.org/10.1016/j.tibs.2015.12.001

Lim, E. K., Kim, T., Paik, S., Haam, S., Huh, Y. M., & Lee, K. (2015). Nanomaterials for theranostics: Recent advances and future challenges. In *Chemical Reviews* (Vol. 115, Issue 1, pp. 327–394). American Chemical Society. https://doi.org/10.1021/cr300213b

Lim, S. Y., Shen, W., & Gao, Z. (2015). Carbon quantum dots and their applications. In *Chemical Society Reviews* (Vol. 44, Issue 1, pp. 362–381). Royal Society of Chemistry. https://doi.org/10.1039/c4cs00269e

Liu, H., Zhong, X., Pan, Q., Zhang, Y., Deng, W., Zou, G., Hou, H., & Ji, X. (2024). A review of carbon dots in synthesis strategy. *Coordination Chemistry Reviews*, *498*, 215468. https://doi.org/10.1016/J.CCR.2023.215468

Liu, M., Du, H., Zhang, W., & Zhai, G. (2017). Internal stimuli-responsive nanocarriers for drug delivery: Design strategies and applications. In *Materials Science and Engineering C* (Vol. 71, pp. 1267–1280). Elsevier Ltd. https://doi.org/10.1016/j.msec.2016.11.030

Liu, W., Li, C., Ren, Y., Sun, X., Pan, W., Li, Y., Wang, J., & Wang, W. (2016). Carbon dots: surface engineering and applications. *Journal of Materials Chemistry B*, *4*(35), 5772–5788. https://doi.org/10.1039/C6TB00976J

Liu, X., Li, L., Si, F., Huang, L., Zhao, Y., Zhang, C., Hoft, D. F., & Peng, G. (2021). NK and NKT cells have distinct properties and functions in cancer. *Oncogene*, *40*(27), 4521–4537. https://doi.org/10.1038/S41388-021-01880-9

Lopez-Tarruella, S., Echavarria, I., Jerez, Y., Herrero, B., Gamez, S., & Martin, M. (2022). How we Treat HR-Positive, HER2-Negative Early Breast Cancer. *Future Oncology*, *18*(8), 1003–1022. https://doi.org/10.2217/FON-2021-0668

Lu, H., Wang, J., Wang, T., Zhong, J., Bao, Y., & Hao, H. (2016). Recent Progress on Nanostructures for Drug Delivery Applications. *Journal of Nanomaterials*, *2016*(1), 5762431. https://doi.org/10.1155/2016/5762431

Luque-Bolivar, A., Pérez-Mora, E., Villegas, V. E., & Rondón-Lagos, M. (2020). Resistance and Overcoming Resistance in Breast Cancer. *Breast Cancer : Targets and Therapy*, *12*, 211. https://doi.org/10.2147/BCTT.S270799

Lv, Z., He, S., Wang, Y., & Zhu, X. (2021). Noble Metal Nanomaterials for NIR-Triggered Photothermal Therapy in Cancer. *Advanced Healthcare Materials*, *10*(6), 2001806. https://doi.org/10.1002/ADHM.202001806

Mao, X. J., Zheng, H. Z., Long, Y. J., Du, J., Hao, J. Y., Wang, L. L., & Zhou, D. B. (2010). Study on the fluorescence characteristics of carbon dots. *Spectrochimica Acta - Part A: Molecular and Biomolecular Spectroscopy*, *75*(2), 553–557. https://doi.org/10.1016/j.saa.2009.11.015

Marçais, A., Cherfils-Vicini, J., Viant, C., Degouve, S., Viel, S., Fenis, A., Rabilloud, J., Mayol, K., Tavares, A., Bienvenu, J., Gangloff, Y. G., Gilson, E., Vivier, E., & Walzer, T. (2014). The metabolic checkpoint kinase mTOR is essential for IL-15 signaling during the development and activation of NK cells. *Nature Immunology 2014 15:8*, *15*(8), 749–757. https://doi.org/10.1038/ni.2936

Mattheolabakis, G., Rigas, B., & Constantinides, P. P. (2012). Nanodelivery strategies in cancer chemotherapy: biological rationale and pharmaceutical perspectives. *Nanomedicine (London, England)*, *7*(10), 1577–1590. https://doi.org/10.2217/NNM.12.128

Mauro, N., Calabrese, G., Sciortino, A., Rizzo, M. G., Messina, F., Giammona, G., & Cavallaro, G. (2024). Microporous Fluorescent Poly(D,L-lactide) Acid–Carbon

Nanodot Scaffolds for Bone Tissue Engineering Applications. *Materials*, *17*(2). https://doi.org/10.3390/ma17020449

Mauro, N., Scialabba, C., Agnello, S., Cavallaro, G., & Giammona, G. (2020). Folic acid-functionalized graphene oxide nanosheets via plasma etching as a platform to combine NIR anticancer phototherapy and targeted drug delivery. *Materials Science and Engineering: C*, *107*, 110201. https://doi.org/10.1016/J.MSEC.2019.110201

Mauro, N., Utzeri, M. A., Buscarino, G., Sciortino, A., Messina, F., Cavallaro, G., & Giammona, G. (2020). Pressure-Dependent Tuning of Photoluminescence and Size Distribution of Carbon Nanodots for Theranostic Anticancer Applications. *Materials 2020, Vol. 13, Page 4899*, *13*(21), 4899. https://doi.org/10.3390/MA13214899

Mauro, N., Utzeri, M. A., Cillari, R., Scialabba, C., Giammona, G., & Cavallaro, G. (2022). Cholesterol-Inulin Conjugates for Efficient SN38 Nuclear Delivery: Nanomedicines for Precision Cancer Therapy. *Cancers*, *14*(19). https://doi.org/10.3390/cancers14194857

Mauro, N., Utzeri, M. A., Sciortino, A., Messina, F., Cannas, M., Popescu, R., Gerthsen, D., Buscarino, G., Cavallaro, G., & Giammona, G. (2022). Decagram-Scale Synthesis of Multicolor Carbon Nanodots: Self-Tracking Nanoheaters with Inherent and Selective Anticancer Properties. *ACS Applied Materials and Interfaces*, *14*(2), 2551–2563.

https://doi.org/10.1021/ACSAMI.1C19599/ASSET/IMAGES/LARGE/AM1C19599_0006.JPEG

Mauro, N., Utzeri, M. A., Varvarà, P., & Cavallaro, G. (2021). *molecules Functionalization of Metal and Carbon Nanoparticles with Potential in Cancer Theranostics*. https://doi.org/10.3390/molecules26113085

Mavratzas, A., Seitz, J., Smetanay, K., Schneeweiss, A., Jäger, D., & Fremd, C. (2020). Atezolizumab for use in PD-L1-positive unresectable, locally advanced or metastatic triple-negative breast cancer. *Future Oncology*, *16*(3), 4439–4453. https://doi.org/10.2217/FON-2019-0468

Mellal, I., Oukaira, A., Kengene, E., & Lakhssassi, A. (2017). Thermal Therapy Modalities for Cancer Treatment: A Review and Future Perspectives. *International Journal of Applied Science - Research and Review*, *04*(02). https://doi.org/10.21767/2394-9988.100064

Messina, F., Sciortino, L., Popescu, R., Venezia, A. M., Sciortino, A., Buscarino, G., Agnello, S., Schneider, R., Gerthsen, D., Cannas, M., & Gelardi, F. M. (2016). Fluorescent nitrogen-rich carbon nanodots with an unexpected β-C3N4 nanocrystalline structure. *Journal of Materials Chemistry C*, *4*(13), 2598–2605. https://doi.org/10.1039/C5TC04096E

Mishra, V., Patil, A., Thakur, S., & Kesharwani, P. (2018). Carbon dots: emerging theranostic nanoarchitectures. *Drug Discovery Today*, *23*(6), 1219–1232. https://doi.org/10.1016/J.DRUDIS.2018.01.006

Mitchell, M. J., Billingsley, M. M., Haley, R. M., Wechsler, M. E., Peppas, N. A., & Langer, R. (2020). Engineering precision nanoparticles for drug delivery. *Nature Reviews Drug Discovery 2020 20:2*, *20*(2), 101–124. https://doi.org/10.1038/s41573-020-0090-8

Miteva, M., Kirkbride, K. C., Kilchrist, K. V., Werfel, T. A., Li, H., Nelson, C. E., Gupta, M. K., Giorgio, T. D., & Duvall, C. L. (2015). Tuning PEGylation of mixed micelles to overcome intracellular and systemic siRNA delivery barriers. *Biomaterials*, *38*, 97–107. https://doi.org/10.1016/J.BIOMATERIALS.2014.10.036

Moorthi, C., Manavalan, R., & Kathiresan, K. (2011). Nanotherapeutics to overcome conventional cancer chemotherapy limitations. In *Journal of Pharmacy and Pharmaceutical Sciences* (Vol. 14, Issue 1, pp. 67–77). Canadian Society for Pharmaceutical Sciences. https://doi.org/10.18433/j30c7d

Morais, M., Machado, V., Dias, F., Figueiredo, P., Palmeira, C., Martins, G., Fernandes, R., Malheiro, A. R., Mikkonen, K. S., Teixeira, A. L., & Medeiros, R. (2022). Glucose-Functionalized Silver Nanoparticles as a Potential New Therapy Agent Targeting Hormone-Resistant Prostate Cancer cells. *International Journal of Nanomedicine*, *17*, 4321. https://doi.org/10.2147/IJN.S364862

Mura, S., Nicolas, J., & Couvreur, P. (2013). Stimuli-responsive nanocarriers for drug delivery. In *Nature Materials* (Vol. 12, Issue 11, pp. 991–1003). Nature Publishing Group. https://doi.org/10.1038/nmat3776

Najafi, M., Goradel, N. H., Farhood, B., Salehi, E., Solhjoo, S., Toolee, H., Kharazinejad, E., & Mortezaee, K. (2019). Tumor microenvironment: Interactions and therapy. In *Journal of Cellular Physiology* (Vol. 234, Issue 5, pp. 5700–5721). Wiley-Liss Inc. https://doi.org/10.1002/jcp.27425

Nandi, U., Onyesom, I., & Douroumis, D. (2021). Transferrin conjugated Stealth liposomes for sirolimus active targeting in breast cancer. *Journal of Drug Delivery Science and Technology*, *66*, 102900. https://doi.org/10.1016/J.JDDST.2021.102900

Navarro, C., Ortega, Á., Santeliz, R., Garrido, B., Chacín, M., Galban, N., Vera, I., De Sanctis, J. B., & Bermúdez, V. (2022). Metabolic Reprogramming in Cancer Cells: Emerging Molecular Mechanisms and Novel Therapeutic Approaches. In *Pharmaceutics* (Vol. 14, Issue 6). MDPI. https://doi.org/10.3390/pharmaceutics14061303

Nazri, N. A. A., Azeman, N. H., Luo, Y., & A Bakar, A. A. (2021). Carbon quantum dots for optical sensor applications: A review. *Optics & Laser Technology*, *139*, 106928. https://doi.org/10.1016/J.OPTLASTEC.2021.106928

Owens, D. E., & Peppas, N. A. (2006). Opsonization, biodistribution, and pharmacokinetics of polymeric nanoparticles. In *International Journal of Pharmaceutics* (Vol. 307, Issue 1, pp. 93–102). Elsevier. https://doi.org/10.1016/j.ijpharm.2005.10.010

Paci, E., Broeders, M., Hofvind, S., Puliti, D., & Duffy, S. W. (2014). European Breast Cancer Service Screening Outcomes: A First Balance Sheet of the Benefits and

Harms. *Cancer Epidemiology, Biomarkers & Prevention*, *23*(7), 1159–1163. https://doi.org/10.1158/1055-9965.EPI-13-0320

Park, J. H., Lee, S., Kim, J. H., Park, K., Kim, K., & Kwon, I. C. (2008). Polymeric nanomedicine for cancer therapy. In *Progress in Polymer Science (Oxford)* (Vol. 33, Issue 1, pp. 113–137). Pergamon. https://doi.org/10.1016/j.progpolymsci.2007.09.003

Park, Y., Yoo, J., Lim, B., Kwon, W., & Rhee, S. W. (2016). Improving the functionality of carbon nanodots: Doping and surface functionalization. In *Journal of Materials Chemistry A* (Vol. 4, Issue 30, pp. 11582–11603). Royal Society of Chemistry. https://doi.org/10.1039/c6ta04813g

Pasquini, L., Napolitano, A., Visconti, E., Longo, D., Romano, A., Tomà, P., & Espagnet, M. C. R. (2018). Gadolinium-Based Contrast Agent-Related Toxicities. *CNS Drugs*, *32*(3), 229–240. https://doi.org/10.1007/S40263-018-0500-1

Patel, J. K., & Patel, A. P. (2019). Passive Targeting of Nanoparticles to Cancer. In *Surface Modification of Nanoparticles for Targeted Drug Delivery* (pp. 125–143). Springer International Publishing. https://doi.org/10.1007/978-3-030-06115-9_6

Phan, L. M. T., & Cho, S. (2022). Fluorescent Carbon Dot-Supported Imaging-Based Biomedicine: A Comprehensive Review. *Bioinorganic Chemistry and Applications*, *2022*. https://doi.org/10.1155/2022/9303703

Portale, F., & Di Mitri, D. (2023). NK Cells in Cancer: Mechanisms of Dysfunction and Therapeutic Potential. *International Journal of Molecular Sciences*, *24*(11), 9521. https://doi.org/10.3390/IJMS24119521

Prabhakar, U., Maeda, H., K. Jain, R., Sevick-Muraca, E. M., Zamboni, W., Farokhzad, O. C., Barry, S. T., Gabizon, A., Grodzinski, P., & Blakey, D. C. (2013). Challenges and key considerations of the enhanced permeability and retention effect for nanomedicine drug delivery in oncology. *Cancer Research*, *73*(8), 2412–2417. https://doi.org/10.1158/0008-5472.CAN-12-4561

Pusztai, L., Karn, T., Safonov, A., Abu-Khalaf, M. M., & Bianchini, G. (2016). New strategies in breast cancer: Immunotherapy. *Clinical Cancer Research*, *22*(9), 2105–2110. https://doi.org/10.1158/1078-0432.CCR-15-1315/268051/AM/NEW-STRATEGIES-IN-BREAST-CANCER

Rao, J., Dragulescu-Andrasi, A., & Yao, H. (2007). Fluorescence imaging in vivo: recent advances. *Current Opinion in Biotechnology*, *18*(1), 17–25. https://doi.org/10.1016/J.COPBIO.2007.01.003

Rezaeifard, S., Talei, A., Shariat, M., & Erfani, N. (2021). Tumor infiltrating NK cell (TINK) subsets and functional molecules in patients with breast cancer. *Molecular Immunology*, *136*, 161–167. https://doi.org/10.1016/J.MOLIMM.2021.03.003

Rizwanullah, M., Ahmad, M. Z., Ghoneim, M. M., Alshehri, S., Imam, S. S., Md, S., Alhakamy, N. A., Jain, K., & Ahmad, J. (2021). Receptor-Mediated Targeted Delivery of Surface-ModifiedNanomedicine in Breast Cancer: Recent Update

and Challenges. *Pharmaceutics*, *13*(12), 2039. https://doi.org/10.3390/PHARMACEUTICS13122039

Roberti, M. P., Mordoh, J., & Levy, E. M. (2012). Biological role of NK cells and immunotherapeutic approaches in breast cancer. *Frontiers in Immunology*, *3*(DEC), 36631. https://doi.org/10.3389/FIMMU.2012.00375/BIBTEX

Roncato, F., Rruga, F., Porcù, E., Casarin, E., Ronca, R., Maccarinelli, F., Realdon, N., Basso, G., Alon, R., Viola, G., & Morpurgo, M. (2018). Improvement and extension of anti-EGFR targeting in breast cancer therapy by integration with the Avidin-Nucleic-Acid-Nano-Assemblies. *Nature Communications 2018 9:1*, *9*(1), 1–11. https://doi.org/10.1038/s41467-018-06602-6

Rotella, D. P. (2002). Phosphodiesterase 5 inhibitors: current status and potential applications. *Nature Reviews. Drug Discovery*, *1*(9), 674–682. https://doi.org/10.1038/NRD893

Roti, J. L. (2008). Cellular responses to hyperthermia (40–46°C): Cell killing and molecular events. *International Journal of Hyperthermia*, *24*(1), 3–15. https://doi.org/10.1080/02656730701769841

Sani, A., Cao, C., & Cui, D. (2021). Toxicity of gold nanoparticles (AuNPs): A review. *Biochemistry and Biophysics Reports*, *26*, 100991. https://doi.org/10.1016/J.BBREP.2021.100991

Schipper, M. L., Iyer, G., Koh, A. L., Cheng, Z., Ebenstein, Y., Aharoni, A., Keren, S., Bentolila, L. A., Li, J., Rao, J., Chen, X., Banin, U., Wu, A. M., Sinclair, R.,

Weiss, S., & Gambhir, S. S. (2009). Particle Size, Surface Coating, and PEGylation Influence the Biodistribution of Quantum Dots in Living Mice. *Small*, *5*(1), 126–134. https://doi.org/10.1002/SMLL.200800003

Scialabba, C., Sciortino, A., Messina, F., Buscarino, G., Cannas, M., Roscigno, G., Condorelli, G., Cavallaro, G., Giammona, G., & Mauro, N. (2019). Highly Homogeneous Biotinylated Carbon Nanodots: Red-Emitting Nanoheaters as Theranostic Agents toward Precision Cancer Medicine. *ACS Applied Materials and Interfaces*, *11*(22), 19854–19866. https://doi.org/10.1021/acsami.9b04925

Sciortino, A., Cannizzo, A., & Messina, F. (2018). *Carbon Nanodots: A Review-From the Current Understanding of the Fundamental Photophysics to the Full Control of the Optical Response*. https://doi.org/10.3390/c4040067

Sciortino, A., Mauro, N., Buscarino, G., Sciortino, L., Popescu, R., Schneider, R., Giammona, G., Gerthsen, D., Cannas, M., & Messina, F. (2018). β-C3N4 Nanocrystals: Carbon Dots with Extraordinary Morphological, Structural, and Optical Homogeneity. *Chemistry of Materials*, *30*(5), 1695–1700. https://doi.org/10.1021/ACS.CHEMMATER.7B05178

Shabestari Khiabani, S., Farshbaf, M., Akbarzadeh, A., & Davaran, S. (2017). Magnetic nanoparticles: preparation methods, applications in cancer diagnosis and cancer therapy. *Artificial Cells, Nanomedicine, and Biotechnology*, *45*(1), 6–17. https://doi.org/10.3109/21691401.2016.1167704

Sharma, A., Jampani, V. S. R., & Lagerwall, J. P. F. (2019). Realignment of Liquid Crystal Shells Driven by Temperature-Dependent Surfactant Solubility.

Langmuir, *35*(34), 11132–11140. https://doi.org/10.1021/ACS.LANGMUIR.9B00989/SUPPL_FILE/LA9B00989_SI_001.PDF

Soliman, H. H., Jackson, E., Neuger, T., Claire Dees, E., Donald Harvey, R., Han, H., Ismail-Khan, R., Minton, S., Vahanian, N. N., Link, C., Sullivan, D. M., & Antonia, S. (2014). A first in man phase I trial of the oral immunomodulator, indoximod, combined with docetaxel in patients with metastatic solid tumors. *Oncotarget*, *5*(18), 8136. https://doi.org/10.18632/ONCOTARGET.2357

Soliman, H. H., Minton, S. E., Han, H. S., Ismail-Khan, R., Neuger, A., Khambati, F., Noyes, D., Lush, R., Chiappori, A. A., Roberts, J. D., Link, C., Vahanian, N. N., Mautino, M., Streicher, H., Sullivan, D. M., Antonia, S. J., Soliman, H. H., Minton, S. E., Han, H. S., … Antonia, S. J. (2016). A phase I study of indoximod in patients with advanced malignancies. *Oncotarget*, *7*(16), 22928–22938. https://doi.org/10.18632/ONCOTARGET.8216

Suk, J. S., Xu, Q., Kim, N., Hanes, J., & Ensign, L. M. (2015). PEGylation as a strategy for improving nanoparticle-based drug and gene delivery. *Advanced Drug Delivery Reviews*, *99*(Pt A), 28. https://doi.org/10.1016/J.ADDR.2015.09.012

Suk, J. S., Xu, Q., Kim, N., Hanes, J., & Ensign, L. M. (2016). PEGylation as a strategy for improving nanoparticle-based drug and gene delivery. In *Advanced Drug Delivery Reviews* (Vol. 99, Issue Pt A, pp. 28–51). Elsevier B.V. https://doi.org/10.1016/j.addr.2015.09.012

Sun, R., Xiang, J., Zhou, Q., Piao, Y., Tang, J., Shao, S., Zhou, Z., Bae, Y. H., & Shen, Y. (2022). The tumor EPR effect for cancer drug delivery: Current status, limitations, and alternatives. *Advanced Drug Delivery Reviews*, *191*, 114614. https://doi.org/10.1016/J.ADDR.2022.114614

Sun, Y. P., Zhou, B., Lin, Y., Wang, W., Fernando, K. A. S., Pathak, P., Meziani, M. J., Harruff, B. A., Wang, X., Wang, H., Luo, P. G., Yang, H., Kose, M. E., Chen, B., Veca, L. M., & Xie, S. Y. (2006). Quantum-sized carbon dots for bright and colorful photoluminescence. *Journal of the American Chemical Society*, *128*(24), 7756–7757. https://doi.org/10.1021/ja062677d

Ten Tije, A. J., Verweij, J., Loos, W. J., & Sparreboom, A. (2012). Pharmacological Effects of Formulation Vehicles. *Clinical Pharmacokinetics 2003 42:7*, *42*(7), 665–685. https://doi.org/10.2165/00003088-200342070-00005

Torchilin, V. (2011). Tumor delivery of macromolecular drugs based on the EPR effect. *Advanced Drug Delivery Reviews*, *63*(3), 131–135. https://doi.org/10.1016/J.ADDR.2010.03.011

Tripodo, G., Wischke, C., Neffe, A. T., & Lendlein, A. (2013). Efficient synthesis of pure monotosylated beta-cyclodextrin and its dimers. *Carbohydrate Research*, *381*, 59–63. https://doi.org/10.1016/j.carres.2013.08.018

Varvarà, P., Tranchina, L., Cavallaro, G., & Licciardi, M. (2020). Preparation and characterization of gold nanorods coated with gellan gum and lipoic acid. *Applied Sciences (Switzerland)*, *10*(23), 1–18. https://doi.org/10.3390/app10238322

Wang, L., & Li, C. (2011). pH responsive fluorescence nanoprobe imaging of tumors by sensing the acidic microenvironment. *Journal of Materials Chemistry*, *21*(40), 15862–15871. https://doi.org/10.1039/C1JM12072G

Wang, X., Zhao, S., Xin, Q., Zhang, Y., Wang, K., & Li, M. (2024). Recent progress of CDK4/6 inhibitors' current practice in breast cancer. *Cancer Gene Therapy 2024*, 1–9. https://doi.org/10.1038/s41417-024-00747-x

Watt, J., Hance, B. G., Anderson, R. S., & Huber, D. L. (2015). Effect of Seed Age on Gold Nanorod Formation: A Microfluidic, Real-Time Investigation. *Chemistry of Materials*, *27*(18), 6442–6449. https://doi.org/10.1021/ACS.CHEMMATER.5B02675/ASSET/IMAGES/LARGE/CM-2015-02675A_0006.JPEG

Weissleder, R. (2001). A clearer vision for in vivo imaging: Progress continues in the development of smaller, more penetrable probes for biological imaging. *Nature Biotechnology*, *19*(4), 316–317. https://doi.org/10.1038/86684

Wicki, A., Witzigmann, D., Balasubramanian, V., & Huwyler, J. (2015). Nanomedicine in cancer therapy: Challenges, opportunities, and clinical applications. In *Journal of Controlled Release* (Vol. 200, pp. 138–157). Elsevier B.V. https://doi.org/10.1016/j.jconrel.2014.12.030

Wu, L., Mendoza-Garcia, A., Li, Q., & Sun, S. (2016). Organic Phase Syntheses of Magnetic Nanoparticles and Their Applications. *Chemical Reviews*, *116*(18), 10473–10512. https://doi.org/10.1021/ACS.CHEMREV.5B00687

Wu, R. S., Lin, Y. S., Nain, A., Unnikrishnan, B., Lin, Y. F., Yang, C. R., Chen, T. H., Huang, Y. F., Huang, C. C., & Chang, H. T. (2022). Evaluation of chemotherapeutic response in living cells using subcellular Organelle–Selective amphipathic carbon dots. *Biosensors and Bioelectronics*, *211*, 114362. https://doi.org/10.1016/J.BIOS.2022.114362

Xie, J., Lee, S., & Chen, X. (2010). Nanoparticle-based theranostic agents. In *Advanced Drug Delivery Reviews* (Vol. 62, Issue 11, pp. 1064–1079). Elsevier. https://doi.org/10.1016/j.addr.2010.07.009

Xue, Y., Li, X., Li, H., & Zhang, W. (2014). Quantifying thiol–gold interactions towards the efficient strength control. *Nature Communications 2014 5:1*, *5*(1), 1–9. https://doi.org/10.1038/ncomms5348

Yan, F., Sun, Z., Zhang, H., Sun, X., Jiang, Y., & Bai, Z. (2019). The fluorescence mechanism of carbon dots, and methods for tuning their emission color: a review. In *Microchimica Acta* (Vol. 186, Issue 8). Springer-Verlag Wien. https://doi.org/10.1007/s00604-019-3688-y

Yang, T., Huang, J. L., Wang, Y. T., Zheng, A. Q., Shu, Y., & Wang, J. H. (2019). β-Cyclodextrin-Decorated Carbon Dots Serve as Nanocarriers for Targeted Drug Delivery and Controlled Release. *ChemNanoMat*, *5*(4), 479–487. https://doi.org/10.1002/CNMA.201800528

Yap, T. A., Parkes, E. E., Peng, W., Moyers, J. T., Curran, M. A., & Tawbi, H. A. (2021). Development of Immunotherapy Combination Strategies in Cancer. *Cancer Discovery*, *11*(6), 1368. https://doi.org/10.1158/2159-8290.CD-20-1209

Yoo, J., Park, C., Yi, G., Lee, D., & Koo, H. (2019). Active Targeting Strategies Using Biological Ligands for Nanoparticle Drug Delivery Systems. *Cancers*, *11*(5), 640. https://doi.org/10.3390/cancers11050640

Yu, S., Zheng, J., Zhang, Y., Meng, D., Wang, Y., Xu, X., Liang, N., Shabiti, S., Zhang, X., Wang, Z., Yang, Z., Mi, P., Zheng, X., Li, W., & Chen, H. (2023). The mechanisms of multidrug resistance of breast cancer and research progress on related reversal agents. *Bioorganic & Medicinal Chemistry*, *95*, 117486. https://doi.org/10.1016/J.BMC.2023.117486

Zakharia, Y., McWilliams, R. R., Rixe, O., Drabick, J., Shaheen, M. F., Grossmann, K. F., Kolhe, R., Pacholczyk, R., Sadek, R., Tennant, L. L., Smith, C. M., Kennedy, E. P., Link, C. J., Vahanian, N. N., Yu, J., Shen, S. S., Brincks, E. L., Rossi, G. R., Munn, D., & Milhem, M. (2021). Phase II trial of the IDO pathway inhibitor indoximod plus pembrolizumab for the treatment of patients with advanced melanoma. *Journal for ImmunoTherapy of Cancer*, *9*(6). https://doi.org/10.1136/jitc-2020-002057

Zang, X., Song, J., Yi, X., & Piyu, J. (2022). Polymeric indoximod based prodrug nanoparticles with doxorubicin entrapment for inducing immunogenic cell death and improving the immunotherapy of breast cancer. *Journal of Materials Chemistry B*, *10*(12), 2019–2027. https://doi.org/10.1039/D2TB00197G

Zhang, T., Qu, J., Yao, Y., Zhang, Y., Ma, Y., Wu, D., Cao, Y., Yang, M., Zhang, Y., Tang, M., & Pu, Y. (2020). N-doped carbon dots triggered the induction of ROS-

mediated cytoprotective autophagy in Hepa1-6 cells. *Chemosphere*, *251*, 126440. https://doi.org/10.1016/J.CHEMOSPHERE.2020.126440

Zhang, Y., Newton, B., Lewis, E., Fu, P. P., Kafoury, R., Ray, P. C., & Yu, H. (2015). Cytotoxicity of Organic Surface Coating Agents Used for Nanoparticles Synthesis and Stability. *Toxicology in Vitro : An International Journal Published in Association with BIBRA*, *29*(4), 762. https://doi.org/10.1016/J.TIV.2015.01.017

Zou, L., Wang, H., He, B., Zeng, L., Tan, T., Cao, H., He, X., Zhang, Z., Guo, S., & Li, Y. (2016). Current Approaches of Photothermal Therapy in Treating Cancer Metastasis with Nanotherapeutics. *Theranostics*, *6*(6), 762. https://doi.org/10.7150/THNO.14988

Zou, W. (2005). Immunosuppressive networks in the tumour environment and their therapeutic relevance. *Nature Reviews Cancer 2005 5:4*, *5*(4), 263–274. https://doi.org/10.1038/nrc1586

Acknowledgments

First of all, I would like to acknowledge the Laboratory of Biocompatible Polymers at the University of Palermo where this thesis work was carried out under the supervision of Prof. Gennara Cavallaro and Prof. Nicolò Mauro, whom I sincerely thank for guiding me through this PhD journey.

A special thanks go to Prof. Helena F. Florindo and Dott. Rita C. Acúrcio from the Faculdade de Farmacia (University of Lisbon), for hosting me during the six months abroad of my PhD program and performing the *in vivo* evaluations of CDs-IND antitumoral activity.

I acknowledge Dott. Sergio Scirè (University of Palermo) for performing the evaluation of CT contrast of AuCDs-Glu, and Paolo Bonomo, Advanced Technologies Network Center—ATeN Center, for the Mico-CT analysis reported in this work.

I also thank Prof. Cesare Gagliardo and Prof. Maurizio Marrale (University of Palermo) for collaborating on the characterization of GdCDs by performing MRI contrast analysis.